Università di Pisa

DIPARTIMENTO DI FISICA "ENRICO FERMI"
Corso di Laurea in Fisica

Tesi di laurea

Commissioning and first data analysis of the Mainz radius experiment.

Candidato:
Adriano Del Vincio
Matricola 562946

Relatore:
Prof. Francesco Forti
Prof.ssa Concettina Sfienti

Anno Accademico 2022-23

Contents

Commissioning and first data analysis of the Mainz Radius Experiment.

Adriano del Vincio

Abstract

The Mainz Radius Experiment (MREX) is an experimental campaign with the aim of determining fundamental properties of the equation of state (EOS) of nuclear matter. The equation of state contains all the thermodynamic quantities of a system of nucleons, as energy, pressure, temperature, density, and asymmetry between the number of neutrons protons in nuclear-matter. An important parameter, poorly-known at the state of current knowledge, is the slope of the symmetry energy at saturation density L, which quantifies the dependencies of the energy per nucleon associated with the changes in neutron-proton asymmetry. It is also an essential element for the determination of the radius of neutron stars, whose description is still determined by the EOS, despite being many order of magnitude higher than the physical dimensions of the nuclei. The slope of the symmetry energy L is strongly correlated to a characteristic shown by heavy nuclei, the neutron-skin thickness, that is the difference between the spacial distribution radius R of the neutrons and protons. Nowadays it is well-known, thanks to various nuclear physics experiments, that the neutrons of a nucleus tend to accumulate at a larger radius, forming a neutral thin layer around atomic nuclei. This peculiar characteristic is known in literature as neutron-skin thickness. The experimental measurement of this quantity is the main method to estimate the value of L, which is used as an input to many theoretical models of neutron stars. The MREX is focused on the determination of the neutron skin thickness of ^{208}Pb from parity-violating experiments (PV) performed at the future MESA electron accelerator, that is currently under construction and will be located in Mainz. The parity-violating experiments, where longitudinal polarized electrons scatter from a fixed target at a single value of momentum transfer, consist in the determination of the cross section asymmetry $A_{pv} = \frac{\sigma^+ - \sigma^-}{\sigma^+ + \sigma^-}$ related to the different longitudinal polarization state of the beam. The parity-violating electron scattering is a valid probe to determine the neutron-skin thickness, because it is highly sensitive to the neutron distribution due to the larger coupling of the Z^0 boson to the weak charge Q_W of neutrons, which is approximately -0.99 per neutron, while that of the proton is 0.07. In this context, it is necessary to determine one of the possible background sources for the PV experiments, known as beam normal single spin asymmetry A_n, or transverse asymmetry. The asymmetry A_n, that concerns transversely polarized electrons, comes from the interference between two Feynman diagrams where one or two virtual photons are exchanged, giving a contribution of the order of $20\,ppm$. Because the values of A_n are typical higher that A_{pv}, the presence of a small transverse electron polarization component could produce an effect that is of the same order of magnitude of the A_{pv}. The work of this thesis focuses on the measurement of the transverse asymmetry A_n carried out at the Mainz microtron accelerator (MAMI) on a ^{12}C target. The ^{12}C target is particularly suited for studying and testing the electronics systems and detectors that will be employed in the next phase of the MREX experiment, the determination of A_n for ^{208}Pb. The measurement consists in the determination of A_n using two Cherenkov detectors made of fused-silica materials coupled to 3 and 8 photo-multiplier tubes. The two detectors have been tested in the laboratory, together with the new electronics for the data read-out, that consist in the NINO-asic board with which the impulse signals coming from the detectors are acquired. The beam parameters, as the transverse position of the beam, the scattering angles, and the current intensity and energy are determined with particular accuracy because their variation over time can result in effects that overlap with A_n. This required the development of a new analysis program, processing the raw data to extract the beam parameters relevant for the analysis, and separating the contributions of the false asymmetries from A_n. The work consisted in a first part dedicated to the calibration of the monitors, to measure the parameters of the beam. The second part was focused on the analysis of the data collected during the beam time, removing the outliers, identifying possible errors and isolating the contribution of false asymmetries. A_n has been measured for electron-carbon scattering at a two fixed angles ($\theta_B = -22.5°$, $\theta_A = 22.5°$) corresponding to a transfer momentum of $Q^2 = 0.04\,\mathrm{GeV}^2$. The measured values are: $A_B = -21 \pm 5\,(stat)\,ppm$ for

detector B and $23.1 \pm 1.7\,(stat)\,ppm$ for detector A. The different sign of the two measurements is in agreement with the opposite kinematic, and the two measurements are compatible within 1 σ, and in agreement with the previous measurements performed at MAMI. The results obtained confirm the capabilities of the electronic systems and components used during the experiments and are encouraging in anticipation of the next measurement of the transverse asymmetry for lead.

Organization of Contents

This thesis can be dived in two part: the first part is dedicated to the description and motivations regarding the MREX experiment and the description of the MAMI accelerator, where a large part of the work was done. The second part is focused on the analysis of the data acquired during the beam time. A list of the chapters with a brief explanation of the contents follows:

- **chapter 1**: Motivation of the MREX experiment for the measurement of the neutron skin thickness of ^{208}Pb. The Equation of state for nuclear matter is presented, with particular attention on the slope of the symmetry energy at saturation density L. Following, the parity violating scattering on ^{208}Pb is discussed, the is the main experimental method to extract the value of L. This term connects the equation of state for nuclear matter with the structure of the neutron star, and it directly associated with neutron star radii. Its determination is relevant to discriminate among the different existing theoretical models for the EOS, besides being important for astrophysical models of the internal structure of neutron star. In the end of the chapter, we briefly presenter the Beam normal single spin asymmetry (BNSSA), named also transverse asymmetry, the topic of this thesis. The BNSSA represents the principal background process for the parity violating experiment, and its determination is important to isolate possible systematic effect.
- **chapter 2**: This chapter focuses on the physical description of the transverse asymmetry. The theoretical model to obtain the value of the transverse asymmetry is presented, together with a final formula that encloses the dependence of the BNSSA on the transfer momentum Q, Compton and charge form factor. Following a review of the past measurement of the BNSSA.
- **chapter 3** This chapter is focused on a general description of MAMI electron accelerator, and its peculiar method, based on a cascade of microtrons, for accelerating particles. A section is dedicated to beam monitors, devices that measure the beam parameters using resonant cavities that are excited by the passage of the particles. The beam parameters are necessary to estimate and remove the contribution of beam fluctuations to the total asymmetry A_{tot} measured. In the end we briefly present the setup for the measure of the transverse asymmetry, and we describe the two Cherenkov detectors that are used.
- **chapter 4**: here we present some simple detector tests performed in the laboratory, and then we focus on the calibration phase, that comes before the acquisition of the data for the asymmetry. The calibration consists in the measurements the parameters for the conversion of the raw data of the beam monitors to data with the correct physical unit. After the calibration of the monitors, we explain the auto-calibration procedure, needed to measure and subtract the PMT offset from the measurements.
- **chapter 5**: Chapter 5 is focused on the data analysis. The rates with Lead target are measured, and we calculate the time needed to measure the transverse asymmetry with lead with a precision of $\simeq 2\,ppm$ for different value of the beam intensity. Hereafter we discuss the data selection and the linear fit for the data with carbon target.
- **chapter 6**: The result of the analysis are reported. The transverse asymmetry is measured by each PMT individually. Then the result are averaged to obtain a single measurement for each detector.

Chapter 1

Neutron Skin Thickness Measurement

1.1 The Mainz Radius Experiment

The Mainz Radius Experiment (MREX), at the Mainz nuclear physics institute, is an experimental campaign with the aim of investigating the nature of atomic nuclei, by measuring the neutron skin thickness of ^{208}Pb. The characteristics of atomic nuclei are mainly determined by the strong interaction, whose existence was firstly speculated by Yukawa in 1935. The strong interaction is responsible of a broad range of phenomena: from nature of the nuclei, the compositions of baryons and meson to the exotic structure of Neutron stars. Hence, nuclear physics provides many answers to fundamental questions that are important also in other fields of physics. In particular the neutron stars, that are among the most studied astrophysical objects, are ideal to study theories of dense nuclear matter. It can be surprising to think that, despite a difference of so many order of magnitude, neutron rich nuclei and neutron stars have the same basic physics description, represented by the the Equation Of State (EOS) of nuclear matter [1]. The Equation Of State represents the fundamental relation between the state variables such as temperature, energy, pressure and the neutron-proton asymmetry. Specifically, the final goal of the MREX experiment is to determine an important parameter of the EOS, the slope of the symmetry energy at saturation density L, which controls the change in energy due to presence of an asymmetry between neutron and proton densities. This parameters plays an important role for the determination of the radius of the neutron stars and it is also responsible for a peculiar characteristic shown by heavy nuclei: the neutron skin thickness. The neutron skin thickness δr_{np} is a phenomena that affect heavy nuclei, which consists in the accumulation of the excess of neutrons near the surface, producing a neutral layer of neutrons. It is defined in equation as:

$$\delta r_{np} = \sqrt{< r_n^2 >} - \sqrt{< r_p^2 >}, \tag{1.1}$$

Where $< r^2 >_n$ and $< r^2 >_p$ are the rms radii of proton and neutron distributions. The neutron skin thickness is sensitive to L, so an accurate determination of δr_{np} provides significant constrains on the value of L, which can be used as an input to many theoretical models of the structure of the neutrons stars. The determination of δr_{np} presents considerable difficulties. While r_p is measured with high accuracy, with the electrons elastic scattering experiments which involving electromagnetic force, the determination of r_n has traditionally relied on hadronic experiments, such as proton-nucleus scattering, π^0 photo-production, α and π nucleus scattering. These processes suffer from large and often uncontrolled theoretical uncertainties that compromise the extraction of the neutron density. The most promising method, that is the least model dependent, is parity-violating electron scattering, where longitudinal polarized electrons are elastically scattered off an unpolarized target. This method consists in the measurement of the cross-section asymmetry between right and left handed electrons:

$$A_{pv} = \frac{\sigma_R - \sigma_L}{\sigma_R + \sigma_L} \tag{1.2}$$

This process is dominated by the exchange of a virtual photon, which is sensitive to the charge form factor, and of a Z_0 boson, that is sensitive to the weak form factor. Since the weak charge of the neutron is $Q_w = 0.99$ and the weak charge of the proton is 0.04, the weak form factor contains the information on the neutron density, necessary to measure δr_{np}. In this context, the MREX experiment is an experimental campaign with the aim of measuring the neutron skin thickness via the parity violating scattering with the new MESA electron accelerator, at the Nuclear physics institute of Mainz.

1.2 Nuclear Equation of State (EOS) and Neutron Skin Thickness

During the 30s of the last century, a considerable part of the scientific community was focused in the study of the structure of atomic nuclei. The discovery that every atoms has a positive charged nucleus dates back to 1908, with the famous Rutherford experiment, where alpha particles scatter on a thin gold foil. In the following years, especially after the birth of quantum mechanics in the second half of the 1920s, important progress was made in the knowledge of atomic nuclei and their properties. In 1935, a significant contribution was given by Carl Friedrich von Weizsäcker and Hans Bethe, who proposed the semi-empirical mass formula, to approximate the mass of an atomic nucleus [2]. Although some refinements have been made over the years, the general structure of the formula is the same today. The model proposed by Weizsäcker is the application of the liquid-drop model for nuclear matter, where the nucleus is described as a drop of protons and neutrons, assumed to be incompressible and held together by a nuclear potential. The semi-empirical mass formula states that the mass of a nucleus with Z protons and N neutrons is given by:

$$m = Zm_p + Nm_n - \frac{E_B(N,Z)}{c^2} \tag{1.3}$$

where E_B is the binding energy, containing 5 parameters:

$$E_B = a_V A - a_s A^{\frac{2}{3}} - a_c \frac{Z^2}{A^{\frac{1}{3}}} - a_{asym} \frac{(N-Z)^2}{A} + \delta(N,Z) \tag{1.4}$$

The first two terms a_V, a_s are the volume energy and the surface energy, and conceptually analogous to the volume and surface parameter of the liquid drop model. The volume term represent the energy due to the interaction of each nucleon with the other nearby nucleons. This term is proportional to $A = N + Z$, that is the number of nucleons, which is proportional to the volume. The second term represents the surface energy, and it is a correction to the volume energy. For the volume energy parameter, it is assumed that each nucleon interacts with a constant number of nearby nucleons. This is not true, because the strong nuclear force is a short distance interaction, and furthermore the external protons and neutrons have less neighbors to interact with. This correction terms is proportional to $A^{\frac{2}{3}}$, also proportional to the surface area. The third term, with coefficient a_c denote the binding energy correction due to the Coulomb repulsion between protons. The fourth term, the asymmetry term, is proportional to the asymmetry between neutrons and protons. The theoretical justification for this terms is due to the Pauli exclusion principle. Neutrons and protons are distinct type of particles, and occupy different quantum states. Because neutrons/protons are fermions, they can not occupy a state with the same quantum numbers, therefore higher energy states are progressively filled. If there is an asymmetry between neutrons and protons, for example the number of neutrons is greater than the number of protons, some neutrons will be in higher energy states with respect to the protons. The imbalance between the nucleons causes the energy to be higher with respect to the situation with the equal number of p and n. The last term is the pairing term, and describes the effect of spin coupling, which leads to the formation of protons or neutrons pairs. It has a positive or negative values depending on the parity of N,Z. We stress the fact that the liquid-drop model has the underlying assumption that the nucleons are incompressible. For this reason it is well defined the concept of saturation density ρ_0, the maximum density beyond which nucleons can not be compressed further. In the end the liquid drop models assume that the density ρ is almost equal to ρ_0 and independent of mass number A. In the context of neutron stars, it is more useful to consider the binding energy per nucleons $\epsilon = \frac{-E_B}{A}$ in the thermodynamic limit in which the number of nucleons (and so the volume) is taken to infinity:

$$\epsilon(\rho_0, \alpha) = -\frac{E_B}{A} = -a_V + a_{asym}\big(\frac{\rho_n - \rho_p}{\rho_n + \rho_p}\big)^2, \tag{1.5}$$

Where we have introduced the proton and neutron densities ρ_n and ρ_p, and the saturation density ρ_0. We notice that the surface term and the pairing terms vanish for $A \xrightarrow{\infty}$, and we are neglecting the Coulomb term a_c [1]. In reality, this simple equation is only an approximation, because the nuclear matter doesn't behave like an ideal liquid drop, and it is not incompressible. To describe the response of the nuclear matter to density variation, as well as temperature, etc. we need the equation of state (EOS) of the system, the fundamental relation that binds all these quantities together. In the ideal limit of $T = 0$, the EOS for neutron stars depends on ρ, the conserved baryon density, and neutron-proton asymmetry α. Starting from equation 1.5, the energy density is expanded in a power series of $\alpha = \dfrac{\rho_n - \rho_p}{\rho_n + \rho_p}$:

$$\epsilon(\rho, \alpha) = \epsilon_{snm} + \alpha^2 S(\rho) + O(\alpha^4), \tag{1.6}$$

Where the energy is split in two terms, with $\epsilon_{snm} = \epsilon(\rho, \alpha = 0)$ that represents the energy density for symmetry nuclear matter, with equal amount of neutrons and protons. Since the the strong force does not depend on the isospin, no odd power of α appears in the expansion; or in other words, neglecting electromagnetic interaction and weak interaction, the equation of state depends only on the relative asymmetry between neutrons and protons and it does not matter if such an asymmetry is biased towards protons or neutrons. The term $S(\rho)$ is the symmetry energy, and represents the cost of converting symmetric nuclear matter ($\alpha = 0$) to pure neutrons matter, as the case of neutron star. Now we can proceed considering the saturation density. A further expansion around ρ is done, following [3]:

$$\begin{aligned} S(\rho) &= J + L \cdot \frac{\rho - \rho_0}{3\rho_0} + \frac{1}{2} K_{sym} \cdot \left(\frac{\rho - \rho_0}{3\rho_0}\right)^2 \\ \epsilon_{smn}(\rho) &= \epsilon_0 + \frac{1}{2} K_0 \left(\frac{\rho - \rho_0}{3\rho_0}\right)^2 \end{aligned} \tag{1.7}$$

Several new terms appear in this expression:

- ϵ_0 is the energy per nucleon for symmetric matter at saturation density.
- J is the symmetry energy at saturation density.
- L is the slope of the symmetry energy.
- K_0 is the incompressibility coefficient for symmetric matter.
- K_{sym} is the incompressibility coefficient for the symmetry energy.

In equation 1.7 appears a new quantity: L, the slope of the symmetry energy. This is a key component of the EOS, whose value is an important parameter to determine the radius of neutron star. L quantifies the difference between the symmetry energy at saturation (as in the nuclear core) and the symmetry energy at lower densities, as in the nuclear surface. L is also related to the pressure P at saturation density, as seen in equation 1.10. Giving the EOS in term of ρ and α, the pressure can be written as:

$$P = \rho^2 \frac{\partial \epsilon(\rho, \alpha)}{\partial \rho} \tag{1.8}$$

Equation 1.8 can be simply derived from the first principle of thermodynamics. Now it is possible to substitute everything in ϵ, making all the dependencies explicit:

$$\epsilon(\rho, \alpha) = (\epsilon_0 + \alpha^2 J) + \alpha^2 L x + \frac{1}{2}(K_0 + \alpha^2 K_{sym}) x^2, \tag{1.9}$$

[1] This term is relevant in presence of a $\rho_p \neq 0$, but neutron star can be assumed globally with almost zero electric charge, so this will not give a contribution.

where $x = \dfrac{\rho - \rho_0}{3\rho_0}$. Considering pure neutron matter, with $\alpha = 1$, the pressure at saturation density P_0 can be easily computed with the formula (1.8). The result is:

$$P_0 \simeq \frac{1}{3}\rho_0 L \tag{1.10}$$

From this expression we learn that the slope of the symmetry energy is essential to determine the pressure for densities near saturation. Such conditions are encountered in nuclei and in the core of neutron stars. The contribution of the symmetric term $\epsilon_{snm}(\rho)$ vanishes, and at first order the pressure depends only on L. Because of this, it becomes more clear the link between L and the neutron skin thickness. Let's consider the case of the ^{208}Pb, with an excess of 44 neutrons. Placing the excess of neutrons in the surface of the nucleus is discouraged by the surface term a_S, which tends to minimize the area. However, if the excess of neutrons is placed in the core of the nucleus, it increases the symmetry energy $S(\rho)$. In the end the neutron skin is the result of the competitions between the surface tension and the slope of the symmetry energy. Measurements of the neutron skin have been performed by the PREX collaboration at Thomas Jefferson National Accelerator Facility in Virginia [4]. However the precision attained was insufficient to distinguish between the various competing models which describe the relation between δr_{np} and L. In fact, theoretical models, while predicting different values of L, show that there is a strong correlation between these two quantities, as show in figure (1.1).

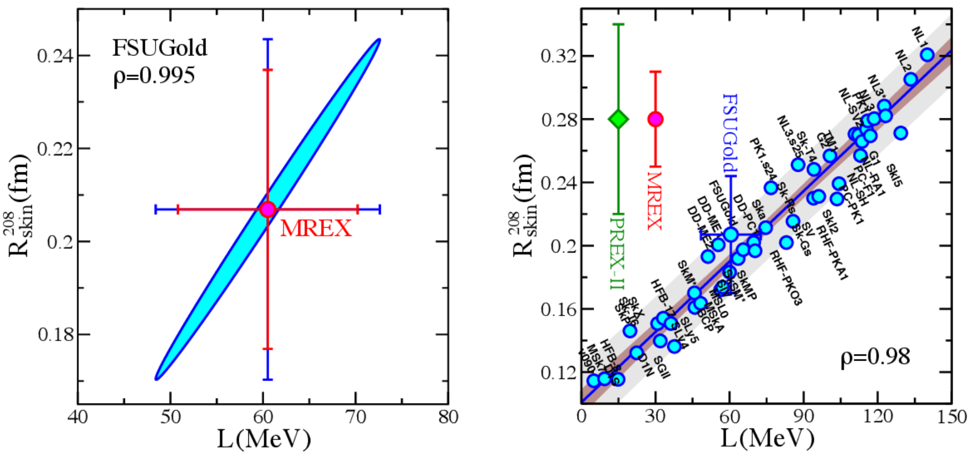

Figure 1.1: *On the right* Neutron skin thickness of ^{208}Pb as a function of the slope of the symmetry energy L. Each dot represent the a value of L and δr_{np} as predicted by various theoretical models. The error bars represent ± 0.06 fm and ± 0.03 fm for the future experiments of PREX-II and MREX. Notice the different scale for x and y axis, a small uncertainty for the neutron skin measurement correspond to an higher uncertainty for the values of L. *On the left* Covariance ellipse displaying the correlation between L and the neutron skin thickness, for FSUGold model. The covariance ρ is equal to 0.995.

A strong linear correlation is evident, then measuring the neutron skin gives access to L.

1.3 Parity-violating Scattering Experiment

In the last years, the parity violating electron scattering seems to be a promising method for the determination of the neutron-skin thickness of ^{208}Pb. The choice of lead is due to the significant neutron excess and stability of lead nuclei (^{208}Pb is a double magic nucleus). The advantage of this method is that it is free from the many uncertainties associated to strong interaction. The main disadvantage is the need to accumulate large statistics, because the reaction are mediated by the weak interaction, associated with smaller scattering amplitude compared to electromagnetic and strong interactions. The parity violating scattering is highly sensitive to the neutron density because, as mentioned above, since the weak charge of the neutron is higher compared to the weak charge of the proton. In this reaction, longitudinally polarized electrons are elastically scattered off a lead target. The important quantity to determine is the parity violating asymmetry A_{pv}, the difference in cross section between the scattering of right and left handed electrons.

$$A_{pv} = \frac{\sigma_R - \sigma_L}{\sigma_R + \sigma_L}, \tag{1.11}$$

The theoretical calculation of A_{pv} includes the interference between the exchange of virtual γ and Z^0. In the Born approximation A_{pv} is directly proportional to the weak form factor, and is given by:

$$A_{PV} \simeq \frac{G_F Q^2}{4\pi\alpha} \cdot \frac{Q_W F_W(Q^2)}{Z F_{ch}(Q^2)}, \tag{1.12}$$

where G_F is the Fermi constant, Q^2 is the transferred momentum, Z and Q_W are the electric and weak charge of the nucleus, F_{ch} and F_W are the charged and weak form factors of the nucleus. The charge form factor of the lead nucleus is known with high accuracy (precision of 0.02 %), so in this limit the only quantity that is unknown is $F_W(Q^2)$. In the long wavelength approximation, the weak form factor at single value of momentum transfer is given by:

$$F_W(Q^2) = \frac{1}{Q_W} \int \rho_W(r) \frac{sin(Qr)}{Qr} d^3r = (1 - \frac{Q^2}{6} R_W^2 + \frac{Q^4}{120} R_W^4 + ...) \tag{1.13}$$

The form factor is normalized in such a way that $F_W(Q^2 = 0) = 1$. The weak charge radius correspond to $R_W^2 = -6 \frac{\partial F_W}{\partial Q^2}\Big|_{Q^2=0}$. Now it is clear that parity-violating experiment are a promising method to extract information about neutron density. The difficulty is represented by the small values of A_{pv} asymmetry. Typical values are on the order of $1\,ppm$ or less, for lead target. This requires high statistic to reduce the uncertainty of the measurement and high control over the systematic effects. In 2012 the PREX collaboration measured for the first time the neutron skin through parity-violating experiment, obtaining:

$$\delta r_{np} = 0.33^{+0.16}_{-0.18}\mathrm{fm} \tag{1.14}$$

The error associated to this first measurement is not enough small to provide significant constraints on the values of L. The MREX experiment has the objective of measuring the neutron skin of lead with a precision of 0.5% ($\pm 0.03\,\mathrm{fm}$). This high precision is needed to decrease the uncertainty associated to L. For example, the left plot in 1.1, shows the correlation between the neutron skin thickness of ^{208}Pb and the slope of the symmetry energy as predicted by FSUGold model ([5]). With a precision of $\pm 0.03\,\mathrm{fm}$, L is determined with $\pm 12.1\,\mathrm{MeV}$. In 2019, a new measurement of the PREX collaboration [6], obtain of $\delta r_{np} = 0.283 \pm 0.071\mathrm{fm}$. With the new measurement that will be performed in MESA accelerator by MREX, the precision will be improved further by a factor 2.

1.3.1 Neutron Star Radius

We mentioned that the slope of the symmetry energy L is strongly correlated to the neutron skin thickness of ^{208}Pb and also to R_{ns}. We can go deeper in the discussion stating that the maximum neutron-star mass and radius are uniquely constrained by the E0S ([7]). The maximum mass depends on the energy density dependence of the pressure, that must be high enough to oppose the gravitational collapse into a black hole. Moreover, stellar radii are strongly dominated by the pressure of degenerate nuclear matter near the saturation density. The connection between the radius of compact object and pressure is enclosed in the Volkov-Oppenheimer equation; resolving the equation for a compact symmetric object gives the relation between radius and pressure P_c at the center of the star (formal proof in [8]).

$$R^2 = \frac{3}{8\pi\rho} \frac{1 - (\rho + P_c)^2}{(\rho + 3P_c)^2} \tag{1.15}$$

But the pressure P_c is, in large part, determined by the symmetry energy of the equation of state, so there should be a strong correlation between L and the neutron star radius R_{ns}. In the end, different theoretical models [9] confirm the connection between L and R_{ns}, for example we show the covariance ellipses predicted by FSUGold model between the slope of the symmetry energy L and the stellar radii in figure 1.2

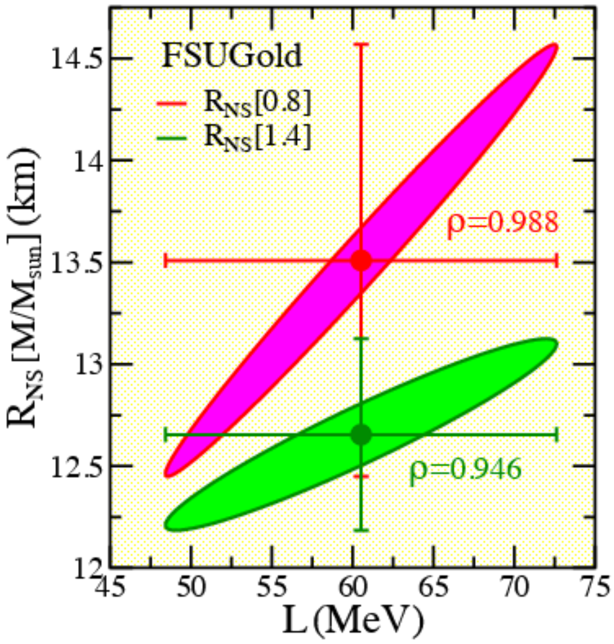

Figure 1.2: Covariance ellipses between slope of the symmetry energy and stellar radii, for 0.8 and 1.4 solar masses, predicted by the relativistic density model FSUGold.

From these consideration, astronomical observations of mass and radii of neutron stars represents important constrains on the EOS, and are valuable for understanding the behaviour and physics of the atomic nuclei. Astronomical observations of the neutron star radius rely traditionally on photometric measurements, assuming that thermal emission of light from the surface follow a blackbody spectrum at uniform temperature. These measurement are affected by systematic uncertainties that are typically of a couple of kilometers. However, the situation is rapidly changing with the beginning of the gravitational wave detection. The first observation of the binary neutron star merger by the LIGO-Virgo collaboration opened a new path to measure the neutron-stars radius [10]. In fact, the gravitational wave generated by the merging of two neutron stars depends on a property called tidal deformability; this parameters describes the tendency of a neutron star to deform in response of the gravitational field of its companion star, developing a mass quadrupole moment. This parameters Λ, is highly sensitive to the ratio of the stellar radius to the Schwarzschild radius:

$$\Lambda = \frac{2}{3} k_2 \left(\frac{c^2 R_{NS}}{GM}\right)^5 \tag{1.16}$$

In this expression, M and R_{NS} are the neutron star mass and radius, and k_2 is the second tidal Love number [11], which is computed from the quadrupole component of the gravitational field induced by the companion. From the first detection, an upper limit of $R_{NS}^{1.4} < 13.76\,\mathrm{km}$ was placed on the radius of a neutron star with a 1.4 solar masses. Because of the strong correlation between R_{NS}, L and δr_{np}, this is a indirect constrain on the neutron skin thickness of ^{208}Pb. An upper limit of $\delta r_{np} < 0.25\,\mathrm{fm}$ was obtained. This limits is in slightly tension with the larger values measured by PREX collaboration, suggesting that the symmetry energy, for slightly higher density as in neutron stars, decreases with respect to the typical density found in atomic nuclei. This increment and decrement may be an indication of the presence of phase transition in the interior of neutron stars.

1.4 Transverse Asymmetry

The parity-violating scattering has numerous advantages for extracting the neutron-skin thickness of nuclei. However, the asymmetry to measure is rather small. To measure such asymmetries, it is necessary to reduce as much as possible the systematic effects, that can alter the result of the measurement. One of the main sources of background for the measurement of A_{PV} is a different process that concerns transverse polarized electrons. The different polarization of the electrons produce an asymmetry, called beam normal single spin asymmetry (BNSSA), or transverse asymmetry A_n. Since such asymmetries are typically one order of magnitude higher than the parity-violating ones, a small normal component of the beam polarization during parity-violating experiments can produce a systematic effect that changes the final result. The subject of this thesis is the measurement of transverse asymmetry A_n for carbon target, performed at MAMI, the Mainz microton accelerator. The choice of carbon target is due to the fact that the transverse asymmetry for ^{12}C is well known and already measured at MAMI; the expected asymmetry is roughly $20\,ppm$, thus it is particularly suited for the commissioning of the new experimental setup. Such asymmetries are challenging because they require calculation of box diagrams with intermediate excited states [12], which will be threated in chapter 2. After the determination on A_n for ^{12}C, the next phase of the MREX experiment will be the determination of the transverse asymmetry for ^{208}Pb. As already mentioned, this is mandatory to constrain the systematic effects in PV experiments. However, it is also interesting because in the last measurement performed by PREX [13] the transverse asymmetry for ^{208}Pb target is compatible with zero, with a complete disagreement with the theoretical predictions. Since the theoretical prediction for hydrogen, helium, carbon and zirconium are in agreement with theory, a second, independent measurement of the BNSSA for lead is interesting, to confirm the measurement performed by PREX.

Chapter 2

Transverse Asymmetry

This chapter is focused on describing the theory behind the transverse asymmetry . The transverse asymmetry arises from interference between two scattering amplitudes (the exchange of one and two virtual photons, respectively) and it is deeply connected with the Time-reversal operator. These two scattering amplitude, given by electromagnetic interaction between the incident electron and the nucleus, are explained in this chapter, together with the limits of theory. The chapter ends by presenting the problem of the anomalous observation made by PREX, of zero A_n for lead target. In the end we discuss the general formula of A_n and we study how the accuracy of a measurement vary increasing the statistics.

2.1 Description of the Process

The Beam Normal single spin asymmetry, which we will refer for brevity as Transverse asymmetry, originates from the interference of two scattering process. The theory of the electron scattering against a spin 0 target is extensively treated in [12]. To understand why the interference of this two scattering amplitude give rise to an asymmetry, we first have to look at the kinematic of the experiment:

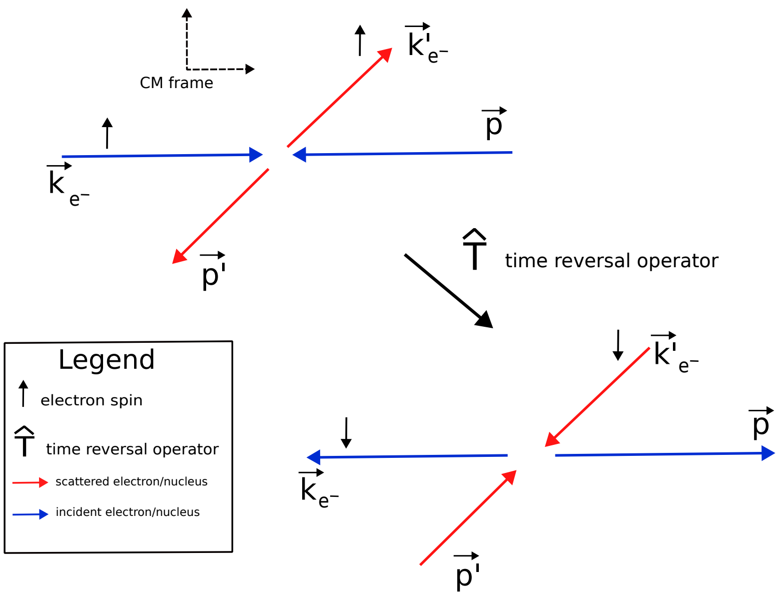

Figure 2.1: Scheme of the scattering process. In blue the incident electron and nucleus, in red the outgoing electron and nucleus. All the quantities are referred to the center of mass frame. The small arrow over the vector represent the electron spin, aligned in the normal plane.

Where all the momenta are measured respect to the center of mass frame. In the figure we can confront the two situation before and after applying the Time-reversal operator, $\hat{\Theta}$. Looking at the picture we can understand that :

- Before applying $\hat{\Theta}$, we have the incident electron with $\vec{k}$ momenta and the nucleus with $\vec{P}$ momenta, after applying $\hat{\Theta}$ we have that the incident/outgoing electron and the incident/outgoing nucleus are exchanged.
- The $\hat{\Theta}$ operator acts also on the spin of the electron. Because we are considering process where the spin doesn't flip, the two situations are not equivalent.
- Considering that the process is elastic, the kinematic is the same, taking $\vec{p}$ and $\vec{k}$ as the initial particle momenta, or $\vec{p}'$ and $\vec{k}'$.

The time-reversal operator seems to connect the two different cases of UP and DOWN polarized electron. Our effort is to measure the asymmetry between the two cross section:

$$A = \frac{\sigma_{\uparrow} - \sigma_{\downarrow}}{\sigma_{\uparrow} + \sigma_{\downarrow}} \tag{2.1}$$

And it's particularly clear that a non-zero asymmetry depends on how the time-reversal act on the elastic amplitude of the process.
With this idea, let's see in more detail the $\hat{\Theta}$. We know that $\hat{\Theta}$ is an anti-unitary operator that can be always seen as:

$$\hat{\Theta} = U \cdot K$$

Where U is an unitary operator, while K is the complex conjugation operator that generates the complex conjugate of each coefficient in front of it. If we consider a ket describing a system we have that:

$$Kc\,|\alpha\rangle = c^* K\,|\alpha\rangle \tag{2.2}$$

Now, let's consider H as the hamiltonian of our system. We want to apply the $\hat{\Theta}$ operator. We can now use the assumption that the hamiltonian consist of two term, which correspond to the two different scattering process. Because of the electromagnetic interaction conserve CP, so also T is conserved, we know in advance that each piece of the hamiltonian commute with $\hat{\Theta}$. Now let's see what happen for an hamiltonian which has an imaginary part:

$$H = H_R + iH_{Im} \quad ; \quad \hat{\Theta}H\hat{\Theta}^{-1} = \hat{\Theta}H_R\hat{\Theta}^{-1} + \hat{\Theta}iH_{Im}\hat{\Theta}^{-1} \Rightarrow H_R - iH_{Im} \neq H \tag{2.3}$$

what we understand from these simple calculation is that to give rise to an asymmetry, we expect an imaginary part of the scattering amplitude different from zero.
At the α leading order, the two process of the electron-Nucleus scattering that give rise to the asymmetry involve the exchange of one-photon-exchange (OPE) and two-photon-exchange (TPE). The Feynman diagrams that describes the processes are the following:

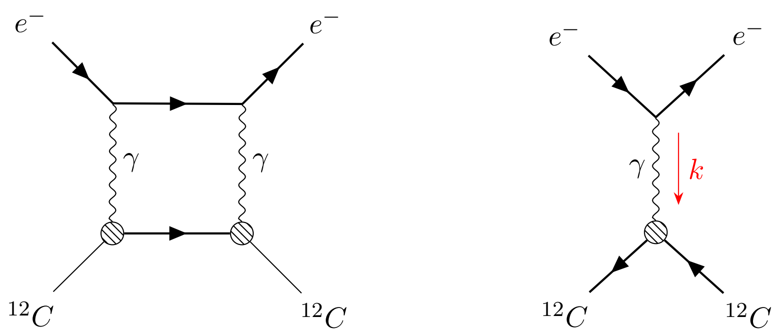

Figure 2.2: TPE and OPE diagrams in electron nucleus scattering.

The important quantity to compute the cross section is the scattering amplitude. The scattering amplitude is given by the two contributions: the exchange of a single virtual photon A_1 and the terms given by the two photon exchange A_2. In general we can write that the total scattering amplitude S:

$$S = \frac{e^2}{Q^2}\overline{u}(k')[\, m_e A_2 + A_1 \not{P}\,]\overline{u}(k) \tag{2.4}$$

Where in this expression $\vec{P} = \frac{\vec{p}+\vec{p}'}{2}$. The second term A_1 has a simple expression, given by the form factor of the nucleus:

$$A_1 = 2ZF_N(Q^2)$$

This expression is obtained if we look at the 2.2. For the one photon exchange the first vertex connects the incident and scattered electron, whose expression is given by $-ie\gamma^\mu$. The second vertex connect the carbon nucleus with the virtual photon. The carbon is threated like as a spin 0 particle, and the contribution due to the charge density in enshrined in the form factor. The lagrangian term for a vertex of this type is given by the formula:

$$\mathcal{L}_{interaction} = +ieA_\mu(\Phi\partial^\mu\Phi^\dagger - \Phi^\dagger\partial_\mu\Phi) \tag{2.5}$$

For the spin 0 field Φ. This is not the only piece of the lagrangian: there exist another term of interaction, that involves a vertex with four particles which is not of our interest. This interaction term give rise to the Feynmann rule for spin 0 particle, and we have to substitute for this vertex:

$$-ie(p + p')_\mu$$

And we recognize, apart from a factor 2, $\not{P}$ which multiplies A_1. The last term is the feynmann propagator for the photon, that give the $\frac{1}{Q^2}$ term. This first part of the scattering amplitude is T-even, and it is purely real, so it is the imaginary part of the two photon exchange which give rise to the asymmetry. The expression that connects the amplitude with the transverse asymmetry is given by:

$$A_n = -\frac{m_e}{\sqrt{s}} tan(\frac{\theta_{CM}}{2})\frac{\mathrm{Im}(A_2)}{ZF_N(Q^2)} \tag{2.6}$$

Looking at this formula, the theoretical effort to compute the transverse asymmetry is given by the imaginary part of A_2. The calculation of this quantity is theoretically challenging, due to the fact that at energies of $\simeq 1\,\mathrm{GeV}$ of incident electrons, contributions from intermediate excited states become important. Because of this, the contribution of A_2 are given by the sum of elastic intermediate state and inelastic terms, which involve hadronic excitations.

2.1.1 Hadronic Tensor

The imaginary part A_2 is related to the two-photon exchange. To compute this quantity, we have to perform an integration over the internal momenta of the electron k_1 (see figure 2.2). This contribution, following [12], is given by:

$$\mathrm{Im}(A_2) = e^4\frac{1}{(2\pi)^2}\int \frac{l_{\mu\nu}\cdot W^{\mu\nu}}{2E_1 Q_1^2 Q_2^2} d^3\vec{k_1} \tag{2.7}$$

Two new terms appear in this expression. The first term is $l_{\mu\nu}$, named leptonic tensor. This term is given computing the Amplitude for the upper part of the diagram, which involve the incident and scattered electron:

$$l_{\mu\nu} = \overline{u}(k')\gamma_\nu(\not{k}_1 + m_e)\gamma_\mu u(k) \tag{2.8}$$

In this expression is immediate to recognize the feynmann rules for fermion vertex. The term $(k_1 \not+ m_e)$ comes from the fermion propagator of the internal electron, which is:

$$\frac{i(\not{p}+m)}{p^2+m^2}$$

The other term is $W^{\mu\nu}$, the hadronic tensor. For the elastic contribution this term is simply given by the feynmann rules for vertex with spin 0 particles, with the proper correction of the form factor, so we can write:

$$W_{\mu\nu} = \pi\delta((p+k-k_1)^2 - M^2)(2p+q_1)_\mu(2p'+q_2)_\nu \times Z^2 F_N(Q_1)F_N(Q_2) \tag{2.9}$$

At this point, one can substitute in the integral above, and compute the contribution of the transverse asymmetry due to the elastic term. This first terms scales with the nuclear charge $Z\alpha$, and this is important for electron scattering with heavy nuclei. However, this mechanism is important in the energy range of few MeV, and has a minor impact, although not negligible, for higher energy, such as the energy of interest for this thesis. For the inelastic contributions, the structure of the hadronic tensor is different. Realistic estimate are given only for nearly forward scattering angles. The hadronic tensor is given in terms of the structure functions $W_{1,2}$

$$W^{\mu\nu} = 2\pi W_1(\omega^2, Q_1^2)\Big(-g^{\mu\nu} + \frac{P^\mu q_1^\nu + P^\nu q_2^\mu}{(P\overline{K})} - \frac{q_1 q_2}{(P\overline{K})^2}P^\mu P^\nu\Big) \tag{2.10}$$

Several assumption are made to threat this new term. The structure function, for forward scattering angles, can be approximated by a function containing the Compton form factor of the nucleus, neglecting some dependence on $Q_{1,2}$ that let to simplify the integral in equation 2.6. It is beyond our scope to go into a detailed description, which can be found in the articles ([14], [12], [15]). We emphasize however that for the estimation of the inelastic intermediate state, theoretical calculation are affected by the approximation of forward angles and other assumptions due to lack of data in the dependence of some important variables, such as the Compton form factor for carbon 12, the Compton slope parameter and the use of the approximated Callavan-Gross relation. In summary, the theoretical prediction for the transverse asymmetry are reliable for small scattering angle, that correspond to lower values in transfer momentum Q; the experimental data measure by PREX [13] for ^1H, ^4He, and ^{12}C at Q values of 0.31 GeV, 0.28 GeV and 0.1 GeV, respectively, are in agreement with the theoretical prediction. The measurement performed at MAMI for ^{12}C [16] are with higher values of transfer momentum ($Q = 0.2$ GeV) and shows a discrete agreement with the theoretical prediction, considering also the systematic uncertainties associated to the poorly known Compton slope parameter. While the theory presented so far is quite successful in describing the data, it fails completely with ^{208}Pb. PREX report for lead 0 asymmetry. This strictly disagreement, although remove the presence of systematic effects due to the BNSSA for PV experiment, suggest to repeat the measure, besides being a theoretical challenge. Also for this reason, after the measurement with carbon, a new measurement of the transverse asymmetry with lead is scheduled.

2.1.2 Model Description

$$A_N = C_0 \cdot log(\frac{Q^2}{m_e^2 c^2})\frac{F_{Compton}(Q^2)}{F_{ch}(Q^2)} \tag{2.11}$$

2.2 Concept of the Experiment

We have seen so far how the Transverse Asymmetry is related to the interference between two scattering amplitude, and the theoretical model used to describe the process. The goal from an experimental point of view is to measure this quantity. The challenge is to obtain a valid measure of A_n, which is of the order of 20 part per million (ppm), taking into consideration all the possible effects that can interfere. To measure A_n, the straightforward method is to prepare an electron beam, with polarized electron, and send it to a fixed target. The scattered electrons are then collected by a detector placed at a certain angle, and now it's possible to obtain the transverse asymmetry applying the formula:

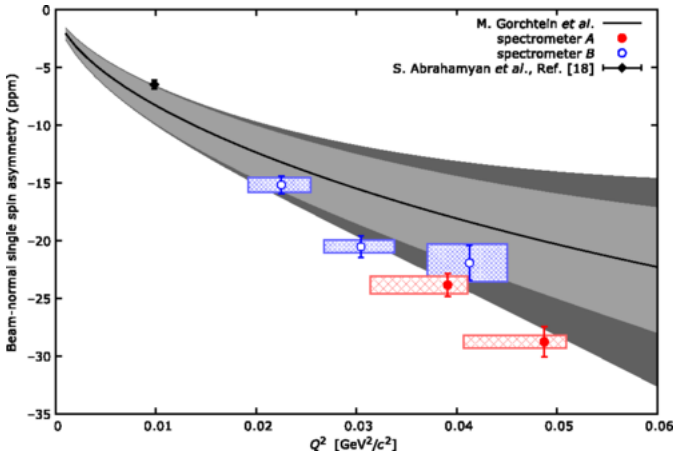

Figure 2.3: Transverse asymmetry measured at MAMI for ^{12}C target [16]. Theoretical calculation for $E_{beam} = 570\,\mathrm{MeV}$ is shown.

$$A_N(Q,p) = \frac{N_{\uparrow}(Q) - N_{\downarrow}(Q)}{N_{\uparrow}(Q) + N_{\downarrow}(Q)} \cdot (\frac{1}{p}) \tag{2.12}$$

where we have explained the dependence on the transmitted impulse, on the degree of polarization of the beam. In an experiment of this type, several requests are necessary to have an effective data acquisition:

- The accelerator must produce a polarized beam, stable over the time, with an high polarization percentage, in order to amplify the effect.
- The Beam energy needs to be quite stable, and should not depend on the Polarization state of the electrons. A change in the Beam energy associated with the polarization state can lead to a different count rate for $N_{\uparrow}$ and $N_{\downarrow}$, and would create an undesired contribution that adds to the A_n.
- The beam must be correctly aligned with the target, with a stable position. Again if the position of the target changes according to the polarization of the electrons, it will produce another contribution to the total asymmetry.
- The beam current should not depend on the polarization state of the electrons. If the beam source depends on the polarization, we will have a difference in the event rate and then another false asymmetry.
- it's necessary to reject possible double elastic scattering events, which may contribute to the total asymmetry.

All this demands can be satisfied with an accelerator that has stabilization devices with great precision and that can sustain high beam intensities. This last request is necessary to accumulate enough statistics to measure the transverse asymmetry with an accuracy about 1 ppm, in view of the future PV experiments. We can quantify how the statistical error varies according to the amount of data available. With the assumption that $N_{\uparrow,\downarrow}$ are gaussian distributed variables, we can compute the expected variance

$$Var[A_n] = \frac{1 - A^2}{N_{\uparrow} + N_{\downarrow}} \tag{2.13}$$

For a single measurement of the A_n. For multiple measurement n, the variance scales as $\frac{1}{n}$. Because A_n is expected to be smaller respect to 1, we can approximate the above formula:

$$V[A_n] = \frac{1}{2N \cdot n} \tag{2.14}$$

The error associated to the reconstructed asymmetry is the square root of the above quantity. If we impose that the error must be $\leq 1ppm$ we can easily obtain that the quantity $n \cdot N$:

$$n \cdot N \leq \frac{1}{2} \cdot 10^{12}$$

We will see later that achievable rates $N_{\uparrow,\downarrow}$ are in the range (20000,60000) counts per event for a carbon target. This number can not be increased at will by acting on the beam current. The first reason is oblivious: the beam source can produce only a certain amount of electrons before loosing, furthermore a beam with great intensity for an extended periods of time can damage the carbon target up to the risk of melting it. Another idea might be to increase the thickness of the target, to take advantage of the larger cross section. However this does not take into account that by doing so the number of double scattering event is increased. To avoid this the scientific community that deals with these nuclear physics measurements respect the convention that the target thickness should be less than the 10% of the radiation length of the material.

Chapter 3

Experimental setup

This chapter presents briefly the structure and the characteristics of the Mainz microtron accelerator (MAMI), where the experiment is setup and the transverse asymmetry is measured. Particular attention is given in the the description of the beam monitors that measure the beam parameters. Following an overview of MAMI and the acceleration stages, the experimental hall, the detectors and the electronic devices used to acquire and process the data are presented.

3.1 Overview of the Experiment

To measure the Beam-Normal single spin asymmetry, a polarized beam of 570 MeV is sent against a 10 mm thick ^{12}C target. The detectors consist of two fused-silica bars coupled to 3 (detector B) and 8 (detector A) PMTs, which collect the Cherenkov light emitted when an electron pass through the fused-silica. The detector are placed inside the two spectrometer of the A1 hall, whose standard detectors are not used in this experiment because of the high beam current (20 µA) that is above their limits of operation. The asymmetry between the two orientations of the electron spin is the goal of the measurement. The PMT signals are collected and digitalized by the **NINO** board, after a threshold selection, and sent to the A1 control room computer, where the DAQ program collect the data together with all the data coming from the beam monitors. The produced binary files are later analyzed by the analysis program, which is a significant part of the work done in the framework of the thesis. The data collected are divided in *events* made by 4 *sub-events* in sequence. Each event corresponds to a temporal window of $\simeq$ 80 ms, where each sub-event is 20 ms long. Here it is important to clarify that, unlike the majority of experiments in high energy physics, an event is not a single interaction, but is made by all the electrons interacting with the detectors during the specified time interval. The division into sub-events reflects the polarization sequence of the beam. The PMT counts and the beam monitor values are saved for each sub-event, along with the time length of the event (measured in clock cycles by the NINO electronic board) and other values which are required to process beam monitor data. The general structure of the event is the following:

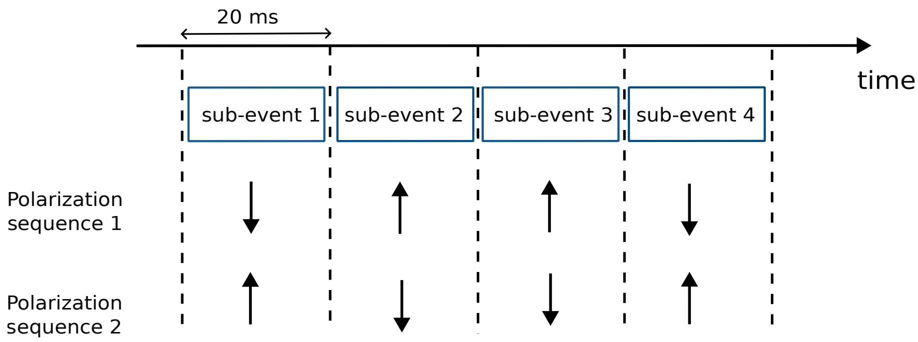

Figure 3.1: General structure of the event. The gate-length of each event is synchronized with the power grid frequency, to reduce possible effects of 50 Hz noise.

The particular choice of 20 ms for the sub-event is made to avoid undesirable effects generated by the power grid frequency (50 Hz). The gate-length of each sub-events is synchronized with the period of the power grid frequency: this ensures that an entire oscillation of the current of the power grid takes place within the same sub-event. This cancels out the 50 Hz noise and avoid to produce effects between nearby sub-events. For each event we have a single measurement of A_n, defined as the asymmetry between the $\uparrow$ and $\downarrow$ sub-events. It is important to avoid the creation of fake asymmetries by correlated noise or other external sources. For this reason polarization states are concatenate following the two patterns $\uparrow, \downarrow, \downarrow, \uparrow$. In addiction at the beginning of an event one of the two polarization pattern is selected using a De Bruijn sequence. A De Bruijn sequence of order n is defined as a cyclic sequence where every sub-sequence of length n appear only once. We have two different polarization pattern, the ones shown in the figure, that can be represented as 1 and 0. For this experiment, the De Bruijn sequence is of order $n = 6$ bits; this correspond to all the possible sequences of 1 and 0 with a length equal to 6, which are 64 different sub-sequence. It is possible to demonstrate that the number of exactly $N_{DeBruijn}$ sequences is:

$$N_{bruijn} = \frac{(k!)^{k^{n-1}}}{k^n}$$

If we substitute in the formula above $k = 2$ and $n = 6$, we have a total of $\simeq 67 \cdot 10^6$ different sequences. The seed of the De Bruijn sequence is generated with a pseudo random number generator, and the sequence is used to select between $\uparrow, \downarrow, \downarrow, \uparrow$ and $\downarrow, \uparrow, \uparrow, \downarrow$. At this point it could be objected why so much care is taken in choosing randomly the two sequences. At a first glance is certainly easier to select one of the two polarization pattern and reproduce it for every sub-event. However, this does not protect from systematic effects that arise from electronic or beam noise with frequencies similar to the frequency of the polarization pattern. An electronic noise, with a frequency roughly 10 Hz could in principle increase the rates for one polarizations state and decrease the other. The adopted solution to reduce possible effect is to randomize the pattern selection. In the end, there is another reason why a De Bruijn sequence is useful. During each polarization flip, we observe a short, transient reduction of the beam current. This reduction in the beam intensity has more influence on patterns where there are more inversion of the polarization respect to the other. With a De Bruijn sequence we ensure that we have a identical number of pairs of patterns, meaning that:

- 25% : $\uparrow, \downarrow, \downarrow, \uparrow$; $\uparrow, \downarrow, \downarrow, \uparrow$
- 25% : $\downarrow, \uparrow, \uparrow, \downarrow$; $\downarrow, \uparrow, \uparrow, \downarrow$
- 25% : $\downarrow, \uparrow, \uparrow, \downarrow$; $\uparrow, \downarrow, \downarrow, \uparrow$
- 25% : $\uparrow, \downarrow, \downarrow, \uparrow$; $\downarrow, \uparrow, \uparrow, \downarrow$

In the top rows we have 4 inversion, while in the two lower rows we have 5 inversion. Later we will describes the other details of the experiment; in the next sections we will present briefly MAMI accelerator, where the experiment is performed.

3.2 Mami

MAMI is the electron accelerator located in Mainz, which provides a continuous wave [1], high intensity, polarized beam for nuclear physics fixed-target experiments. The concept of the Mainz microtron accelerator was born in the early 1970s, when the researchers of the nuclear physics institute were investigating the possibility of generalizing the concept of the racetrack microtron (RTM), that consists in a linear accelerator (linac) and two deflection magnets (180° magnet, see figure 3.2). The particle recirculate, due to the deflection magnets, several time in the linac, and each time they gain energy. The goal of the collaboration which developed MAMI was to produce a continuous beam, with energies above 1 GeV and beam intensities up to 100 µA.

[1] The electron beam is made by bunches of electrons, in sequence. In MAMI the separation between subsequent bunches is so small that it is not possible, with the available instrumentation, to distinguish it from a continuous flow of particles.

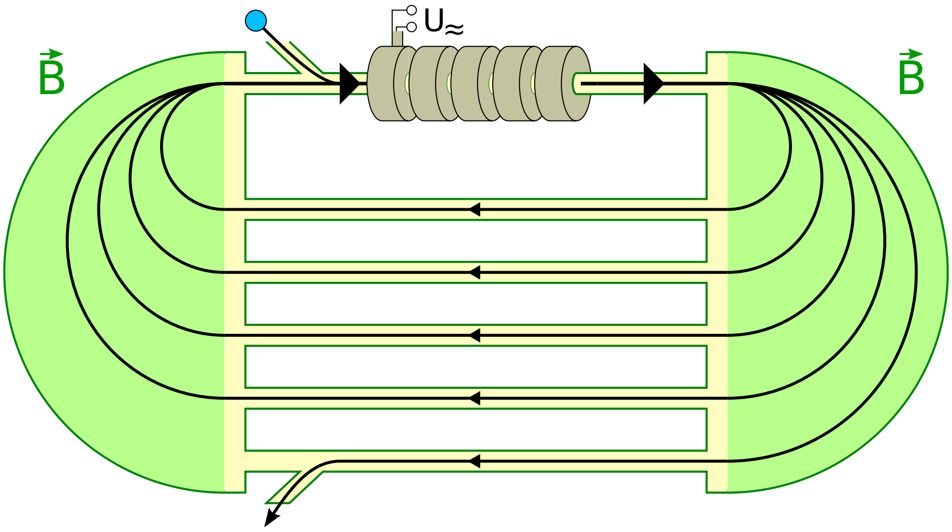

Figure 3.2: Racetrack Microtron. The particles are sent to the linac, and the two deflection magnets make the particles recirculate, until the momenta exceed the capability of the magnetic field.

A racetrack microtron, is characterized by the energy gain per-cycle δE given by the high-frequency electromagnetic field (HF). The energy gain for a single acceleration cavity of the linac is:

$$\delta E = eU_{Linac} \cdot cos(\phi)$$

U_{Linac} is the maximum voltage of the linac, and ϕ is the phase of the beam relative to the maximum of HF. Because the particle are accelerated by the linac, the beam consist in individual packets (bunches) whose rate correspond to the frequency of HF. In order for the electrons to be accelerated for each recirculation step, they must arrive at the beginning of the linac with the correct phase ϕ. Therefore the flight-time per cycle must be an integer or a multiple of the HF period. The time of flight is made of two terms: the first is the time that an electron needs to travel in the magnetic field of two 180° bending magnets, that is the cyclotron period, while the second term is given by the straight sections.

$$T = \frac{2\pi\gamma m_e}{qB} + \frac{L}{v} \tag{3.1}$$

where B is the magnetic field, q and m_e are the charge and mass of the electron, and L is the length of the straight section of the accelerator. The frequency is the given by the formula:

$$f = \frac{qB}{2\pi\gamma m_e + \frac{LqB}{v}} \tag{3.2}$$

From this overview two conclusion can be drawn:

- To accelerate slow electrons, with $\gamma = (1, 10)$, a magnetic field of 0.1 T is used, in order to work with frequencies of (2 GHz,4 GHz), that are easy to control. However with higher energies, and with a small magnetic field, the bending radii is higher and uneconomical.
- For high energy electrons $\gamma > 10$, to reduce the size of the deflection magnets, it is useful to increase the magnetic field up to 1 T of more, with the same band of frequencies $\simeq$ GHz.

These conclusions justify the structure of MAMI: a cascade of microtrons to reach each time higher energies with the same acceleration frequency at each stage. MAMI is composed by a sequence of 4 different microtrons, reaching 1.6 GeV.

The first stage, shown in figure 3.3, is composed by two small microtrons. The first microtron RTM1 accelerate the particles to 14 MeV in 18 revolutions. The electrons are then sent to the second

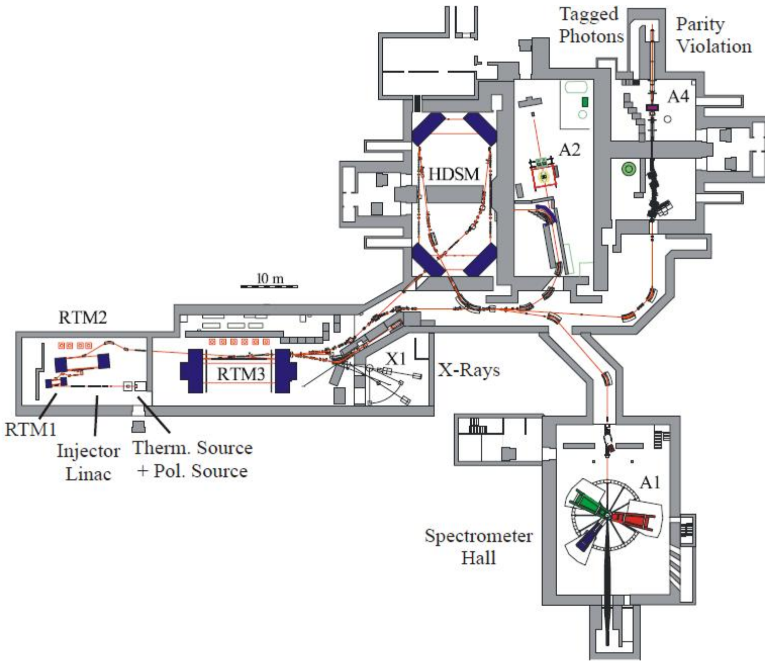

Figure 3.3: Scheme of the accelerator, with the different experimental halls. A third hall previously used for the A4 experiment, measuring the strange quark content of the proton, is now being used for the novel MESA accelerator and its experiments.

microtron that can accelerate up to 180 MeV. After passing the first stage, the beam is sent to the RTM3 (race track microtron 3), a large microtron with an end point energy of 855 MeV. These 3 microtrons forms MAMI-B, which started operation in 1990-91. A fourth stage, MAMI-C, was built and started operation in 2007. This fourth stage is made by 4 bending magnets, with a bending angle of 90°, and it is designed to achieve energies of 1.6 GeV. The design is different from the other race-track microtrons, and will not be explained, as it is not necessary for the experiment to reach such high energies.

The operation principles of a microtron are simple to be described. First we consider the gyro-radius for relativist electrons of energy E, that is:

$$r = \frac{E\beta}{qcB} \tag{3.3}$$

To have a coherent conditions, we must have that the flight-time $\tau = \frac{\lambda}{c}$ of the first recirculation must be an integer multiple of the HF wavelength $\lambda_{HF} = \frac{c}{f_{HF}}$, see equation 3.2. This means that:

$$\lambda = \tau c = \frac{2\pi cR}{\beta c} + \frac{Lc}{v} = \frac{2\pi E}{qB} + L = m\lambda_{HF}$$

For the other recirculation, we must have that the flight-time at energies $E_n = E_{n-1} + \delta E$ must be increased by an integer multiple of HF, too. This lead to the second equation:

$$\frac{2\pi\delta E}{qB} = n\lambda_{HF}$$

The minimum gain per cycle is then determined only by the strength of the magnetic field and wavelength λ_{HF}. These two equations together controls the dynamic of the race-track microtrons.

3.2.1 Polarized Beam

For the beam-normal single spin asymmetry a vertically polarized beam is necessary. At the MAMI electron accelerator it is possible to produce a vertically polarized beam with energy in the range

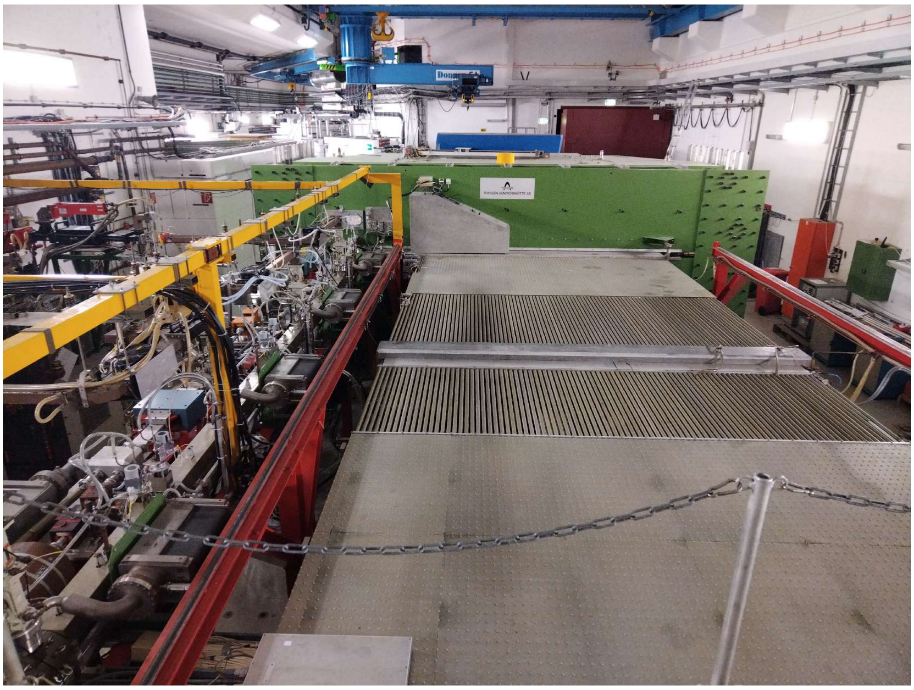

Figure 3.4: Picture of the Racetrack RTM3 in MAMI-B. The Green square at the bottom is one of the deflector magnets, the other one is below the point where the photo was taken. The linac stage is on the left. The tubes at the center of the figure are the paths that the particle cross during the recirculation. The further away from the linac the greater the energy.

180 MeV – 855 MeV [17]. In this section the procedure to orient the spin vertically is presented, following an explanation of how the degree of polarization is measured.

The electron source used at MAMI is made by a strained GaAs/GaAsP super-lattice photo-cathode illuminated by circularly polarized light. To alternate the sign of the light polarization, a fast Pockels cell ([18]) is installed in the optical system of the electron source. The Pockels cell is a wave plate controlled by the electric field, that changes the helicity of the photons impinging on the electrons. A Pockels cell exploits the Pockels effect, that affects crystal with particular characteristics (lack of inversion symmetry). For this type of materials the refractive index is linearly dependent on the applied electric field. By controlling the refractive index with the electric field, the polarization state of the incident light beam is altered. The extracted electron carries the same helicity of the incoming photon because of angular momentum conservation:

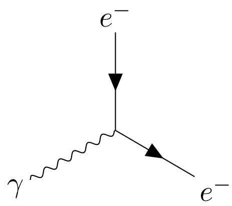

$$(Jz)_\gamma = \pm 1 \qquad (Jz)_{e^-} = \mp\frac{1}{2} \to \pm\frac{1}{2} \tag{3.4}$$

With the fast change of the Pockels cell it is possible to alternate the sign of the polarization. By the insertion of a $\lambda/2$ plate between the laser system and the photo-cathode the global polarization orientation of the electron beam can be reversed. This is particularly useful because this directly changes the sign of the asymmetry measured by the detectors, and allows to identify systematic errors. This is usually done for longer beam time, where two sets of data are taken, reversing the orientation of the $\lambda/2$ wave plate. By comparing the results for the two sets of data, the influence of the optical system on the asymmetry measurement is estimated and can be corrected for the final result of the asymmetry. During the beam time of interest for this thesis, the $\lambda/2$ wave plate orientation was fixed. The beam polarization achieved with this source is roughly $P = 80\%$, so the measured asymmetry are:

$$A_{measured} = P \cdot A_n$$

The polarizations of the electrons just extracted from the source is longitudinal. A magnetic field is needed to rotate $\vec{P}$ from longitudinal to transverse orientation. For this purpose two devices are used: the **Wien filter** and a double solenoid located in the injection beam line, close to the the optical source, as show in figure 3.5:

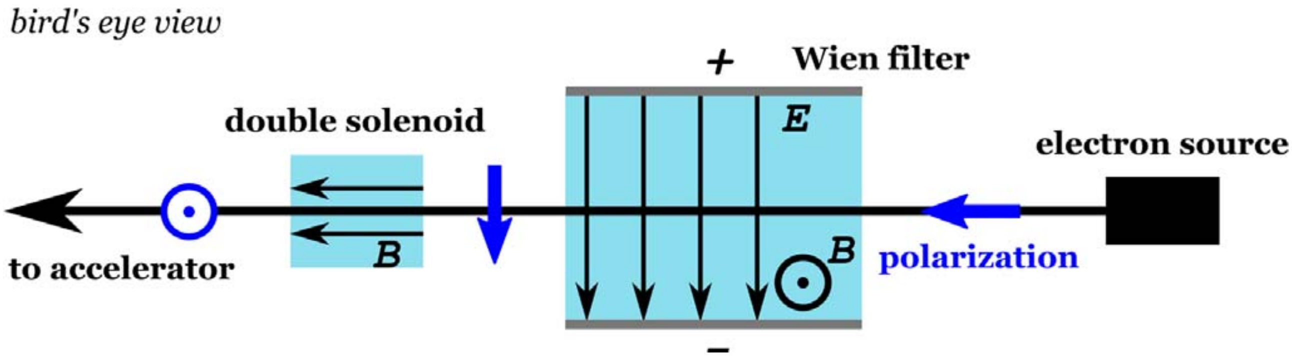

Figure 3.5: Beam line projection. This figure is taken from the paper [17]

Looking at the picture, the longitudinal direction corresponds to the Z axis. The X axis is parallel to the second blue arrow, just after the Wien filter, and the Y axis is orthogonal to the page. The spin is rotated primarily in the X direction, with a 90° rotation, then the subsequent double solenoid align the spin to the vertical direction, with another 90° rotation. Once the beam passes the double solenoid, the electrons go through the linac, the microtron and in the end to the experimental hall, where the target of the experiments is installed. During the acceleration stage, the spin follows the precession motion due to the various magnetic fields of the accelerator, as determined by the BMT equation. However in our experimental setup, the magnetic field of the various bending magnets that constitute the microtron-cascade are always parallel to the polarization in vertical direction, so that the cross product $\vec{B} \times \vec{P} = 0$, and the polarization remain constant. Only the residual horizontal component precedes during the motion. For conventional experiment that involve longitudinal polarization, after the first spin rotation due to Wien filter and the bending magnets, there is a further rotation to be considered, due to the motion of the particle during the acceleration and recirculation in the microtron. Because of this, the rotation made by the Wien is set in such a way that after the second rotation due to the motion in the accelerator, the polarization has the correct alignment in the experimental hall. The rotation angles of the polarization vector through the accelerator are known from simulations and are also directly measured for relevant energies, for a beam of 570 MeV the rotation angle is 55° with an accuracy of ±2°. In our case, this further rotation has only a small effect to the residual horizontal component. This horizontal component was accurately minimized by MAMI operators at the beginning of the beam time, and its effects the measurement are negligible. MAMI was not developed for experiments with transverse polarization. So it's not possible to measure directly the transverse component. However the vertical polarization is deduced from the determination of the total beam polarization and the residual horizontal components. For this purpose a Moller, Comport and Mott polarimeters are used.

3.2.2 Vertical Polarization Measurement

Three polarimeters are installed in MAMI: Mott, Møller and Compton polarimeters. Compton and Mott polarimeter are located behind the injector linear accelerator (see figure 3.3), close to the beam source, where the electrons, with an energy of 3.5 MeV, have already passed the Wien filter and the double solenoid. The Møller polarimeter, instead, is installed in the spectrometer hall, where the beam is delivered. The Møller polarimeter is sensitive only to the longitudinal component of the polarization, while the Mott and Compton polarimeter are sensitive to the Z and X component. When the beam is polarized longitudinally, the total polarization can be measured by a Møller polarimeter, in the spectrometers hall. The procedure for the alignment is the following: at the beginning of the beam time the Mott polarimeter is used for different settings of the solenoid field, with the Wien filter angle equal (nominal) to 90°. The aim is to minimize the horizontal polarization component (P_x) after the rotation performed by the double solenoid, changing the solenoid magnetic field. Then a second minimization follows, using the Møller polarimeter and changing Wien filter rotation angles. In this way we minimize also the longitudinal component (P_z). With the new Wien filter settings, another measurement is performed with the Mott polarimeter. With this procedure, the P_x and P_z components are completely minimized, with the result that the beam polarization is parallel to the Y axis. At this point, the polarization is correctly aligned, and the experiments can start. The last polarimeter, the Compton, is used to measure the variation of the degree of polarization during time.

In the last measurement of A_n at MAMI [16] the Moller and Mott polarimeters were available. In this way, it is also possible to estimate the systematic uncertainty for the degree of polarization, which is the relevant contribution to the total systematic uncertainty of the final measurements of A_n. The systematic effects obtained during the previous experiment were about $1\,ppm$. For the experiment described in this thesis, we performed the minimization described before only with the Mott polarimeter, obtaining a measure of the transverse polarization $P = 0.79\%$. This means that we could not estimate the systematic uncertainty of the polarization.

3.2.3 Mott Polarimeter

In this section we describe the theory of the Mott polarimeter. The Mott polarimeter exploits the asymmetry in the cross section due to the spin dependence. From the asymmetry we can to measure the polarization of the beam. Let's suppose that we have an electron beam that is sent towards a nucleus of charge Ze. We know from theory [19] that the spin of the incident electron interacts with the electromagnetic field produced by the nucleus. The magnetic field seen by a particle with speed $\vec{v}$ near a nucleus is:

$$\vec{B}_{nucleus} = \frac{-\vec{v} \times \vec{E}_{nucleus}}{c} = \frac{Ze}{mcr^3}\vec{L}$$

This magnetic field is coupled with the magnetic momenta of the electron μ_e.

$$V = -\vec{\mu} \cdot \vec{B}_{nucleus} = \frac{Ze}{mcr^3}\vec{L} \cdot \vec{S}_{e^-} \tag{3.5}$$

The second equation represents the spin-orbit interaction potential. This term yields the polarization dependence of the cross section. Let's consider an incident particle that scatters from a nucleus at an angle θ, as shown in the figure:

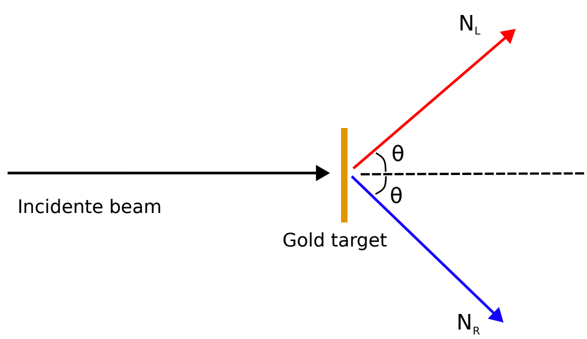

Figure 3.6: Scheme of the Mott scattering, the polarization is orthogonal to the plane, $\vec{n} = \frac{\vec{k} \times \vec{k'}}{|\vec{k} \times \vec{k'}|}$

The cross section can be modeled highlighting the dependencies on the polarization $\vec{P}$:

$$\frac{\partial \sigma(\theta)}{\partial \Omega} = I(\theta)[1 + S(\theta)\vec{P} \cdot \vec{n}] \tag{3.6}$$

In the equation above, the cross section is divided in two terms: $I\theta$ represents term that does not depend on the polarization, the second contains the dependence on the polarization, where $S(\theta)$ is the Sherman function, or the asymmetry function [19]. The unit vector $\vec{n}$ is normal to the scattering plane, and it is defined as:

$$\vec{n} = \frac{k \times k'}{|k \times k'|}$$

Where k and k' are the wave vectors associated with the incident and scattered electrons. The direction of $\vec{n}$ is parallel to the angular momentum L, and depends on whether scattering to the left or to the right is being considered. Let's suppose our initial beam has a polarization P, that can also be expressed as:

$$P = \frac{N_\uparrow - N_\downarrow}{N_\uparrow + N_\downarrow}$$

Where $N_\uparrow$ and $N_\downarrow$ are the number of electrons with spin up and spin down. The Mott polarimeter measure the number N of scattered electrons at a fixed angle θ, in the two directions right and left (figure 3.6). Using the equation 3.6, the scattered electrons to the left side N_L and to the right side N_R are equal to:

$$\begin{aligned} N_L &= N_\downarrow[1 + S(\theta)] + N_\uparrow[1 - S(\theta)] \\ N_R &= N_\uparrow[1 + S(\theta)] + N_\downarrow[1 - S(\theta)] \end{aligned}$$

The asymmetry $A(\theta)$ of the scattered electron between left (N_L) and right (N_R) is given by:

$$\begin{aligned} A(\theta) = \frac{N_L - N_R}{N_L + N_R} &= \frac{N_\downarrow(1 + S(\theta)) + N_\uparrow(1 - S(\theta)) - N_\uparrow(1 + S(\theta)) - N_\downarrow(1 - S(\theta))}{N_L + N_R} = \\ &= \frac{(N_\uparrow - N_\downarrow)}{(N_\uparrow + N_\downarrow)} S(\theta) = P \cdot S(\theta) \end{aligned}$$

The last step of the equation gives the beam polarization in terms of $A(\theta)$, the asymmetry measured by the Mott polarimeter, and the function $S(\theta)$, the Sherman function. The Mott polarimeter in MAMI, installed after the double solenoid, measures the scattering asymmetry $A(\theta)$ for electrons of 3.5 MeV with a thin gold target.

3.3 Experimental Hall Setup

Until now we have described how MAMI produce to accelerate the electrons, however we have not presented the structure where the beam is delivered and various experiments are carried out. MAMI experimental halls are named with the capital letter A followed with a number. In A2, for example, photo-nuclear reactions are studied to investigate the fundamental physics at the scale of nuclear dimensions. The experimental hall where the experiment described in this thesis is conducted is the A1 hall. We will describe briefly the main operating detectors that are installed and the details that are interesting for the transverse asymmetry measurement. In A1 hall the beam is delivered with energy in a range starting from 180 MeV up to 1.6 GeV. Energy greater than 855 MeV are reached with the last acceleration stage HDSM, shown in figure 3.3. Because the electron energy of our experiment is 570 MeV, the beam passes only through the first acceleration steps, and is extracted from the RTM3 and directly sent to the A1 experimental hall, without going through the HSDM stage.

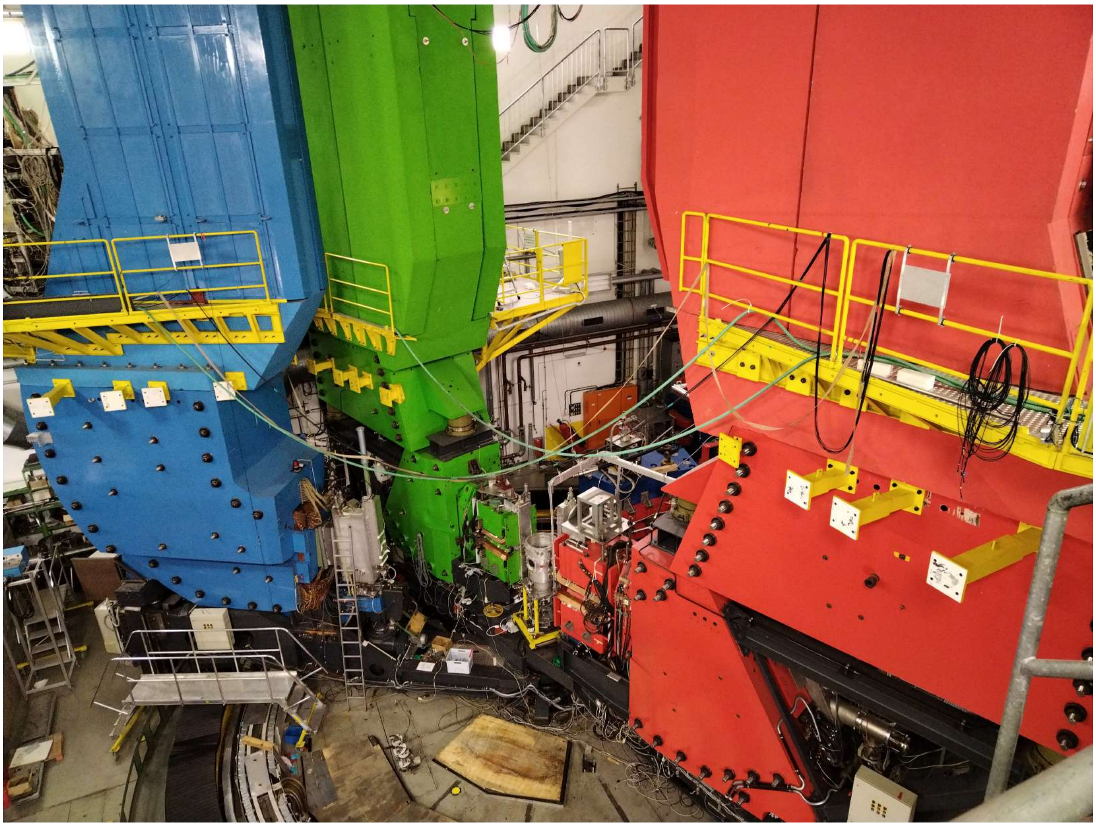

Figure 3.7: Picture of the A1 spectrometers hall, the spectrometers red and blue are used during this experiment. At the center of the picture is possible to observe the scattering chamber.

Inside A1 hall three large magnetic spectrometers are placed on a circular rail-track around the target chamber (figure 3.7). They where designed and built in 1993 to perform high precision measurement of electron scattering in coincidence with other hadron detection, with an high resolution in the determination of the particle momenta $\frac{\delta p}{p} < 10^{-4}$. The spectrometers develop vertically with a height of 15 m, for this reason the scattered electrons and the other particles are deflected with respect to the scattering plane with the use of magnetic fields. The figure 3.8 shows the path of the particles scattered from the target. The spectrometers used for the transverse asymmetry measurement are the red and blue ones. There are multiple reasons why the particle are deflected on the vertical direction, we summarized them in two points:

- reason of space, due to the fact that a horizontal setup would not fit with the dimension of the building in addiction to the fact that this would not allow to rotate the spectrometers by a variety of angles that the vertical orientation does
- reduce background and noise, in fact the high beam intensity that is possible to reach at MAMI

is a source of noise and background event which can be cut off detecting the particle far from the interaction point.

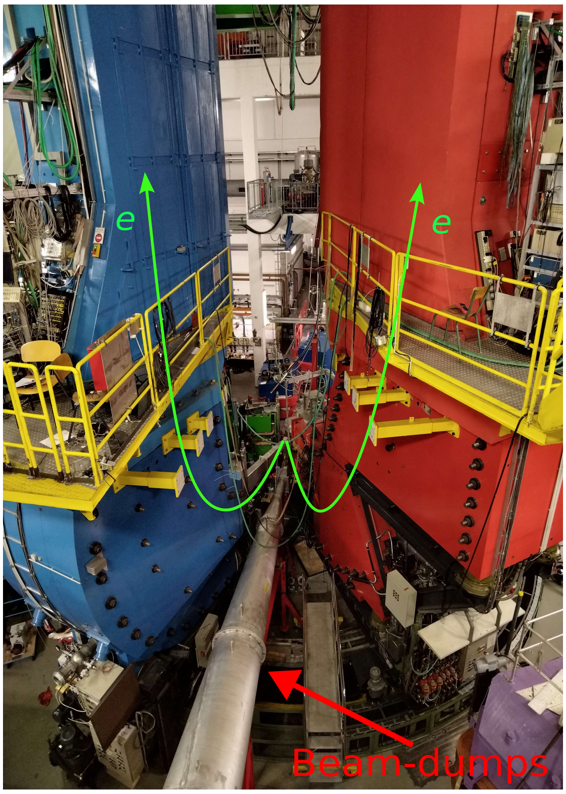

Figure 3.8: Image of the spectrometers of A1 hall. The spectrometers can be rotated using a system of rail-tracks that are visible at the bottom of the image. The electrons are scattered and then deflected in the vertical direction by the magnetic field (green lines). This picture is taken from behind the target. The target is roughly at the center of the image where the two green lines join. The electron are coming from the opposite direction, with respect to the spectrometers.

Once a particle is scattered in the acceptance region of the spectrometers, it is deflected by the magnetic field and passes through the drift chamber, which occupies the first third in height of the spectrometers. When the particle is at the height of the platform in the figure 3.8, it impinges on a layer of plastic scintillator, and after that a Cherenkov detector measures the particle speed v. In figure 3.9 the spectrometer A internal, taken during the installation of detector A, is shown. The determination of both the particle speed v and momenta (drift chamber) allows particle identification.

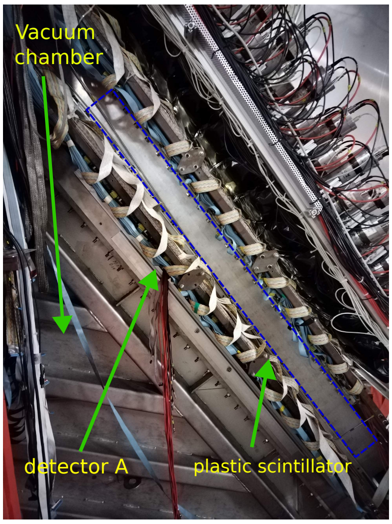

Figure 3.9: Internal of the spectrometer. This image was taken during the installation of the detector A inside the red spectrometer, that is accessible from the platforms visible in the picture 3.8

Despite the possibilities offered by the already existing setup, for the beam time of interest none of these components was used directly in the estimation of A_n. The reason is due to the high intensity of the beam that is used in the experiment, which is far from the optimal operating conditions of the components, that are suited for rates lower than the ones expected for beam normal single spin measurements. The spectrometers are used indirectly, for the alignment of scattered electrons to our detection system.

3.4 Detector Description

In this section we will describe the electronics and the detectors used to measure the transverse spin asymmetry. For this experiment we are going to measure the transverse asymmetry at one fixed angle, corresponding to a transferred momentum of $Q = 0.2\,\text{GeV}$. The electrons detection is made via two thin blocks of fused-silica that are coupled to PMTs. When a scattered electron hits the fused-silica (refractive index $n = 1.45$) Cherenkov light is emitted. The emitted Cherenkov light can extract one electron in the photocathode, which will be amplified by the PMT dynode structure. This sequence of event triggers the PMT and produce an output signal.

In the experiment two detectors are installed and read-out independently. The detector A is placed at an angle of $+\theta$, while detector B is placed at $-\theta$. We expect to measure the same absolute value of the transverse asymmetry, with an opposite sign due to the different orientation. The two detector are made by 3 PMTs and 8 PMTs coupled with two blocks of fused-silica, as shown in 3.10.

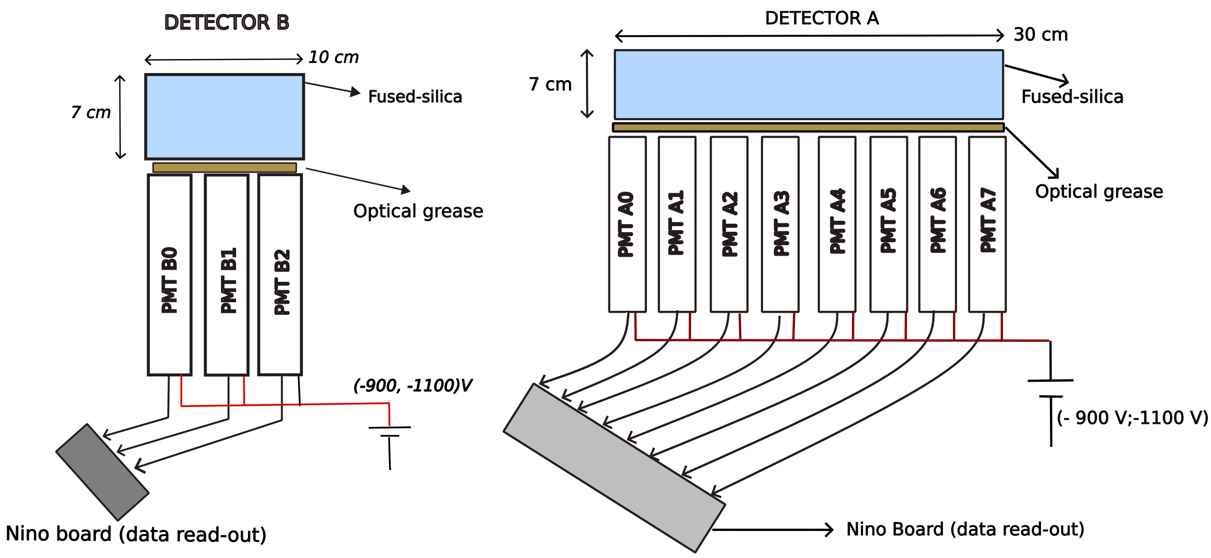

(a) *Detector B* (b) *Detector A*

Figure 3.10: Detector A and B scheme. Each PMT is coupled to the same fused silica bar. The PMTs located at the edges of the fused-silica bars are expected to measure lower rates with respect to the PMTs located near the center. The output signals have negative voltage and are read out by the NINO board.

These two detectors are placed inside the spectrometers presented in 3.8, between the top of the drift-chamber, which occupies the first third in height of the spectrometer, and just below the panel of scintillator. During the experiment, the drift chamber of the spectrometers is turn off, and also the PMTs coupled to the spectrometer scintillators are not powered. As we mentioned above, the scattered electron are deflected in the vertical direction by the magnetic field of the spectrometer. It is important to mention the differences between the new and the old electronic setup. In the old electronic setup the output signal of the PMTs was integrated during the time interval of each sub-event, and therefore the single scattered electron could not be counted. The advantage of this method is that the electronics is simpler. However, this old method is affected by a baseline noise and it is not good for the future experiments with lead target, where the expected rates are lower than the rates on carbon. With the new electronics, the single electrons are counted, and this will enable the future measurements with lead, improving the accuracy.

Here we report the characteristic of the two detector that are relevant for the data analysis:

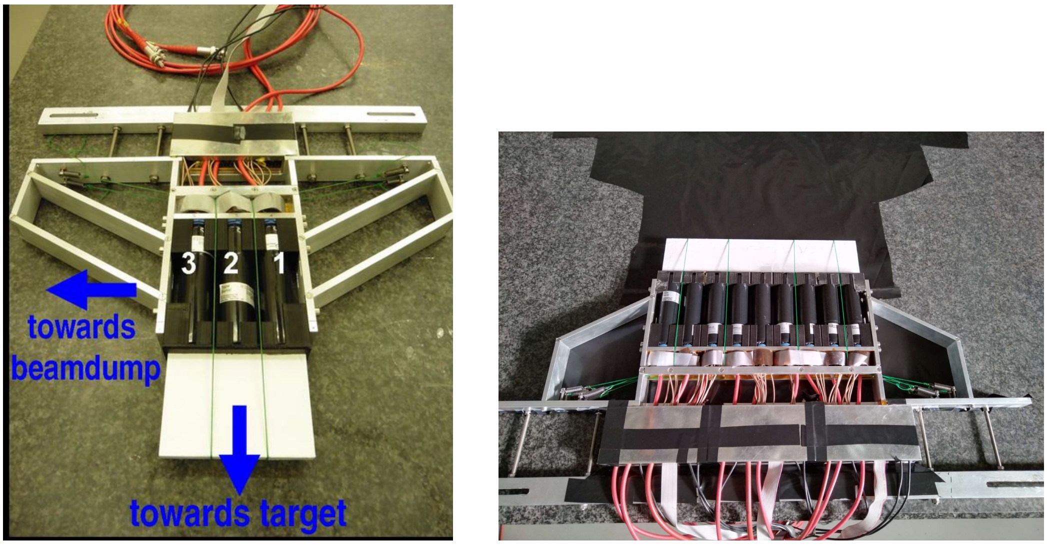

(a) *Detector B* (b) *Detector A*

Figure 3.11: Picture of the two detector taken in the clean room. The white blocks are the fused silica bars that produces the Cherenkov light, the cylinders below are the PMTs, triggered by the passage of the particle.

- detector B size: $7\,\mathrm{cm} \times 10\,\mathrm{cm} \times 1\,\mathrm{cm}$
- detector A size: $7\,\mathrm{cm} \times 30\,\mathrm{cm} \times 1\,\mathrm{cm}$
- Number of dynodes of the PMT: 12
- The Power voltage for the PMT in negative, in the range of $(-900\,\mathrm{V}, -1100\,\mathrm{V})$
- refraction index n of the fused-silica is 1.45.
- maximum gain of $22 \cdot 10^6$.

The Pmts are coupled to the fused-silica with an optical grease suited for ultraviolet light. The PMTs positioned at the center of the fused-silica bar an effective area that is larger respect to the PMTs at the edge and their rates are expected to be higher compared with other PMTs.

3.5 Beam Monitors

In MAMI, several monitors are placed along the beam line to check the beam quality and measure parameters such as current intensity, energy and relative position of the beam. This section summarizes the operating principles of the monitors installed at MAMI. Some details will be given in the appendix, for a complete discussion please refer to the following paper [20]. The monitors available at MAMI are constitutes by resonant cavities. With the resonant cavities it is possible to measure the various quantities, with the underlying physical principle that the passage of charged particles through these cavities excites some electromagnetic resonant modes[2] (see figure 3.12) which can be detected and analyzed by an analog circuit to measure the beam parameters. Before going into the details, it is necessary to define some quantities that will be used later in the discussion. We define the Shunt-impedance r_s as:

$$r_s = \frac{|V_{\|}|^2}{P} \tag{3.7}$$

Where P is the power absorbed by the cavity when a particle excites one of the resonant mode, and $V_{\|}$ is defined as the effective voltage experienced by a charged particle along a straight line, which can be computed as:

[2] TM mode, where the magnetic field is completely transverse respect to particle momenta

$$V_{\parallel} = \frac{1}{q}\int_{s_0}^{s^1} \vec{E}_s \cdot d\vec{s}$$

The Shunt impedance is a measure of the interaction strength between a cavity and a charged particle, and can also be expressed using the Q value of the cavity, the maximum energy stored W and the frequency of resonance f_r:

$$r_s = \frac{|V_{\parallel}|^2 Q}{2\pi f_r W}$$

When the beam travels through the cavity, the particles lose energy that excites the mode. The power P_{HF} extracted from the beam is related to the beam current:

$$P = i^2 r_s \tag{3.8}$$

Where i is the beam current. An antenna is used to decouple part of the energy from the cavity and send it to a circuit which produces an analog output signal. Indicating with κ the coupling constant of the antenna, the previous relation needs to be modified introducing a new factor $\frac{\kappa}{(1+\kappa)^2}$. In a cylindrical resonator, the type installed at MAMI, the resonance frequencies of the different oscillation modes are expressed by the formula:

$$f_{m,n,p} = \frac{c}{2\pi\sqrt{\epsilon_r \mu_r}}\sqrt{\left(\frac{x_{m,n}}{R}\right)^2 + \left(\frac{p\pi}{L}\right)^2}$$

The constant in the formula are:

- c is the light speed.
- ϵ_r, μ_r are the magnetic and dielectric constant of the material.
- $x_{m,n}$ it the n-th zero of the m-th Bessel function.
- R and L are the radius of the cylindrical cavity and his length.

This formula can be obtained solving the Maxwell equations with cylindrical boundary condition. If the frequency of the beam bunch is equal to the resonant frequency $f_{m,n,p}$ of the cavity, a TM mode is excited. At MAMI high quality monitors are installed, with a $Q \simeq 10000$, that means that $\frac{\nu}{\delta\nu} \simeq 10000$. This means that the frequency of the beam buch must be very close to the frequency of the resonant cavity. At MAMI the frequency used for all the resonators is 2.449 532 GHz or a multiple of it. The beam bunch frequency is the same, and it is controlled by the MAMI-master oscillation signal, that is the reference signal for all the MAMI monitors.

Depending on the TM mode excited, we have a different signal in the cavity, so a different signal collected by the antenna. The relevant quantity that is detected is the power P_{HF} absorbed by the antenna, that is proportional to the power loss P of the beam. For the TM_{010} mode, the power absorbed by the antenna is:

$$P_{HF} = i^2 r_{010} \frac{\kappa}{(1+\kappa)^2} \tag{3.9}$$

Where κ is a coupling constant between the electromagnetic field of the cavity and the antenna. The power absorbed by the antenna is directly dependent on the beam current. Because the values are typically in the range of pW to mW, the signal is processed in close proximity of the installed monitors. In the signal processing, the input signal of the antenna in coupled to the master-oscillation signal, so the output signal is given by the formula:

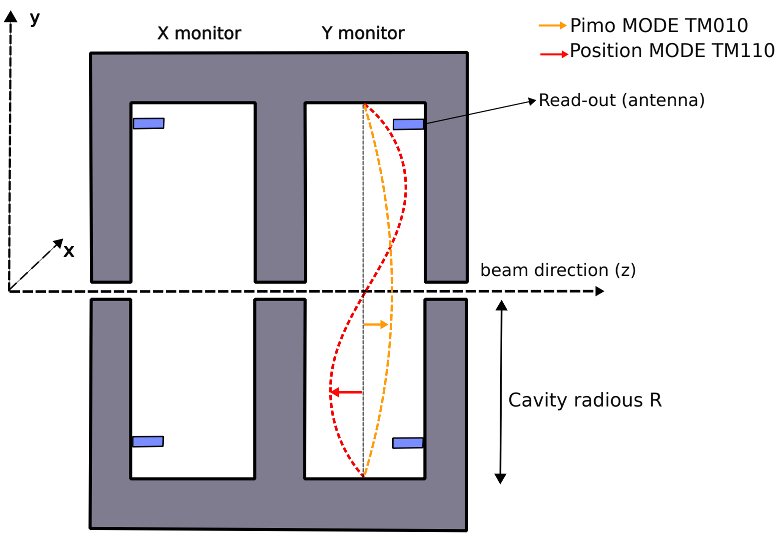

Figure 3.12: Scheme of the Cylindrical cavities installed at MAMI. In red we have the TM_{110} mode, used to measure the position of the beam, in yellow the TM_{010} mode, to measure the intensity of the beam.

$$U = \sqrt{P_{HF}} \cos(\phi - \phi_{LO}) \tag{3.10}$$

where the phase ϕ is the phase of the resonant mode or the phase of the beam bunch, while the phase ϕ_{LO} is the phase respect to the master-oscillation signal, and can be adjusted by a phase shifter in the circuit. The output voltage signal can be read out with the oscilloscope or digitalized and saved with other devices. To measure the beam intensity is important to minimize $\phi - \phi_{LO}$ (see figure 3.13), to maximize the signal amplitude.

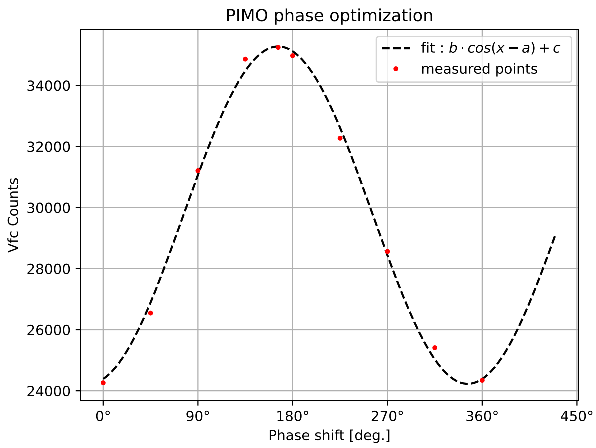

Figure 3.13: Plot of the phase ϕ versus the output signal. The phase optimization was done selecting the working point in correspondence of the peak.

The measurement of the x, y position follows in principle the same procedure. In this case the TM_{110} is acquired. The reason is clear, because it is possible to calculate that for this mode the r_{shunt} is proportional to the beam position on the x, y plane. So The power absorbed by the antenna can be written:

$$P_{HF} = i^2 r_{110} \frac{\kappa}{(1+\kappa)^2} K x^2 \tag{3.11}$$

The output signal, that is read by our setup, is proportional to the square root of the absorbed power:

$$U = \sqrt{P_{HF}} = constant \cdot i \cdot x \tag{3.12}$$

The beam parameter are then given inverting the above formula

$$x \propto \frac{\sqrt{P_{HF}}}{i} \tag{3.13}$$

Where the exact conversion coefficients are not known, and are determined during the calibration phase, at the beginning of the beam time. To measure the beam energy, a different approach is used. The energy monitor (ENMO) consists of 2 cavities in the RTM3. One is located in the last recirculation pipe, the other one on the part of the beam line, where the acceleration takes place. The two monitors are synchronized to the master oscillation and measure the phase of the bunches of electrons. During their travel from the first cavity to the second cavity, the beam passes through the magnet and does one half turn. If the energy is slightly higher, the radius of the turn will be slightly larger. This means that there is an extra time between the two bunches, that can be measured as a small phase shift in the 570 MeV recirculation. From this it is possible to obtain a value for the difference of the actual energy from the nominal energy.

3.5.1 Beam stabilization

The beam stabilization is an essential component of the experiment. The values of A_n that we want to measure are in the order of $10\,ppm$, so it is important to reduce other contributions that can be related to variations in the beam parameters. The beam stabilization at MAMI is achieved a control program. The beam monitors constantly measure the beam parameters and the control program receives the measurements from the monitors and calculates consequently the corrections to be performed. The beam position in the transverse plane is constantly adjusted by the magnets in the beam line. For beam current and energy, the control program acts on the laser of the beam source and the klystrons in the three racetrack microtrons described in section 3.3. Two types of stabilization are made by the control program: the first is made to avoid long term drifts by pulling back the beam back to nominal conditions every $\simeq 10$ s. Simultaneously, a fast stabilization prevents fast fluctuation, reacting quickly to every disturbance of the beam.

3.6 Electronics

3.6.1 Voltage to Frequency Converter

Some beam parameters are needed in order to take into account possible effects in the measurement of the transverse asymmetry. The relevant data are the position in the (x, y) plane, the incident angles on the target, the current and energy of the beam. All this values are collected using the already existing monitors. To collect the data from the monitors, single and multichannel, synchronous voltage-to-frequency converters (AD7742) are used. This devices contain an analog modulator that is able to convert the input voltage into an output pulse train, whose frequency is proportional to the input voltage.

The VFCs are powered with an external voltage of 5 V. They measure an input voltage in the range of $(-V_{ref}, V_{ref})$. An external clock signal, with a frequency $F_{CLKIN} = 5.88$ MHz is created externally and synchronous to the gate-length. The analog input signal is sampled with by a switched capacitor, with a rate that is equal to F_{CLKIN}. The comparator produces a number pulses; the frequency of the output signal is proportional to the input voltage, with $-V_{ref}$ equal to $5\% \cdot f_{CLKIN}$ and $+V_{ref}$ equal to $45\% \cdot f_{CLKIN}$ [21], where the first correspond to 0.0 V in input and the second to V_{ref} (see figure 3.14). The data are acquired counting the number of pulses from the comparator, which are proportional to the frequency, so we can substitute to f the number of pulses, and we end up with the equation 3.14

$$V_{in} = V_{ref}[2 \cdot \frac{N_{pulses} - 5\% N_{CLKIN}}{40\% N_{CLKN}} - 1] \tag{3.14}$$

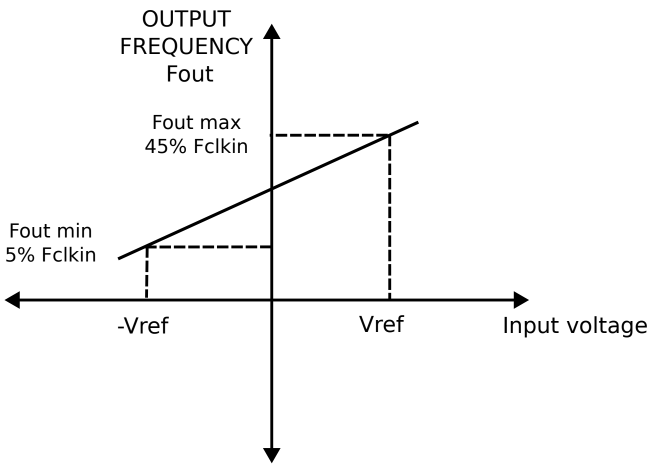

Figure 3.14: Frequency versus Voltage

3.6.2 Master Board

The VFCs described in the previous section are measuring the beam parameters along the beam line. A figure of the beam line is in section 4.3.2, where the various position of the monitors is shown. The data collected by the VFCs are firstly acquired by the master board, in figure 3.15, and then sent to the A1 computer, which will produce the data package. The VFCs are synchronized by the master board clock, with a frequency of 5.88 MHz. This is also the reference frequency for the VFCs output signal.

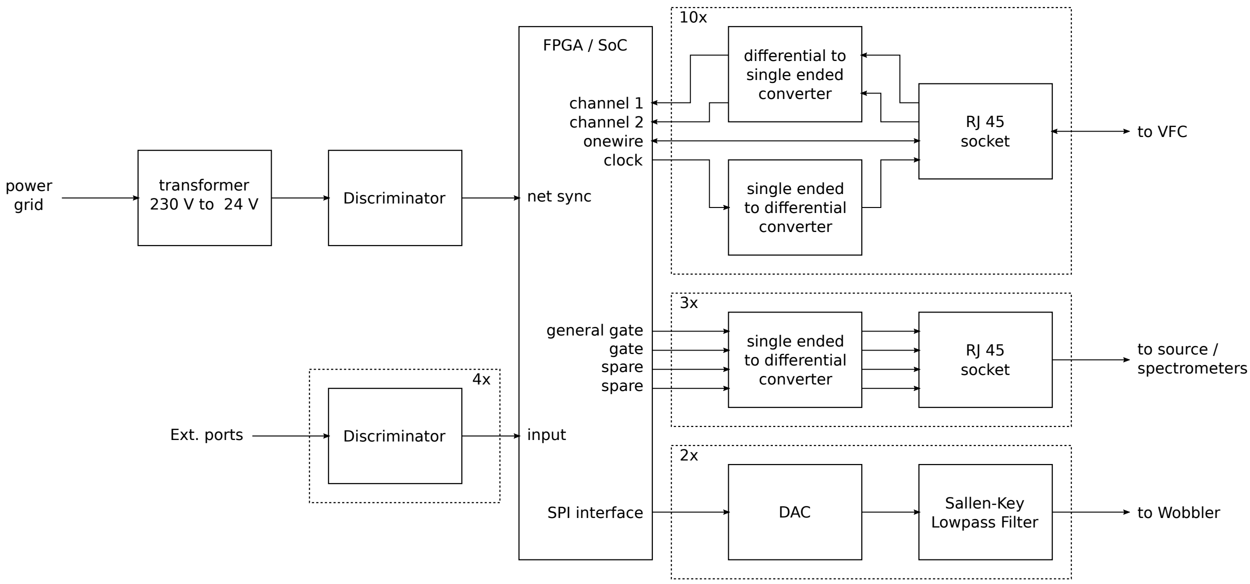

Figure 3.15: Scheme of the master-board, the device that coordinates all the electronics for the experiments, and send the data to the computer in the control room.

The *onewire* is a special bus which will be used in future for temperature measurement in the VFC, to check if there are temperature drift and effects on the outputs signals. The master board sends also the gate length signal to the MAMI source, where the polarized beam is generated, and to the detectors, needed to communicate and synchronize the sub-events. For experiment with lead target, the master board will also controls the one of the magnets (*wobbler 16*, in figure 4.5). With lead target, the beam position is constantly changed, artificially. Consequently the beam hitting point on the target is varying, to avoid melting. In the end, the master board is synchronized to the power grid, is order to reduce possible systematics effect connected to the 50 Hz frequency, as discussed in section 3.1.

3.6.3 Nino Board

The NINO board 3.17 is our data acquisition system for the PMT counts (see paper [22], for a reference). It is made by 32 analog input channels and it is powered with ±5 V. Each input channel receive a differential signal from the detector, and has attenuation circuit that reduces the amplitude of the input signal. After passing the attenuator, the signal is sent to the input stage (see figure 3.16) of the NINO chip, a current-to-voltage converter, that produces an output signal whose amplitude is proportional to the total charge of the input signal.

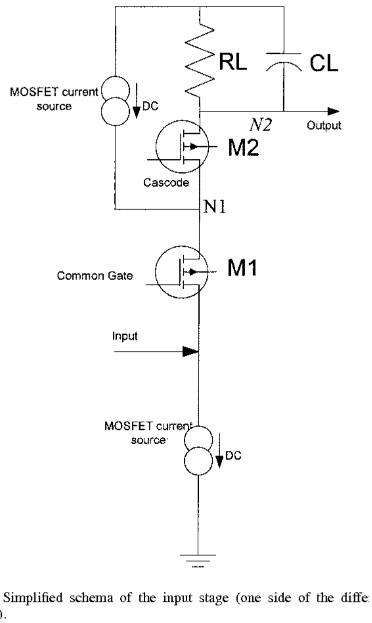

Figure 3.16: Input stage of the NINO chip. The input signal coming from the detector passes an attenuation circuit, and then are sent to the input stage, in this figure. The output, at node N2, is connected to the discriminator and an amplification stage.

After passing the input stage, the signal pass through a discriminator and a block of 4 operational amplifiers. There are 4 discriminator in the NINO chip, and each of them can handle signals coming from 8 different channels. The discriminator selects the signals by a threshold values in V.

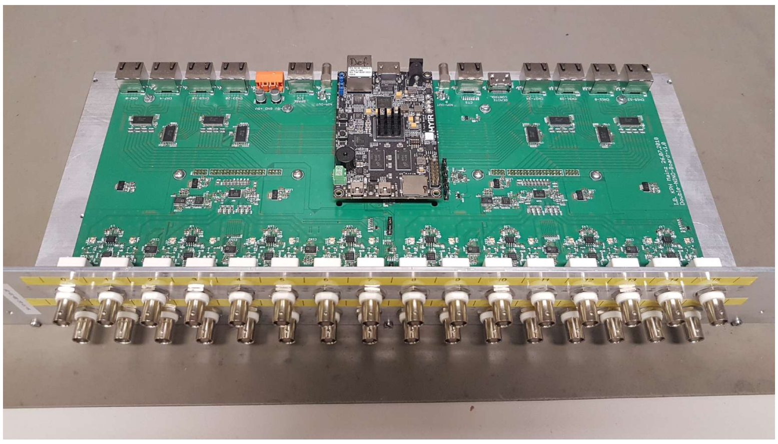

Figure 3.17: Nino Board, The input channels are at the bottom of the figure.

However, the signal that arrives to the discriminator is proportional to the input charge of the signal coming from the detector, so in the end the NINO board is sensitive to the input charge.

The discriminator threshold can be set in the range of (10 pA, 100 pA). The output signal after the discriminator and the amplification block is a LVDS (low voltage differential signaling) with a fixed shape, and a width that is proportional to the input charge. Regarding the data acquisition system, two values are import to control the discriminator threshold and the attenuator, and are named *Thr* and *Att*, respectively. The NINO chip is designed in such a way that the *Thr* value is shared by 4 adjacent channels. On the contrary each channel has is own value of *Att*. Acting simultaneously on *Thr* and *Att* is possible to define a global threshold for each channel, individually. These two parameters are set in the DAQ program, using 12 bit DACs, corresponding to interval of $(0; 4095)$. *Thr* selects the threshold of the discriminator. The *Att* value controls the input voltage of attenuator: the higher is the value of *Att*, the lower is the attenuation of the signal. Two Nino board are used in the experiment, one for detector A and one for detector B. For the experiment discussed in this thesis, we will use only 8 channel for detector A and 3 channel for detector B, since this is the number of the input signals coming from the two detectors. For the future experiments more channels will be used, splitting the analog input signal in 4, and sending it to 4 different input channel of the board. This is useful because changing individually the attenuation value, we can define 4 different thresholds for the same signal and compare different values of threshold, to study how the noise affects the measurement, finding the best compromise between signal to noise ratio. The *Thr* and *Att* selection is explained in chapter 4.

Chapter 4

Detectors Test, Alignment and Calibration.

In this chapter we discuss the electronic test that have been carried out in the laboratory, and the calibrations needed in order to calculate, from the raw data, the quantities needed for the analysis. The test in the lab consisted in checking that the photo-multipliers and the data acquisition electronics. The calibrations consist in the determination of the scaling factors, needed by the analysis program, to convert the raw data collected by the *VFC*s to data in physical units. The important beam parameters are the impact point coordinates of the beam X, Y, the beam energy E, the beam current I and the scattering angles θ_x and θ_y. In the end, we discuss the auto-calibration procedure, to remove non-desired effects due to the presence of an offset in the PMTs counts.

4.1 Nino Board

In this section we study the characteristics of the Nino board, which digitizes the signal from the PMTs. The NINO board has two parameters: *Thr*, that controls the discriminator and *Att*, which controls the attenuator circuit. These parameters are part of the settings of the DAQ program which controls the NINO board. Because the values of *Thr* and *Att* are defined in arbitrary units, it is desirable to find a conversion formula to obtain the value of the threshold in physical units, as mV. Because of the NINO sensitivity to the input charge, it is not simple to define a unique value for the threshold in mV, because the input charge of the detector signal depend on the shape, amplitude and time length. For example, signal with a large time and a small amplitude can generate the same charge with respect to narrow signal with high voltage amplitude. Despite this, some data have been acquired by the A1 collaboration, with which it's possible to define a raw conversion function from attenuation units to threshold. The idea behind is to generate, with a wave generator, signals with fixed time length and shape, varying only the amplitude, and use them as input of the NINO board. The data available were collected following this procedure. Unfortunately, these data were taken with an input signal shape that different from the signal shape of our experiment [1]. We are aware that the conversion formula obtained with these data is only a rough estimation, however it can be useful to get an idea of the threshold values, in mV.

The data shown represent the values of the amplitude of the input signals (in mV) versus the values of *Att*, and are taken for a fixed value of $Att = 750$. The function used for the conversion is obtained from the fit of the data, the function used is the following:

$$Threshold\,[\mathrm{mV}] = \frac{a}{(att-b)^3} + c \tag{4.1}$$

The parameters of the formula are estimated using the function *curve-fit* of the python library *schipy*:

- $a = -802111053\,\frac{\mathrm{mV}}{[arb.unit]}$

[1] Apart from this, it is not even true that the shape of the signals produced by the detectors is constant.

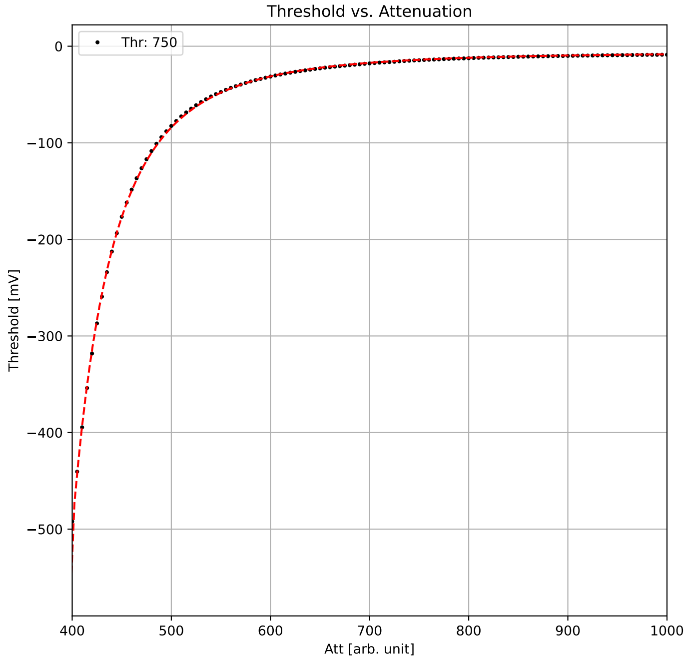

Figure 4.1: Threshold dependence versus attenuation. The input signals have a fixed shape and time length. The data are collected following this procedure: with a fixed amplitude of signal, the *Att* is set to 4000, the maximum, and decreased progressively, until the NINO board starts missing some pulses. All the data are acquired with a fixed value of *Thr* = 750.

- $b = 382\,[arb.unit]$
- $c = -6.1\,\mathrm{mV}$

As we can see, the relation between threshold and *Att* is not linear. Around the values 400 - 700 we observe high variability. For values higher than 700, the threshold is low and almost constant. This mean that the attenuation, controlled by the attenuator in the input channel of the NINO board, is reduced progressively as *Att* increases.

4.2 Detector Test

Before the Beam time, some test with the two detectors were performed, to check that the PMTs were still working after some years of inactivity, and that the new electronics was able to count properly the pulses and store the data. For this studies, we didn't have a radioactive sources to employ. Anyway the signal shape using radioactive sources is expected to be different from signal of the 570 MeV electrons used in the experiment. The typical energies of nuclear decay are in the order of $E \simeq 1\,\mathrm{MeV}$, with consequently only a small production of Cherenkov light, difficult to detect. A different approach is followed, using cosmic rays rate as a probe. The cosmic rays are able to produce Cherenkov light in the fused-silica bars, in fact the refractive index is $n = 1.45$, and a particle emits Cherenkov light when its $\beta = \frac{v}{c}$ is more than $\frac{1}{n} = 0.69$. The principal component of the cosmic rays at sea level is made by muons, produced in the electromagnetic and hadronic showers in high atmosphere. The energy of the muons reaching sea level is about 4 GeV, β for these particles is:

$$\beta_\mu = \frac{p}{E} = \frac{\sqrt{E^2 - m_\mu^2}}{E^2} \simeq 0.99 \tag{4.2}$$

The muons are relativistic and their speed is over the threshold for Cherenkov light production. Knowing that the expected number of event for cosmic rays is about $1\frac{event}{\mathrm{cm}^2\mathrm{min}}$ we can compute the expected values for the number of events. We decided to take 1 minute long acquisition for both the two detectors, this leads to 70 expected events for detector B and 210 events for detector A. These values are a rough estimate, because the effective area seen by the each PMT is less than the total area of the fused-silica bar. The rates measured in the laboratory are $\simeq 60$ for detector B and $\simeq 100$ for detector A. The first step is to select a good work point for the threshold. So, fixing the value of the threshold parameter for the NINO board, we took several acquisitions, each of them one minute long, increasing the attenuation (figure 4.2). We powered the PMTs with a negative voltage around -1000 V, as suggested in the data-sheet, and covered the Cherenkov detector with a shielding blanket, to avoid ambient light simulating a signal.

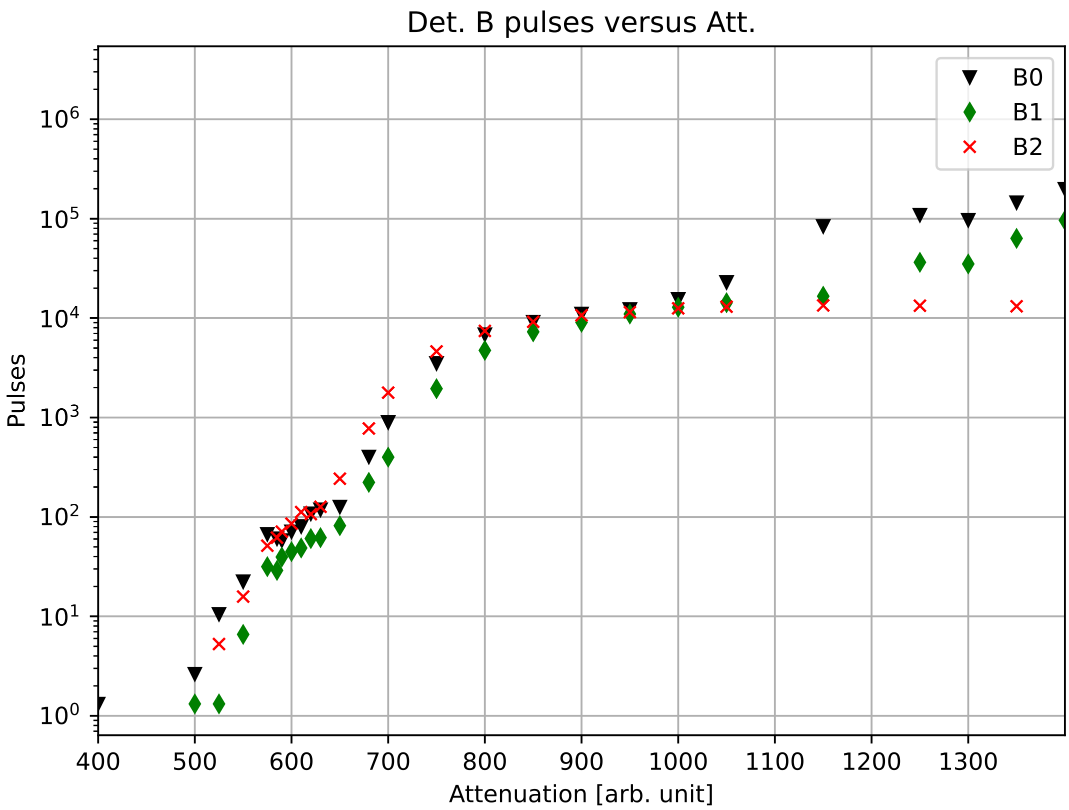

Figure 4.2: Attenuation scan for Detector B.

We observed a small knee, around the zone of $580 - 600$ of *Att*, where the number of counts was almost constant, roughly equal to the number of expected events from muons hitting the detector. Then we observe a big edge for attenuation = 700. Looking at the plot 4.1, we assume that the attenuation values are so high that electronic noise is no longer rejected, in fact the counts grow enormously. The *Att* was set at 600 as a starting point for the experiment. Once the attenuation is set, we have studied the statistical fluctuation of the counts. 10 acquisitions, each of them 1 min long are collected and reported in table 4.1.

These data are interesting, we can check if the counts are following the theoretical distribution of the events expected for cosmic rays at sea level. If the PMTs are working well, we know that the number of counts should be Poisson-distributed:

$$Pdf(\mu, k) = \frac{\mu^k}{k!} e^{-\mu} \tag{4.3}$$

The variance of the Poisson distribution is equal to the mean of the counts, and we expect the same behaviour also for the sample mean and the sample variance, the values are computed and reported in table 4.2

We report also the correlation C_{ij} between the PMTs. The result are fine: we are able to see a positive correlation between adjacent PMT, and as expected the correlation is lower in the case of

$n°$ acquisition	B0	B1	B2
1	58	60	62
2	62	55	59
3	61	59	70
4	73	66	70
5	68	66	56
6	59	52	64
7	69	74	77
8	48	49	57
9	70	54	58
10	60	61	66

Table 4.1: Detector B counts for 10 acquisition of 1 min long, with *Att* equal to 600.

PMT	μ	σ^2	Correlation C_{ij}
1	62.8	54.4	$C_{11} = 0.66$
2	59.6	57.2	$C_{23} = 0.65$
3	63.9	47.0	$C_{13} = 0.35$

Table 4.2: Mean, variance and correlation coefficient for detector B and PMT in overlap.

the more distant. This is explained by the lower probability that the photons of Cherenkov radiation light up at the same time pmts that are far away from each other. We can test that the data follow a Poisson distribution using the well-known Gosset test, defined as:

$$\chi^2_{n-1} = \sum_{i=1}^{n} \frac{(Obs_i - Exp_i)}{Exp_i} \tag{4.4}$$

where *Obs* are the observed counts, and *Exp* are the expected counts. We report the results for detector B in table 4.3. The test shows that there is good agreement with the hypothesis that the count are Poisson-distributed.

Pmt:	1	2	3
χ^2_9	8.52	8.45	6.37

Table 4.3: Gosset test for detector B

At this point, to convince oneself that the detector B is measuring signals given by the passage of cosmic rays, and not only noise, a fourth PMT (a spare component left in the lab) was used. This other PMT is coupled to a small block of fused silica (5 cm × 5 cm), and was placed in overlap with detector B, roughly in correspondence of B2. Unfortunately, the DAQ is not designed to take coincidences, so a different procedure is needed to check is the PMTs are triggered by the same passage of particles. We have acquired 10 acquisition one minute long, as before, measuring the counts of detector B and a PMT in overlap, . This different PMT is indicated with *Ov*. It is useful to compute the correlation coefficient: if a positive correlation between the counts is observed, then a certain number of signals is triggered by the same passage of particles. The result for detector B are reported in table 4.4:

The sample mean, the variance and the correlation between the detector B and the PMT in overlap are reported in table 4.5.

A positive correlation is measured for all the PMTs of detector B. This indicates that a certain amount of signal are detected simultaneously.

	B0	B1	B2	PMT in overlap
χ^2_9	8.95	6.44	10.96	9.52

The same procedure was followed also for detector A (see figure 4.3). We analyzed 4 signal at a time, because during these lab test we had only one NINO board, with only 4 channels available.

$n°$ acquisition	B0	B1	B2	Ov
1	63	57	72	28
2	55	51	64	18
3	62	53	75	27
4	71	62	75	33
5	68	59	49	23
6	57	55	63	18
7	70	64	64	24
8	50	69	69	25
9	65	62	62	19
10	74	71	77	28

Table 4.4: Detector B counts for 10 acquisitions of 1 min long, with PMT Ov in overlap.

PMT	μ	σ^2	Correlation
1	63.5	58.9	0.49
2	60.3	43.3	0.38
3	67.0	71.1	0.65

Table 4.5: Mean, variance and correlation coefficient for detector B and PMT in overlap.

The tests for the set of PMTs (A7,A6,A5,A4,A3) showed good result: the distribution of the counts was in agreement with the expected and the correlation coefficient between nearby PMTs and the PMT is overlap was different from zero and positive. For the set of PMTs (A2,A1,A0), some issues have emerged. Primarily the counts did not vary during the scan in *Att* and this has made impossible to identify a value for the *Att*. To study the behaviour of the counts, once again 10 acquisitions were acquired, and are reported in 4.6.

$n°$ acquisition	A2	A1	A0	Ov
1	91	51	50	27
2	86	61	50	7
3	58	48	45	18
4	95	62	41	29
5	69	60	50	21
6	85	57	45	19
7	66	51	46	28
8	74	51	48	22
9	77	43	45	17
10	62	44	50	29

Table 4.6: PMTs A2,A1,A0 counts for 10 acquisition of 1 min long.

The mean, variance and correlation between the PMTs counts is reported in table 4.7:

PMT	μ	σ^2	Correlation
2	76.3	160	C_{21} = 0.55
1	52.8	47.5	C_{10} = -0.10
0	47.0	9.6	C_{20} = -0.22
Ov	21.7	48.2	

Table 4.7: Mean, variance and correlation coefficient for detector A and PMT in overlap.

The variance σ^2 for A0 and A2 are quite different from the expected mean μ. The Gosset test for this data are reported in table: 4.8

The expected error for the result of this test is $\sigma = \sqrt{2 \cdot (n-1)} \simeq 4$. In this case we are observing

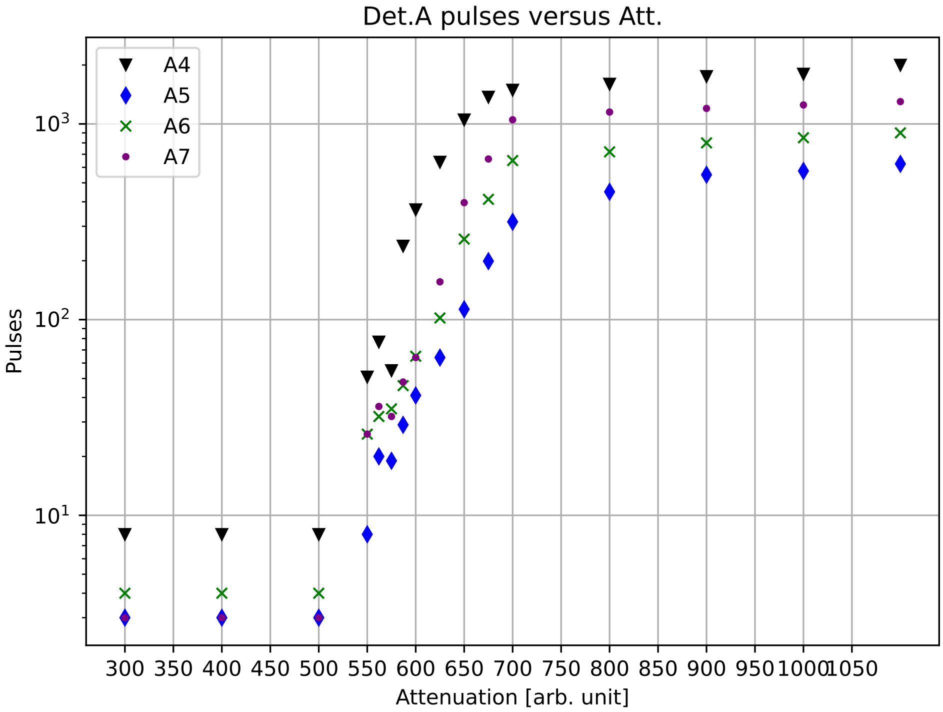

Figure 4.3: Attenuation scan for Detector A, for the pmt 4-5-6-7

Pmt:	A2	A1	A0	PMT in overlap
χ^2_9	19.6	8.30	1.90	39.5

Table 4.8: Gosset Test for PMTs A2,A1,A0 of detector A.

3 values that are more than $3 \cdot \sigma$ far from the expected value. If we look at the correlation matrix :

pmt:	Ov	0	1	2
Ov	1	-0.18	-0.21	-0.06
0	-0.18	1	-0.10	-0.22
1	-0.21	-0.10	1	0.56
2	-0.06	-0.22	0.56	1

Table 4.9: Correlation coefficient between the PMTs (A2,A1,A0) and the PMT in overlap.

We observe negative correlation between the pmts, something not expected. After some investigations, we find out that the program which controls the NINO board had a bug: the program partially overwrote some detector B settings for detector A as well. Since detector B has only three pmt's, the problem affected the PMT's with the same numbering as detector A. After fixing this issue we repeated the same test, without finding any problem.

4.3 Calibration

For the transverse asymmetry on ^{12}C represent an ideal test for the new electronic system. Previous measurements of the A_n have been performed at MAMI for carbon target ([16]). For this experiment, the red spectrometer is placed at the angle of $+22.5°$, and the blue one at $-22.5°$, respect to the longitudinal direction. For these two angle, we have the same kinematics and Q^2 values of the previous measurement. The Q^2 value was measured for a low current beam ($I = 5\,\mathrm{nA}$) with the spectrometers detectors. The Q^2 values are reported with and without rejecting the inelastic scattered electrons. The inelastic scattered electrons rejected imposing an energy threshold.

$$
\begin{array}{lll}
det.A: & Q^2 = 0.0413\,\mathrm{GeV}^2 & \text{without Cut} \\
det.A: & Q^2 = 0.0395\,\mathrm{GeV}^2 & \text{with Cut} \\
det.B: & Q^2 = 0.041\,\mathrm{GeV}^2 & \text{without Cut} \\
det.B: & Q^2 = 0.041\,\mathrm{GeV}^2 & \text{with Cut}
\end{array}
$$

The Q^2 values is the same of the last measurement performed at MAMI, and is measured with and without rejecting the inelastic electrons.

4.3.1 Alignment of the Scattering Plane.

The scattered electrons are deflected upward by the magnetic field inside the spectrometers A and B. However, the spectrometer detectors and systems are not directly used to measure the transverse asymmetry, due to the high current intensity, which would damage the electronics. Instead of the spectrometer detectors, the scattered electrons are measured by the two detectors A and B, described in section 3.4, installed between the drift chamber and the scintillator panel (see figure 3.9). So the scattered particles must be aligned to the fused-silica bars, primarily. This procedure is performed using a low current mode of the beam ($I = 5\,\mathrm{nA}$). For this mode the spectrometer systems can be used to detect the particles. Because we know the position of our detector A and B inside the spectrometers, we can use the Cherenkov detector to visualize where the electrons are deflected. Changing the configuration of the magnetic field, the electrons trajectory is oriented in such a way that is intersects the detectors A and B. For detector A the scattered electron beam has been aligned to pass over the fused silica, in correspondence of pmt A7. For detector B the same procedure was done, aligning the scattered beam in correspondence of pmt B0. Once we achieved a good alignment, we turned off the spectrometers system, performing the other necessary calibrations with only detector A and B.

4.3.2 Beam Monitor Calibration, XY Monitor

For the calibration of the X Y monitors, special targets are used. In the target frame (see figure 4.4) there are two targets made by three carbon wires that are mounted at a known distance from each other, horizontally and vertically aligned.

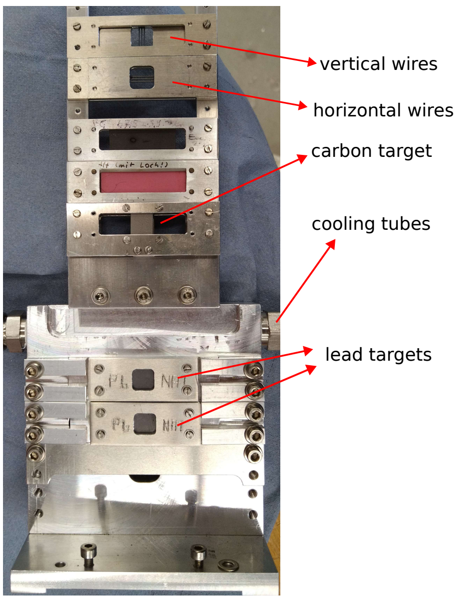

Figure 4.4: Target frame, on the top the three carbon wires that are used to calibrate the positions monitors. Then the carbon target and two lead targets.

The distance between the center of the two external wires is measured, and it is equal to $d_{horizontal} = 2.38\,\mathrm{mm}$ for the horizontal wires and $d_{vertical} = 2.33\,\mathrm{mm}$ for the other one. The procedure to measure the scaling factor used to convert from the raw-data in V to µm, is the following: we ask MAMI operators to slowly change the beam position, in the horizontal and vertical direction for the horizontal and vertical target. The beam position can be changed by varying the magnetic field produced by the *Wobbler 16* magnets (see figure 4.5). During this slow variation, the detectors measure the rate of scattered electrons, that increases when the beam hits one of the three wires and decreases when the beam is centered between two wires. We plot the detector counts versus the XY monitors values, in voltage, and we estimate the position of the two external peaks. This values can be used, together with the distance $d_{horizontal}, d_{vertical}$ already measured, to compute the scaling factors. This procedure is repeated for $X21/Y21$ and $X25/Y25$ monitors. We plot the PMT rate versus the $X25, X21, Y25, Y21$, given in V. To identify the three peaks in of the carbon target, we fit the data using a gaussian model (see figure 4.6). The mean μ represents the center of the wire, given in V. Looking at the Beam line, we assume that the beam travels in a straight line. Let's consider the *Wobbler 16* magnet the "0" of a coordinate system, with the z axis pointing to the target (left direction in the beam scheme).

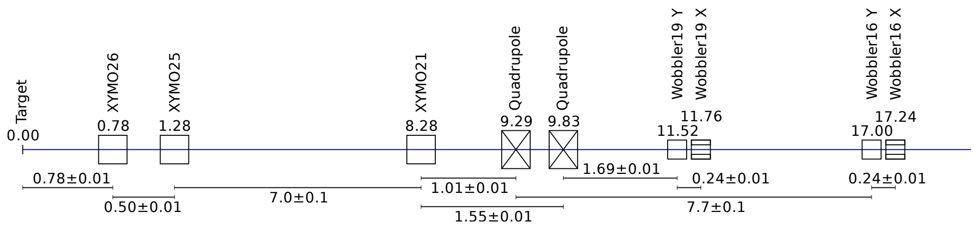

Figure 4.5: Beam line scheme.

The Beam parameters are measured by the Monitors $X/Y_{21}, X/Y_{25}$, which are located at some distance respect to the target. Suppose we are working only with the Y_{25} monitor (the procedure is the same for the others). The Beam y position is described by:

$$Y_{beam} = m \cdot (Z - Z_{wobbler16})$$

In the scheme 4.5 the distance between the various monitor is reported. The longitudinal distance between Y_{25} monitor and the *wobbler 16* magnet is $Z - Z_{wobbler16} = 1.57\,\mathrm{m}$. The Position on the target is given by $Y_{target} = m \cdot Z_{target}$. With these simple equations then:

$$c_{Y25} = \frac{d_{vertical}[\mathrm{mm}]}{Y_{target}} \tag{4.5}$$

c_{Y25} indicates the scaling factor of the monitor. This procedure is repeated and the scaling factor c_{Y25}, c_{Y21} , c_{X25}, c_{X21} are measured. The analysis program uses these quantities to compute the beam position on the target, and from that the incident angles in the X, Y directions, which are needed for the analysis.

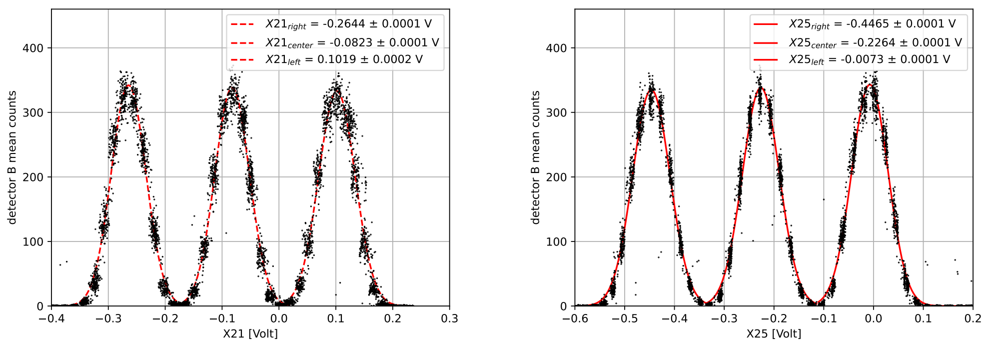

(a) (b)

Figure 4.6: Plot of the averaged count of detector B, with the slow variations of the beam position in the horizontal direction. The three peaks occur when the beam is aligned with the center of the wire. The values on the X axis are in V

With the scaling factor, the analysis program can calculate X and Y values in the correct physical units. The final result are reported in the plot 4.7; the distance between the two external peaks in the PMT counts are in agreement with the distance $d_x = 2.38\,\mathrm{mm}$.

For brevity, we report only the plot for the X position. The result for Y are analogous. The position X and Y are computed combining the values measured by the two monitors (see figure 4.8).

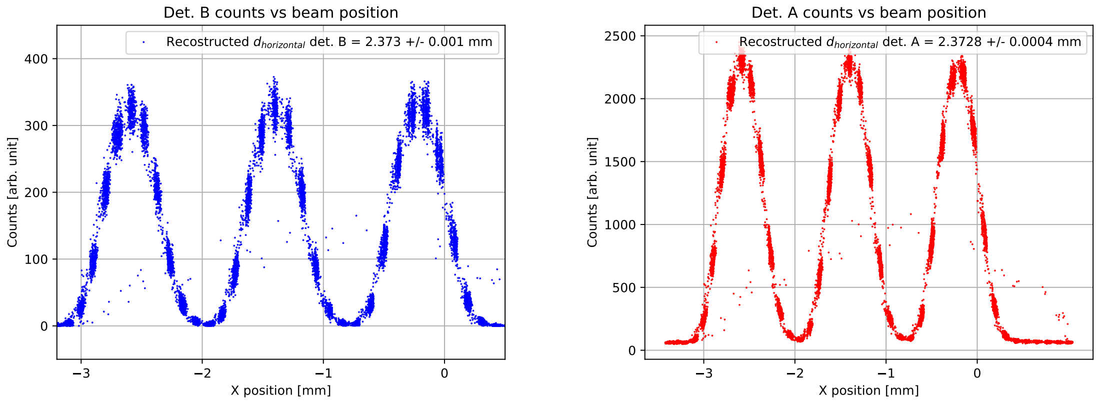

Figure 4.7: plot of the PMT Count against the physical values computed by the analysis program. Now the position of the three peaks correspond to the expected values measured for the target.

For the calculation of the position the reference system has the origin coincident to the center of the target. The beam trajectory is described by the following equation:

$$y = m_y \cdot z + q_y$$
$$x = m_x \cdot z + q_x$$

q_x and q_y, that are the intercepts, are the desired quantities. Imposing in the above equations the passage through the points (Z_{25};X_{25}) and (Z_{21};X_{21}) (identical procedure for Y) we can resolve the system for q_x, obtaining:

$$q_x = \frac{Z_{25} \cdot X_{21} - Z_{21} \cdot X_{25}}{Z_{25} - Z_{21}} \tag{4.6}$$

the solution for q_y is identical. The scattering angles θ_x and θ_y are instead related to the slope m, knowing that $tan(\theta) = m$. The angles are given by the formula:

$$\theta_x = \frac{X_{25} - X_{21}}{Z_{25} - Z_{21}} \tag{4.7}$$

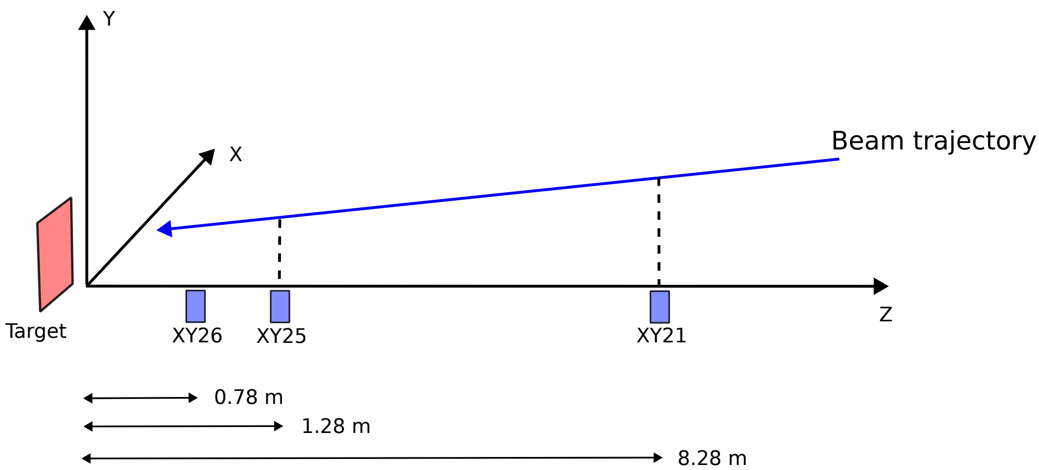

Figure 4.8: Figure of the beam trajectory, the position X and Y are measured by the monitors (blue boxes). Assuming a linear motion of the particles, the hitting positions on the target are computed.

4.3.3 Current (PIMO) Calibration

The last two calibration needed for the analysis are the energy and the current of the beam, which are indicated with PIMO (current monitor) and ENMO (energy monitor). The values that we measure are given by VFCs counts, that are explained in section 3.6.1. We need to determine the scaling factor and possible offsets to convert these quantities in physical units. For this beam time the current is measured in µA and the beam energy is given in keV.

For the current monitors I13 and I21, the raw counts are converted in digitalized voltage values with the formula shown in equation 3.14. The relation between these values given in V and the real values in µA and eV is linear:

$$I(\mu\text{A}) = mI(\text{V}) + q$$

To determine the two coefficients, the beam current was raised from 10 µA to 22 µA in several step. For each step we compare the nominal values of the current with the values in V measured. The following plot show the procedure described:

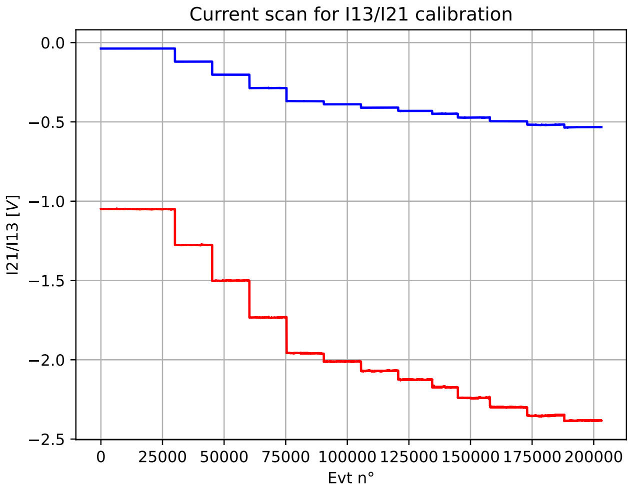

Figure 4.9: Current scan for the calibration, each step correspond to a run with a different beam current. The x axis represents the number of the event analyzed, and each event is 80 ms long.

The calibrations consist in retrieving m and q with a linear fit. Then the parameters are added in the standard configuration file, together with the other calibration parameters, and can be loaded by the analysis program to process the data.

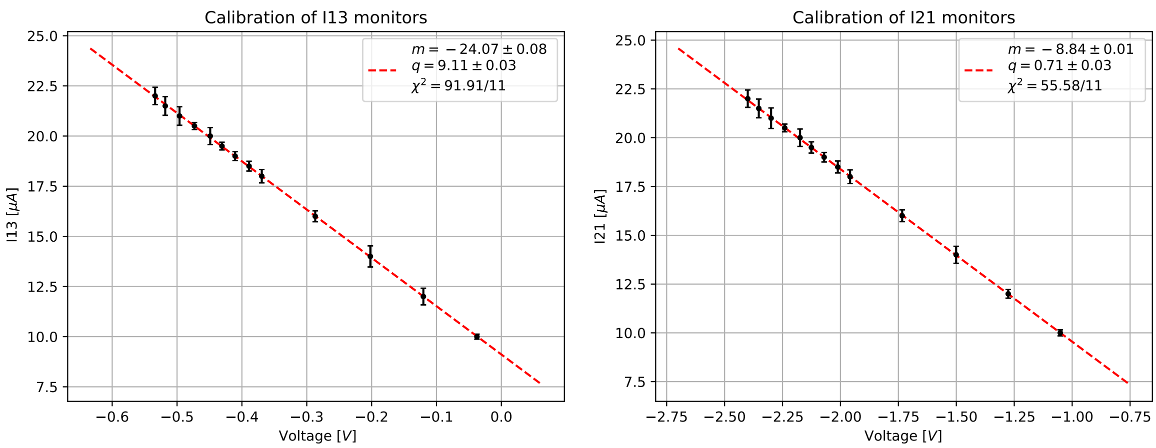

Figure 4.10: Calibrations plots for PIMO I21 and PIMO I13, the errors are multiplied by 25.

The values obtained from the fit of nominal beam current vs. voltage values are shown in the figure 4.10. The χ^2 values are higher than the expected. This is not unexpected, the errors in both the plots are computed with the sampling standard deviation formula applied to the sequence of voltage values $I21\, I13$ (σ_{vfc}, the standard deviation computed for each step in plot 4.9), and it is related to precision of the analog to digital converter VFCs. The errors are then propagated to the y axis showed in the plot. Yet, we are underestimating the error associated with nominal current I, in fact the accuracy associated with the beam current, set by the accelerator operators is not known, and we suspect that is not negligible compared to σ_{VFCs}.

4.3.4 Energy Monitor (ENMO) calibration.

The ENMO calibration is performed in a different way from the other monitors. The energy calibrations are performed by MAMI operators, and exploit the polarity signal which controls the beam polarization at the source of the acceleration. MAMI operators use the signal to create artificially a difference in the beam energy that is correlated to the beam polarization, with the last two sub-events having a higher energy with respect to the first two. The energy difference is nominally 22.6 keV. Because we know the nominal difference, the calibration consist in computing the correct scaling factor which convert from V to keV. The quantity that is relevant for the calibration is δE (with E_{18} being the energy monitor) is:

$$\delta E = \frac{E_{18}[2] + E_{18}[3]}{2} - \frac{E_{18}[0] + E_{18}[1]}{2}$$

An histogram of δE should show a single peak whose values correspond to 22.6 keV. For this calibration, we took 3 different acquisition, which differ for the different values of the beam current. We remind that, as the output voltage signal from the XY monitor, also the energy monitor is proportional to the current, as mentioned in equation 3.13. The relation between energy E keV and the signal amplitude of the energy monitor U V is given by equation 4.8

$$E\,[\mathrm{keV}] = c_E \cdot \frac{U\,[\mathrm{V}]}{i} \tag{4.8}$$

So, if we invert the relation we have that:

$$c_E = \frac{E}{U} \cdot i \tag{4.9}$$

This is the final formula to compute the correct conversion factor for the energy monitor. For this calibration we have 3 different acquisition, that differs only for the beam current. For one acquisition we set the beam current to 0, to observe the presence of an offset. For the other two we set the current to 15 µA and 20 µA.

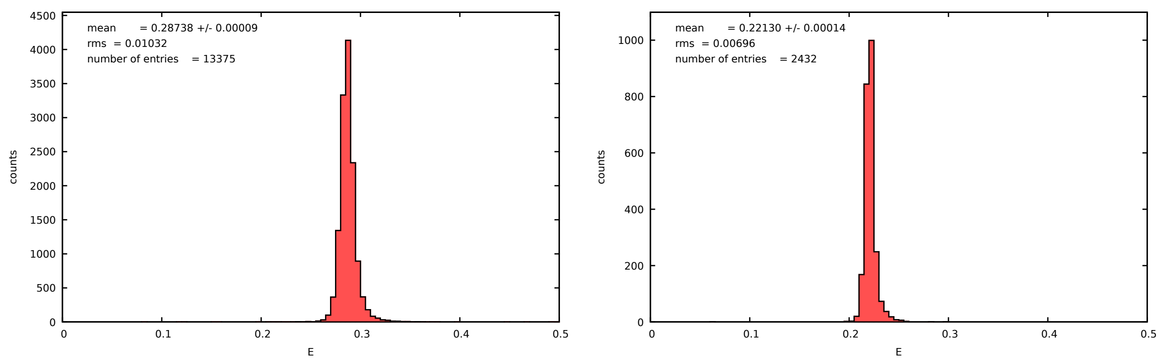

Figure 4.11: Histograms or δE with the beam current 20 µA on the left and 15 µA on the right.

For these three values of δE we perform a linear fit, studying the dependence on the beam current, which is expected to be linear (see figure 4.12).

The c_E conversion parameter is obtained taking the coefficient parameter m from the fit and substituting in the expression:

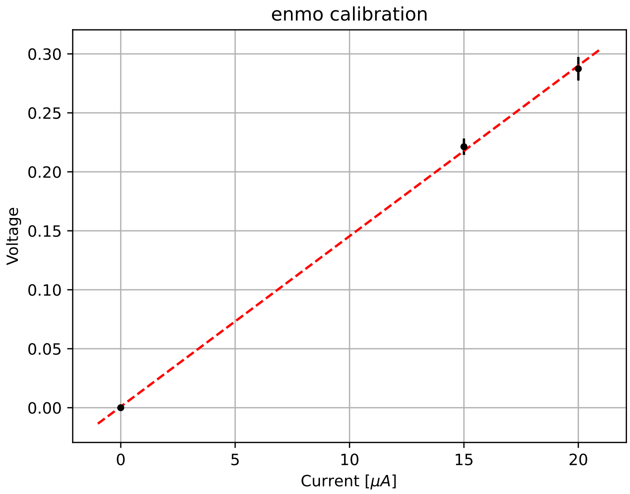

Figure 4.12: Calibration of ENMO monitor, plot of the ENMO voltage values versus the current.

$$C_E = \frac{22.6\,\mathrm{keV}}{m}$$

From this we obtain the value $c_E = +1595.2$ necessary to convert from Voltage units to keV. Using the value, we can show an histogram of δE in physical units, as a check of our procedure (see figure 4.13)

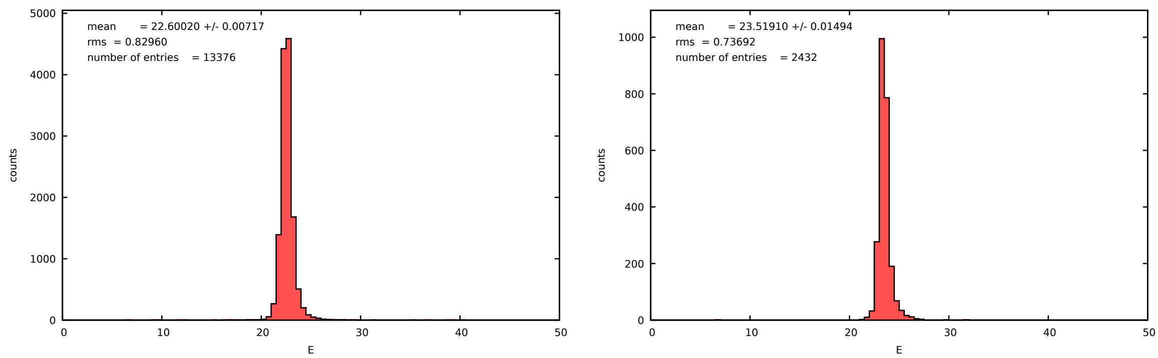

Figure 4.13: Plot for the physical quantities computed in the data tree, for two different current of the beam (on the left 20 µA, 15 µA on the right)

4.3.5 Calibration of the PMTs

Several scans in attenuation of the NINO board were performed on the beam, to choose the best working point for the PMTs of the detectors. The same procedure used in the laboratory was followed: with a beam intensity of 10 µA we acquired data runs one minute long, varying the attenuation.

The PMTs counts in 4.14 are visualized in a different way. It is preferable to visualize the increment of number of signals that pass the threshold selection of NINO board. For this reason, we want to differentiate the data showed in the plots. This procedure consist in computing the difference between the Counts at a certain point and the previous one, and dividing by the increment in attenuation, in equation 4.10.

$$Spectra = \frac{N(att_i) - N(att_{i-1})}{att_i - att_{i-1}} \tag{4.10}$$

In this way we compute a discrete derivative of the plot showed in figure 4.14, which represent $\frac{\partial N}{\partial att}$. This represents the counts increment versus attenuation, see figure 4.15.

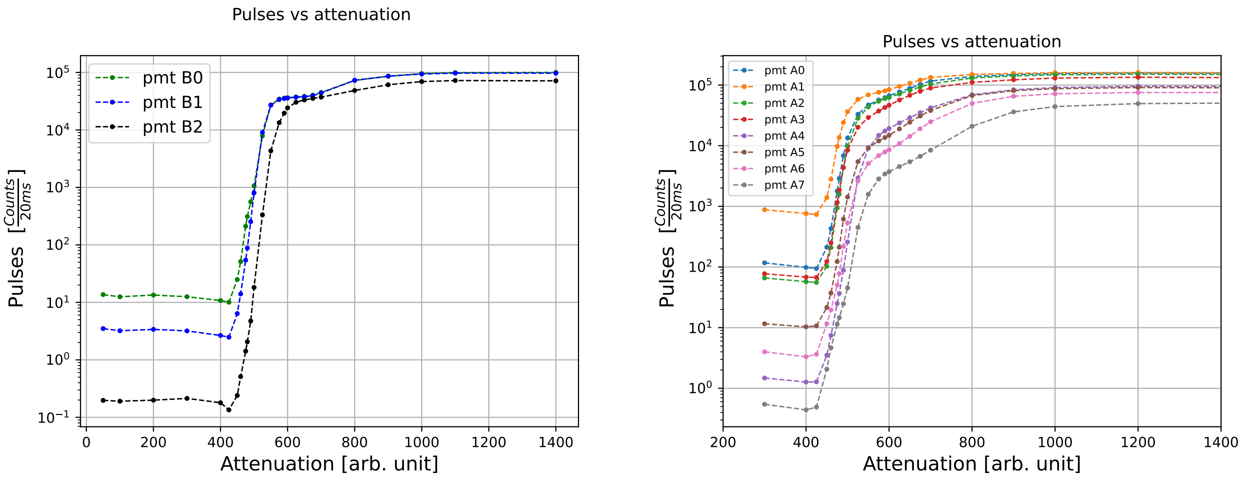

(a) *Attenuation scan for the PMTs of detector B* (b) *Attenuation scan for the PMTs of detector B*

Figure 4.14: Scan in attenuation of the NINO board, with 10 µA. Each point represents the averaged of the counts made on all sub-events of a single data run. Each data run is 1 min long, which correspond to 3000 sub-events.

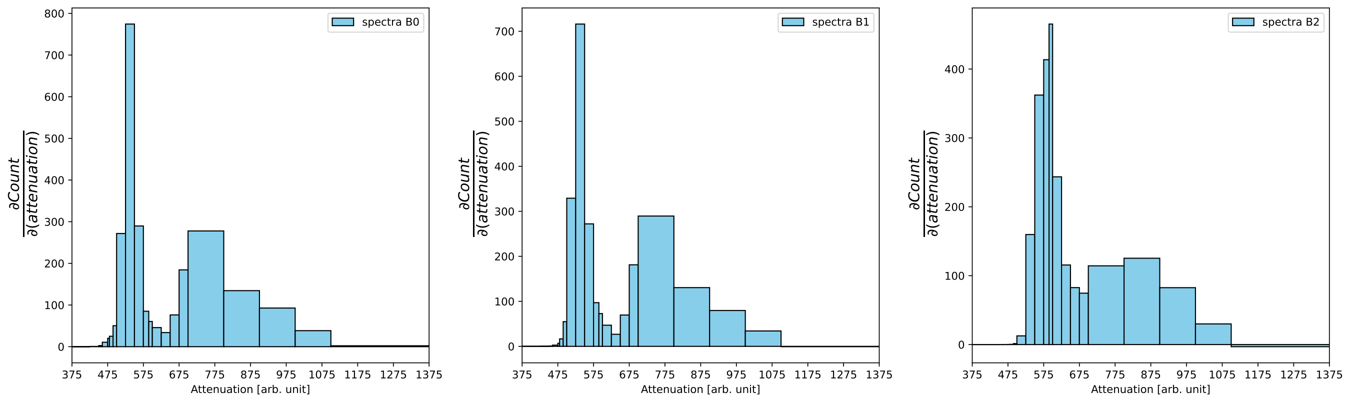

(a) *B0* (b) *B1* (c) *B2*

Figure 4.15: Reconstructed spectra for Detector B

These plots are used to identify a good point to select the attenuation values. If we look at the plots 4.1, we can see that the physical threshold does not scale linearly with changing the *Att* value, and for high values of *Att*, the threshold falls quickly at zero. Looking at the signal spectra, we identify the first peak as the electron signal. The other peak (on the right), correspond to very low threshold values, and it is identified as background noise. We selected the values of the attenuation between the peaks of the two distributions, maximizing the signal acceptance and trying to reject the background as much as possible. Our discussion so far is sufficient to carry out the calibration of the PMTs and take data to measure the asymmetry. However, we would like to identify the physical threshold in mV instead of attenuation unit. We can use the conversion function that we discussed in figure 4.1:

$$f(att) = \frac{a}{(x-b)^3 + d}$$

We point out that the parameters of this function have been obtained from data that have not been acquired during this thesis work, moreover the threshold value in the program that controls the NINO board is slightly different (we always used 600, the data are taken with 750), therefore the values in volts need probably to be rescaled by some factor, but for our discussion we are interested in a raw estimation of the signal peak: With this conversion, we show the same plots in 4.15, with the values in the x-axis in V now.

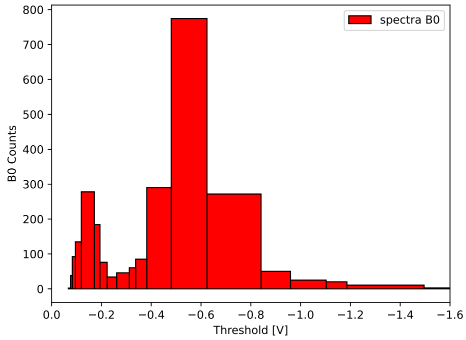

(a)

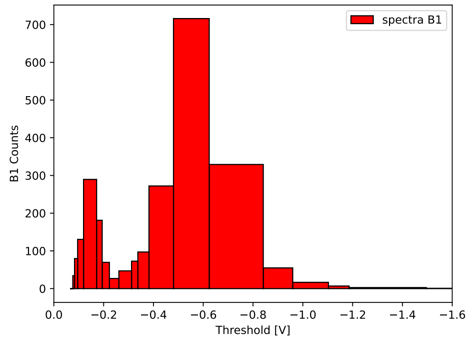

(b)

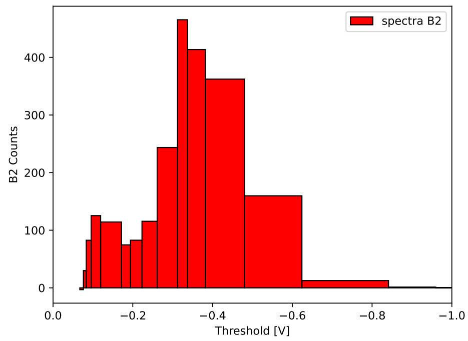

(c)

We know see clearly two peaks, the signal and the background, that are reversed respect to figure 4.15. We discuss now a simple model that we used to describe how the PMT Counts vary when we raise the attenuation. From the plot 4.15, we assume that the two peaks are described by two gaussian distributions. Now if we think about the the probability for a signal to pass the selection, this quantity is equal to the probability of being in below the attenuation value. Using now the fact that the probability are given by the cumulative of the gaussian distribution (probability of being in the right tail) it is straightforward to deduce:

$$P(signal > thr) = \Phi(x) = \frac{1 + Erf(\frac{x-\mu}{\sqrt{2}\sigma})}{2}$$

Considering that we have the sum of two gaussian distribution, we end with:

$$N(att) = \frac{n_1 + n_2}{2} + (\frac{n_1}{2})Erf(\frac{x-\mu_1}{\sqrt{2}\sigma_1}) + (\frac{n_2}{2})Erf(\frac{x-\mu_2}{\sqrt{2}\sigma_2}) \tag{4.11}$$

This model is used to fit the data shown in figure 4.14. The result is shown in figure **??**, the parameters obtained from the fit are reported below:

PMT	μ_1	σ_1	μ_2	σ_2	n1	n2
B0	538.0 +/- 1.3	19.4 +/- 1.1	798 +/- 8	103 +/- 4	34277 +/- 662	64244 +/- 1538
B1	536.4 +/- 0.9	18.2 +/- 0.7	783 +/- 5	89 +/- 2	34053 +/- 475	61636 +/- 1109
B2	582.8 +/- 1.2	25.9 +/- 1.0	824 +/- 8	88 +/- 6	32880 +/- 758	37930 +/- 1245

Table 4.10: Best fit result for the model defined in equation 4.11

From these result we measure the mean μ_1 and μ_2 for the signal and the background given in attenuation units. The correct value of attenuation is set between the two observed peaks, in order

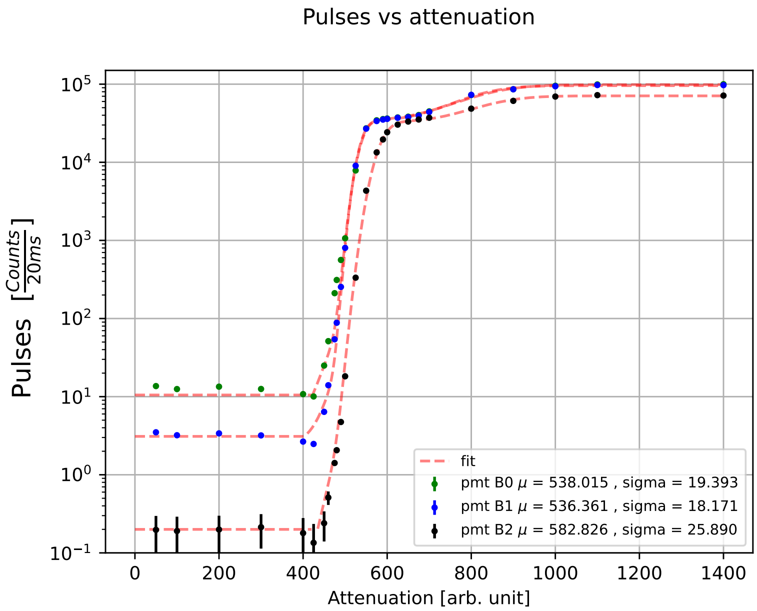

Figure 4.16: Best fit for the data of counts versus attenuation, for detector B.

to rejects the background and take only the signal coming from the scattered electrons. The same procedure was followed also for the detector A, the plots are not reported, for brevity.

With these procedure, the *Att* value has been selected. The values are reported in table 4.11

PMT $n°$	B0	B1	B2	A0	A1	A2	A3	A4	A5	A6	A7
Att	600	600	625	600	590	600	600	600	590	600	600

Table 4.11: Attenuation settings for both the detectors.

4.3.6 Auto-calibration Procedure

In this section we present the last calibration technique needed in the data-process. The auto-calibration is a special operation mode of the MAMI accelerator, during which the beam current is made to vary in a controlled way. Through these special runs is possible to obtain again the current scaling factor that we discussed in section 4.3.3 and it is possible to study the linearity of the PMTs. From a linear fit of the PMTs counts vs. current intensity the angular coefficient and the offset are measured. The offset is particular important because give rise of a possible systematic error that influence the final asymmetry result. It is simple to demonstrate this, if a relation of the type $N = mI + N_0$ holds. Consider the following quantity:

$$\overline{N} = \frac{N_\uparrow + N_\downarrow}{2}$$

we can express $N_\uparrow$ and $N_\downarrow$ in this way using the asymmetry $A_n = \frac{N_\uparrow - N_\downarrow}{N_\uparrow + N_\downarrow}$:

$$N_\uparrow = \overline{N} + A_n\overline{N}$$
$$N_\downarrow = \overline{N} - A_n\overline{N}$$

Now we suppose that $\overline{N}$ is linear dependent on the current in the way we defined above, so:

$$N_\uparrow = mI + N_0 + A_n(mI)$$
$$N_\downarrow = mI + N_0 - A_n(mI)$$

We are supposing that the offset N_0, we assume that the present offset does not contribute to the asymmetry, i.e. it is not correlated to the signal of the scattered electrons, but is due to processes of another type, therefore in the previous formulas only the mI counts must be multiplied by the asymmetry A_n. Therefore if we substitute everything in the definition of the transverse asymmetry:

$$A' = \frac{N_\uparrow - N\downarrow}{N_\uparrow + N\downarrow} = \frac{A_n(2mI)}{(2mI) + 2N_0} = A_n \frac{1}{1 + \frac{N_0}{mI}} = A_n \cdot c \tag{4.12}$$

In the last passage we learn that the presence of an offset can decrease the reconstructed asymmetry. So it is important to determine quantitatively N_0 and m in order to be able to correct for this effect. The strategy used is quite simple: every three hours of production data, we asked MAMI to start the auto-calibration program. With all the auto-calibration runs, we estimate N_0 for each PMT, separately. Then All this quantities are saved in a file so that the analysis program can retrieve the parameters and subtract them from the PMT counts. In this way every three hours the PMT are corrected, taking care also of the possibility that the the linearity of the PMTs can change after hours of use of the PMTs (for example it can decrease the efficiency). During the auto-calibration, the beam current is raised from 9 µA to 11.125 µA in step of 0.125 µA:

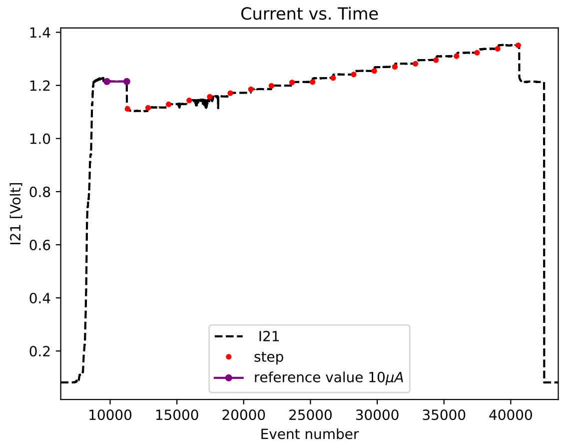

Figure 4.17: Auto-calibration: in this plot we have the voltage value of I21 monitor. The current is first stabilized around 10 µA, then it is raised from 9 µA (the step lower down) to 11.125 µA in step of 0.125 µA.

With a linear fit we can estimate the scale and the offset to convert from I21 voltage values to physical values of the current. The procedure in repeated for the 8 auto-calibration acquisition we had during the beam time, so we can also take care of possible variations during the time.

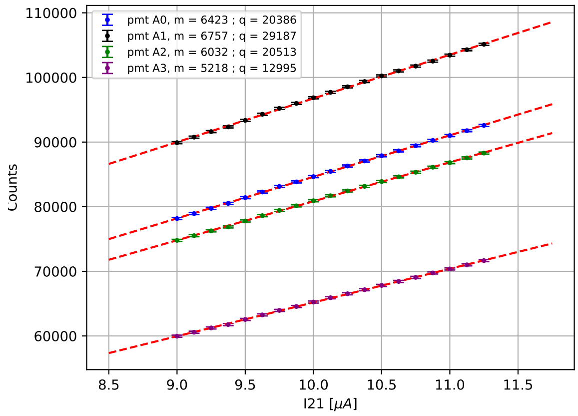

(a) *Current scan for detector A, the error are multiplied by a factor of* 20.

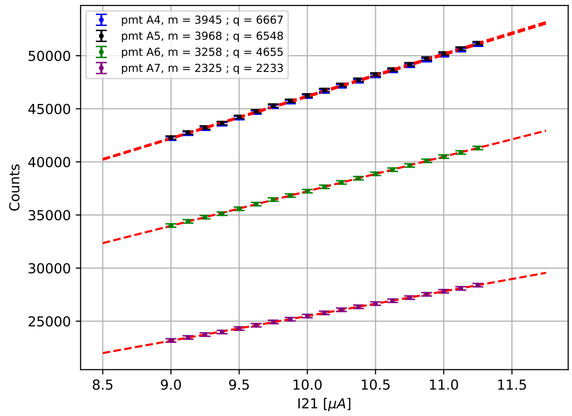

(b) *Current scan for detector A, the error are multiplied by a factor of* 20.

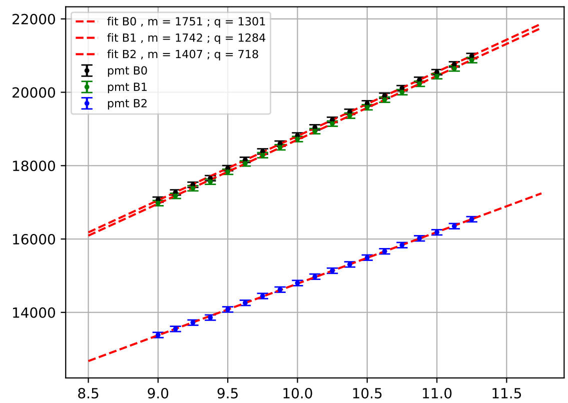

(c) *Current scan for detector B, the error are multiplied by a factor of* 20.

The figures are referred to the data acquired for the first auto-calibration. We report the values of slope and offset measured during the first auto-calibration run. These data are valuable because we can compute the decreasing factor c that appears in equation 4.12:

Ignoring the presence of the offset lead two consequences: the reconstructed asymmetry is lower, on average $\simeq 10\%$ less than expected, and the Counts are overestimated. Because the error depend on the PMT counts, as seen in equation 2.14, this two effect combined add up and decrease the accuracy of the asymmetry measurement The value c reported in the caption 6 can be compared with c in table 6, computed as the ratio between $\frac{A_{notcorr.}}{A_{corr}}$, where $A_{notcorr.}$ stands for the asymmetry result not corrected for the offset and A_{corr} are the result with offset corrected.

4.4 Data Tree Implementation

Referring to figure 3.1, we now discuss briefly the structure of the data that is implemented in the analysis program, important to clarify how data analysis will be developed. The base class that is implemented in the analysis program is the *Event* class. As we mention above in section 3.1, we do not intend to keep track of the single scattered electron, instead we analyze time series of 80 ms, in which we simply count all the electrons detected in this time interval. The work-flow of the analysis program is load the binary file collected during the beam time, parsing one event at a time and processing the raw-data from the beam monitors and the detectors. During the execution of the program data files in *.txt* are generated and filled with the processed data ready. The output data-file can be analyzed with any software package, such as root or python, to get the value of the asymmetry A_n. The picture

PMT	m [µA^{-1}]	Offset	c
B0	1750	1301	0.930 ± 0.003
B1	1742	1283	0.931 ± 0.003
B2	1406	717	0.951 ± 0.003
A0	6423	20385	0.759 ± 0.002
A1	6756	29187	0.698 ± 0.003
A2	6032	20513	0.746 ± 0.002
A3	5218	12995	0.800 ± 0.002
A4	3945	6666	0.855 ± 0.002
A5	3967	6547	0.858 ± 0.002
A6	3258	4655	0.874 ± 0.002
A7	2325	2233	0.912 ± 0.002

Table 4.12: Angular coefficient and offset obtained for the auto-calibration. The third column is contains the estimation of c, as defined in equation 4.12

shows that every event is divided into 4 sub-events. For each different sub-event a precise state of the polarization is defined, +1 for $S = \uparrow$ and −1 for $S = \downarrow$. Every sub-event is 20 ms long; during this time interval master-board receives all the data coming from the monitors and the detectors and sent them to the data-acquisition program (DAQ) that produces the binary-files, which are the input of the main analy sis program.

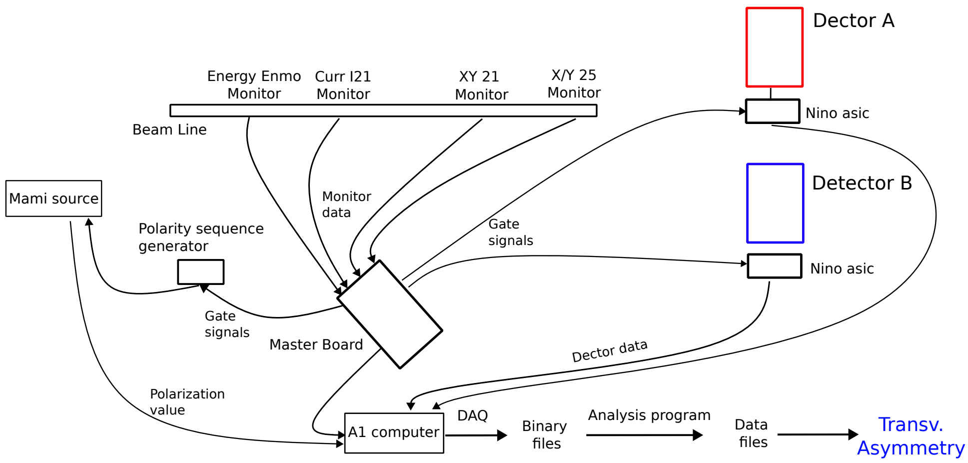

Figure 4.18: Scheme of the data flow.

It is important to note that for each sub-event, a single measurement is acquired from the beam monitors, which is intended as a time average of the various signals on the 20 milliseconds of sub-event duration. The sampling rate is then equal to 50 Hz. This structure of the data is quite specific. The main reason for this setup is connected with the need to avoid as much as possible that the variations of intensity, position and energy of the beams induce an effect that add to A_n. Considering only small time series, it is assumed that the beam is quite stable, in order to reduce undesired effects. Nevertheless, the contribution of these effects, which are indicated for brevity as false asymmetries, is considered in the final model. Several values are saved with the number of scattered electrons, for each event. The general structure of the data tree, with the important quantities, is reported here figure 4.19

The analysis program read the binaries files, convert from binary to decimal values and compute the beam parameters from the raw data of the monitors, filling the data tree shown in the figure. We have 5 different classes, that are contained in the main *Event* class. The asymmetry values are stored in the two separated classes, *Det A* and *Det B*. The Analysis program read and analyze one event at a time, can produce also histograms for a fast visualization of the data, and generates the final output files in *txt* format for the data analysis.

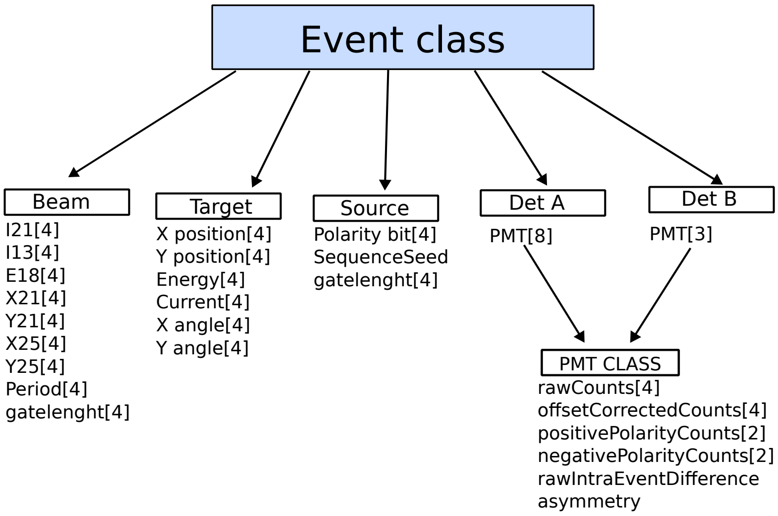

Figure 4.19: Scheme of the Event class, the structure of the data tree is explained in the appendix.

Chapter 5

Asymmetry on Carbon and Rates on Lead Target.

After having described all the calibrations needed, we are ready to analyze the data and measure the transverse asymmetry from the data collected in the second part of the beam time. In this chapter we explain the procedure for the pre-selection of the data (for example the removal of the events with large variation of the beam parameters) and the procedure used to analyze the asymmetry of the two detectors to obtain, in the end, a single estimation of A_n. A section is dedicated to the measurement performed with lead target; through the knowledge of the expected counts per sub-event, we compute the amount of statistics needed to measure the transverse asymmetry on Pb with an accuracy of $\simeq 1/$ *ppm*. In the end we discuss the problem of the false asymmetries that can affect the final result, using different method to calculate their contribution. The amount of data that are available corresponds to 23 hours of acquisitions, that are roughly 1 million of events.

5.1 Model for Fitting the Data

One of the problems of the measurement is to take into consideration the various contributions that can change the value of the asymmetry measured by the experimental apparatus. The raw values of the asymmetry can be affected by the variation of the beam parameters during the time. Let's summarize quickly these effects:

- the PMTs counts can depend on the (x, y) impact position of the beam on the target
- the variations of the incident angles $\theta_x$and θ_y on the target.
- the uncertainty associated with the energy of the beam, a change in the energy associated with the polarization of the beam leads to different rates for the cross section.
- the uncertainty associated with the current of the beam, in particular a difference in the efficiency of the source in producing electrons polarized in the two opposite directions.

All this quantity, which we will indicate in general with δq can influence the asymmetry measurement, considering also that the expected asymmetry is in the order of ten part per million, and small asymmetry introduced by fluctuations on the beam parameters are not negligible. Correcting directly the false asymmetries that arise from those uncertainties is a tough task, and it is easier to adopt a different strategy rather than the analytical/numerical calculation of each of them. Knowing that the beam parameters produced by MAMI are quite stable over the time, we can assume that the measured asymmetry are well described by a linear model as the following:

$$A_{tot} = A_{physical} \cdot P + \delta_I + A_x\delta x + A_y\delta y + A_{\theta_x}\delta\theta_x + A_{\theta_y}\delta\theta_y + A_E\delta E \tag{5.1}$$

$A_{physical}$ is the aim of the experiment, A_x and A_y are the coefficients induced by the variation of the position of the beam, A_{θ_x} and A_{θ_y} are the coefficients associated to angles, A_E is the coefficients associated to the beam energy and P is the polarization percentage. This is a first order approximation, which is valid for small variation of the beam parameters ($\delta x, \delta y, \delta\theta_x, \delta\theta_y, \delta_E$). We must clarify now what we mean with $\delta x, \delta y, \delta\theta_x, \delta\theta_y, delta_E$. Recalling the event structure, that we discussed in section 3.1, we have a sequence of 4 different sub-events, with a polarization pattern that is randomly selected between $\uparrow, \downarrow, \downarrow, \uparrow$ and $\downarrow, \uparrow, \uparrow, \downarrow$. During the 20 ms of time length of each sub-event, the beam monitors make a single measurement of the beam parameters, and the data are saved in the data tree. The task of the analysis program is to use this raw data to calculate the relevant parameters for the analysis. Because we are working with asymmetries, the absolute values of the parameters listed above is not relevant, instead what is relevant are the differences between different polarization states of the beam. Assuming this, $\delta x, \delta y, \delta\theta_x, \delta\theta_y, \delta_E$ are defined by equation 5.2:

$$
\begin{aligned}
\delta x &= \Big(\frac{x_\uparrow(1) + x_\uparrow(2)}{2}\Big) - \Big(\frac{x_\downarrow(1) + x_\downarrow(2)}{2}\Big)\\
\delta y &= \Big(\frac{y_\uparrow(1) + y_\uparrow(2)}{2}\Big) - \Big(\frac{y_\downarrow(1) + y_\downarrow(2)}{2}\Big)\\
\delta E &= \Big(\frac{E_\uparrow(1) + E_\uparrow(2)}{2}\Big) - \Big(\frac{E_\downarrow(1) + E_\downarrow(2)}{2}\Big)\\
\delta\theta_x &= \Big(\frac{\theta_{x,\uparrow}(1) + \theta_{x,\uparrow}(2)}{2}\Big) - \Big(\frac{\theta_{x,\downarrow}(1) + \theta_{x,\downarrow}(2)}{2}\Big)\\
\delta\theta_y &= \Big(\frac{\theta_{y,\uparrow}(1) + \theta_{y,\uparrow}(2)}{2}\Big) - \Big(\frac{\theta_{y,\downarrow}(1) + \theta_{y,\downarrow}(2)}{2}\Big)\\
\delta I &= \frac{I_\uparrow - I_\downarrow}{I_\uparrow + I_\downarrow}
\end{aligned}
\tag{5.2}
$$

Each δq represents the variation of one of the parameters of the beam within an event, so. One may wonder why the model doesn't contain a parameter A_I to describe the false asymmetry due to the current. We can show theoretically that the values of A_I is equal to 1. Starting from the definition of rate Γ:

$$
\Gamma = \frac{dN}{dt} = \frac{I_0}{e}\,\sigma\,\frac{n_t V_t}{S} \tag{5.3}
$$

where I_0 is the beam current, e is the elementary charge, n_t is the number density of the target, V_t the target volume and S is the surface of the beam. Using 5.3, the total asymmetry A is given by the equation 5.4.

$$
A = \frac{\frac{dN_\uparrow}{dt} - \frac{dN_\downarrow}{dt}}{\frac{dN_\uparrow}{dt} + \frac{dN_\downarrow}{dt}} = \frac{\sigma_\uparrow I_{0\uparrow} - \sigma_\downarrow I_{0\downarrow}}{\sigma_\uparrow I_{0\uparrow} + \sigma_\downarrow I_{0\downarrow}} \tag{5.4}
$$

Let's suppose now that the false asymmetry associated to the current is given by $A = A_I \cdot \delta I$. Now, the formula in the model is slightly different

$$
A = \frac{\sigma_\uparrow - \sigma_\downarrow}{\sigma_\uparrow + \sigma_\downarrow} + \frac{I_\uparrow - I_\downarrow}{I_\uparrow + I_\downarrow} = \frac{2(\sigma_\uparrow I_{0\uparrow} - \sigma_\downarrow I_{0\downarrow})}{2\sigma_\uparrow I_{0\uparrow} + 2\sigma_\downarrow I_{0\downarrow} + \sigma_\uparrow I_{0\downarrow} + \sigma_\downarrow I_{0\uparrow}} \tag{5.5}
$$

Now, the asymmetry in the cross section in expected to be of the order of 10^{-6}. If we approximate $\sigma_\uparrow \simeq \sigma_\downarrow$, the two formula above are equal. In the end we have the equation 5.6.

$$
A_{tot} = A_n + \frac{I_{0\uparrow} - I_{0\downarrow}}{I_{0\uparrow} + I_{0\downarrow}} = A_n + \delta_I \tag{5.6}
$$

This is a direct consequence of the fact that the luminosity is proportional to the beam current, so we don't need to add a new parameter to the model.

5.2 Data Pre-selection and Fit

After all the calibration are performed, the analysis program is ready to produce the data-files suitable to analyze the asymmetry data for Carbon. Before proceeding with the linear fit, however, it is necessary to visualize the data to check that there are no anomalous behaviors. In fact the data can contain moments of loss of the beam current and sudden interruptions, loss of the beam polarization and even setting errors by MAMI operators can affect the experiment. Carbon data were taken from November 2nd to 4th, and consist of 28 runs, each 1 hour long. The first step is to observe the PMT counts and the current trend, in order to be able to identify sudden interruptions of the beam, outliers and to check the behaviour. Here we show the trend over time for the series runs:

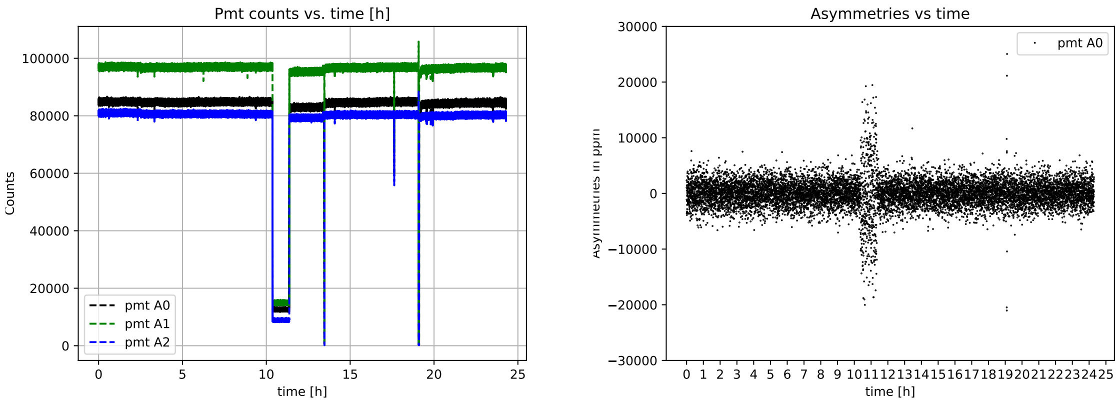

(a) *Counts vs. time* (b) *Asymmetry trend for PMT A0*

Figure 5.1: On the left, counts versus time for all the runs acquired during the beam time. On the right the measured asymmetry versus time. The conversion from event number to time is made knowing that each event correspond to 80 ms. A total of 22 hours of beam was collected.

This plot show that after 10 h of data acquisition the PMT counts (see plot 5.1) dropped rapidly. In the current vs time (figure 5.2a) there is not a corresponding decrease in beam intensity. Also the x, y position (5.2b) and the energy monitor of the beam do not show unexpected behavior, so we reject the possibility that the beam was not properly aligned to the target. For all the PMTs of this suspecious data run, the counts are equal to the offsets measured with the auto-calibration run. This indicates that there was a failure in the data acquisition program, which controls the NINO board. These data are rejected completely from the analysis. In plot 5.1 and 5.2a we observe abrupt variations of the asymmetry at $13.5h$ and $19h$, while other variations are less appreciable. These data correspond to loss of the beam intensity for a short periods of time, and are rejected as outliers.

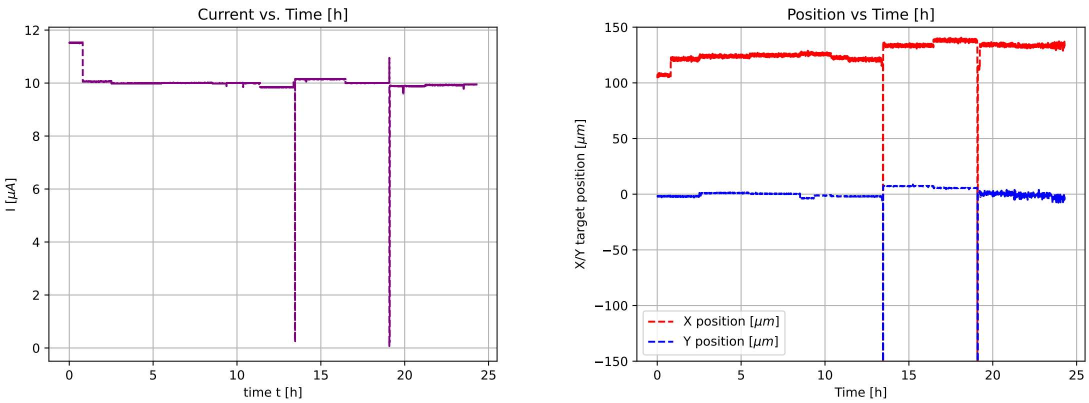

(a) *Current trend over time.* (b) *X, Y beam position over time*

Now we focus our attention on the correlated-difference values. These quantities, are used as independent variables for the fit, as explained before, are defined as

$$\delta x = \frac{(X_{up,1} + X_{up,2})}{2} - \frac{(X_{down,1} + X_{down,2})}{2}$$

and are calculated within each single event, to identify the differences with respect to the various quantities such as position, energy, etc., which correspond to different states of polarization. For every of these quantities a correspondent histogram is shown in figure 5.2. These plots are useful to quantify the stability of the beam: we expect that all the correlated differences are distributed around zero, which implies that there is no systematic difference when the beam has one polarization state respect to the other. The mean μ and the standard deviation σ of the distributions are reported in the table (5.1)

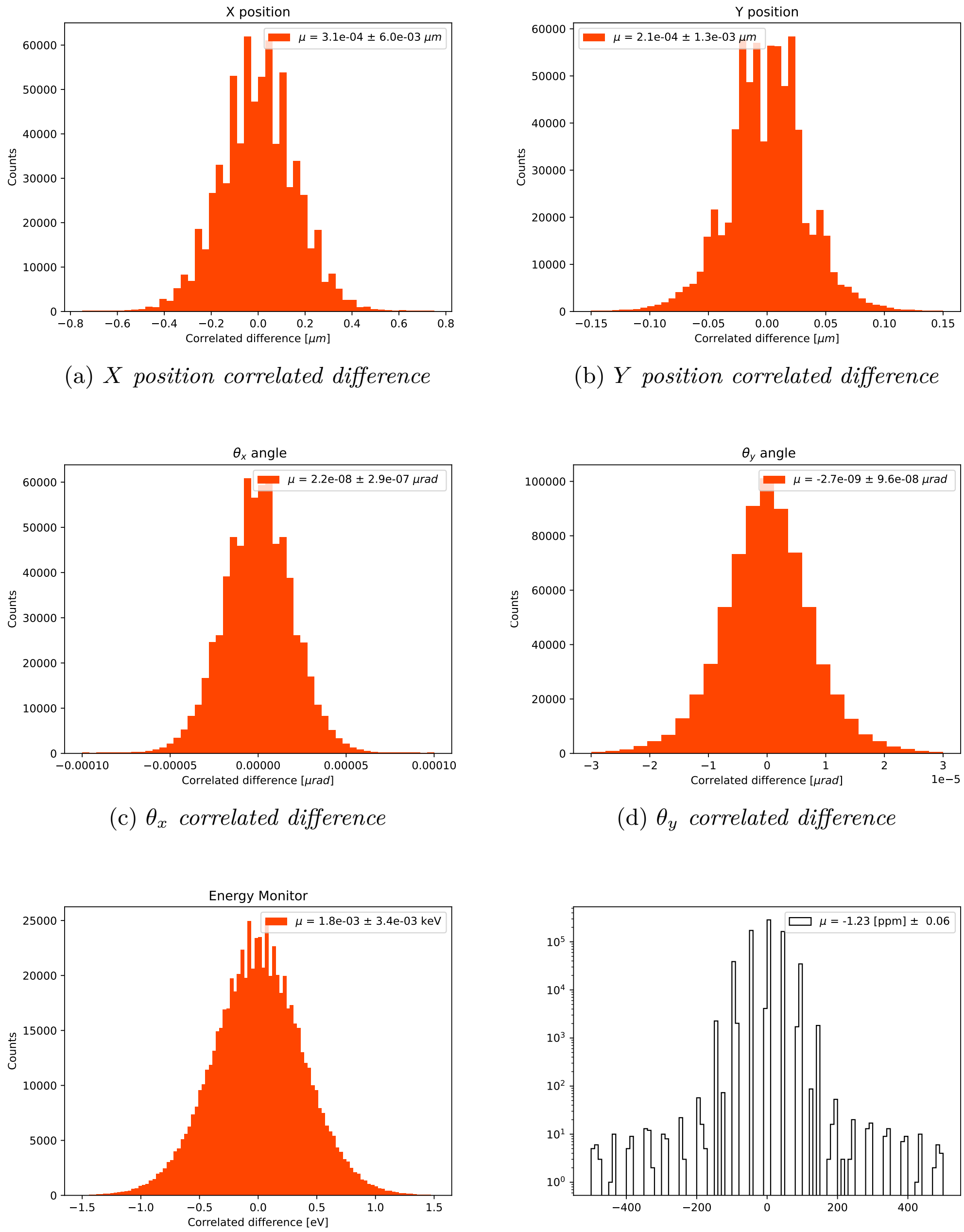

(a) *X position correlated difference*

(b) *Y position correlated difference*

(c) θ_x *correlated difference*

(d) θ_y *correlated difference*

(e) *Energy correlated difference*

(f) *Current asymmetry*

Figure 5.2: Histogram for the beam parameters.

Every histogram is generated with 100 bins. For the current asymmetry, we discovered that the values of the VFCs resistance which controls V_{ref} value was set too high. Because of this, the precision of the monitor is low, compared to the other, and we observe isolated peaks in the plot. This indicated that for the incoming experiment we have to increase V_{ref} in order to to have a precision comparable to that of other monitors.

Table 5.1: Beam parameters:

Beam Parameters	$X[\mu m]$	$Y[\mu m]$	$\theta_x[\mu rad]$	$\theta_y[\mu rad]$	$E[eV]$	$I[ppm]$
μ	$1.31 \cdot 10^{-3}$	$2.4 \cdot 10^{-4}$	$3.2 \cdot 10^{-8}$	$3.6 \cdot 10^{-9}$	0.0013	-1.23
$sigma$	$3.7 \cdot 10^{-1}$	$2.9 \cdot 10^{-2}$	$1.9 \cdot 10^{-5}$	$6.5 \cdot 10^{-6}$	0.38	50.4

Looking at the values of the mean and the corresponding error σ reported in the plots legend, we observe that the means of $X, Y, \theta_x, \theta_y, E$ are compatible with 0. These results are encouraging: we are not able to identify a systematic difference between polarization $+1$ and -1. A systematic difference would have produced a value μ shifted from zero, and a corresponding effect on A_n. With our assumption that the false asymmetries are well described by a linear model, observing that μ is small and compatible with zero for all the parameters, together with the evidence that δq are distributed symmetrical around zero, leads to the cancellation of all the false asymmetries, as can be seen in equation 5.7 :

$$\overline{A} = A_n \cdot P + \overline{\delta_I} + \overline{\delta_x} A_x + \overline{\delta_y} A_y + \overline{\delta_{\theta_x}} A_{\theta_x} + \overline{\delta_{\theta_y}} A_{\theta_y} + \overline{\delta_E} A_E = \tag{5.7}$$

$$A_n \cdot P + \overline{\delta_I} + A_x \cdot 0 + A_y \cdot 0 + A_{\theta_x} \cdot 0 + A_{\theta_y} \cdot 0 + A_E \cdot 0 = A_n \cdot P + \overline{\delta_I} \tag{5.8}$$

We will discuss later, when we will introduce the fit results, whether our assumption reflects the reality. We assume that the only false asymmetry that has an effect is δI: $\overline{\delta I}$ is equal $-1.23\,ppm$, and we will subtract that to the final result:

$$A_n = \overline{A_{tot}} - \overline{\delta I}$$

5.3 Polarization Loss

After discussing the removal of the outliers, now will discuss in details the issue regarding the polarization of the beam. To observe a transverse asymmetry , it is essential to have a correctly polarized beam. Unfortunately, we found out that by mistake part of the data where acquired with a beam made by non-polarized electrons. The reason is that during the second night of the experiment, MAMI operators who controls the quality of the beam switched from polarized beam to non-polarized, unintentionally. These wrong data were acquired during the night of 2nd December and we discovered this problem only the next day. We had no indication of how many hours of beam were lost. Because this happened during the night, nobody could save the polarization measurement of the beam and identify the runs affected by this problem. This issue introduces a big systematic error that is potentially decreases the reconstructed A_n. It is important to identify the runs that share this problem, otherwise the measurements are affected by a bias that is not possible to disentangle from other systematic effects related to the electronics system of the experiment. All the stabilization monitors were active and the data show apparently the same behaviour of the data with the correct polarization. We can not proceed with an arbitrary cut of the data, because there is the risk to cut off also good data or perform an incomplete removal. The next phase of the analysis is focused on describing a method used to identify the data taken with unpolarized beam and remove them from the analysis.

The procedure to identify the runs without polarization rely on the estimation of the correlation coefficient of the PMTs counts. For every event we have two type of polarization sequence. The polarization P of each sub-event is identified with $+1$ and -1, that correspond to up and down P.

This values are part of the data tree, and form a sequence p_i of the type: $+1 - 1 - 1 + 1$, where i is the index to the i-th sub-events analyzed . If the P is different from zero, we expect, caused by the transverse asymmetry, a difference in the number of scattered electrons between sub-events with different p_i (see table 5.2).

sub-event	1	2	3	4	5	6	7	8
Polarity	+1	-1	-1	+1	+1	-1	-1	+1
PMT B0	101	99	98	102	100	99	97	103
Other PMT	...	...	...	...	...	...	...	...

Table 5.2: Example of the Polarity sequence and PMT counts that are saved in the analysis program. The values of the PMT counts given are for example.

This leads to a positive/negative correlation between the sequence p_i and the PMT data. In case of $\vec{P} = 0$, the expected values for the correlation should be zero. We applied this strategy with the hope to identify the blocks of data with $P = 0$, also using the knowledge that the polarization was turned off at some point during the night. The correlation c between p_i and the PMT sequence N_i of counts is measured every $t = 1h$, corresponding to 45000 events. We plot the averaged correlation for detector A and B, and the correlation of the two detectors together (with the reverse sign for detector B) in figure 5.3.

The correlations coefficient c is clearly dependent on the $\vec{P}$. is we observe that c is compatible with zero, we have an evidence of the block of runs to be removed from the analysis. The values are reported in figure 5.3. The errors for each point are computed with the formula:

$$\sigma_c = \sqrt{\frac{1 - c^2}{N - 2}}$$

The plots show also the expected values for the c computed with a simple simulation, using the values of $A_n = 22.5ppm$ and $P = 0.79$ as an input. The simulation results are obtained following these steps:

- A sequence of the type $+1, -1, -1, +1$ is generated, long 45000 events.
- For each sub-event of the previous sequence, the PMT counts are generated: the counts are sampled from a gaussian distribution with μ and σ^2 equal to the values measured for both the detectors. To reproduce the correlation with the polarity sequence, the values are shifted accordingly by a factor $\mu \cdot A_n \cdot P$
- The previous step is repeated 25 times, and for each iteration we compute and save the correlation between the polarity sequences and the counts.
- From the values saved, we compute the mean c (the dotted line in plot 5.3) and σ_c.

Looking at the plots, we observe for detector A a block of runs where c is compatible with 0, in contrast with the values expected from the simulation. Due to the higher error, the corresponding plot for detector B is not clear to interpret, however the plot on the right with the overall results for A and B confirms the evidence for A. This let us to identify the block of runs that show a behaviour compatible with $P = 0$. it is important to check that validity of this method seeing if the corresponding asymmetry is compatible with 0 (see figure 5.4).

The asymmetry values for this block of runs show an unexpected behaviour. For both detectors we observe negative values. The weighted mean for the two detector is :

- $A_B = -7 \pm 5$ ppm
- $A_A = -5 \pm 2$ ppm

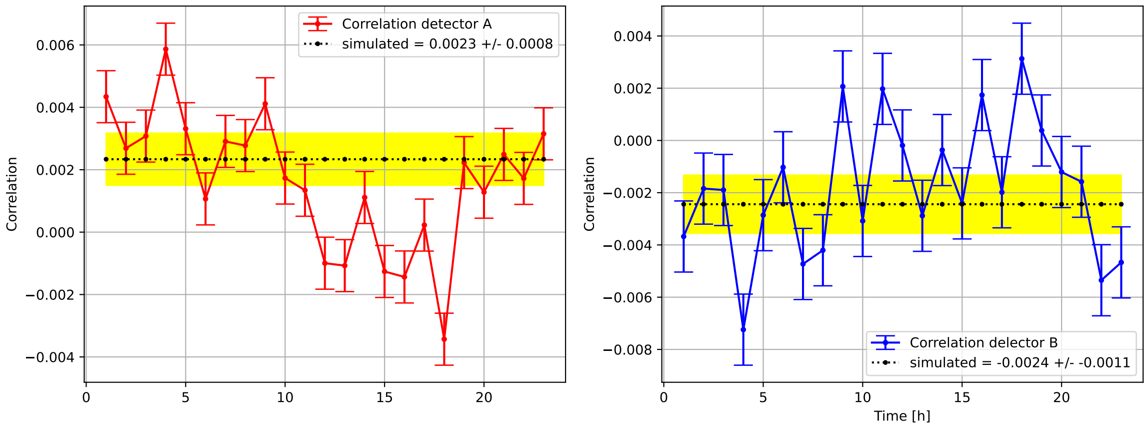

(a)

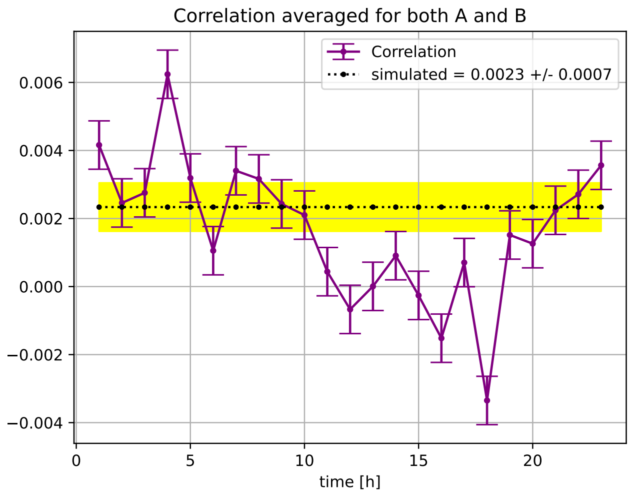

(b)

Figure 5.3: Correlation between the polarization sequence and the asymmetry. The plot *a* shows the averaged value for detector A and B, respectively. The plot *b* shows the overall result for the two detector combined, reversing the sign of the asymmetries of detector B. In yellow the error band expected, computed with a montecarlo simulation.

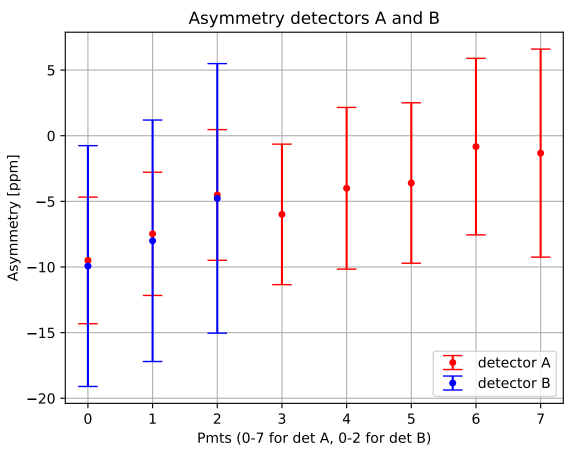

Figure 5.4: Raw-asymmetry computed for the block of runs with $P = 0$. Except for one PMT of detector A, all the values are compatible with 0 in 1σ.

The values are not compatible with zero, but are compatible with each other. It is therefore reasonably certain that such data should not be included in the main analysis, because we observe a negative asymmetry for both the detectors that is not compatible with the presence of a polarized beam.

5.4 Fit with a Linear Model

At this point, it is interesting to study the distribution of the asymmetries measured by the two detectors. Our main assumption is that the asymmetries values are distributed following a normal distribution, around the physical value A_n. We have produced several histograms for the measurements of every PMT (see figure 5.5,5.6 and 5.7). The data without polarization are not included in the histograms. For every histogram we use a gaussian function to fit the data, the reduced χ^2 is reported in the table 5.3. We see a good agreement with the hypothesis of normal distributed data.

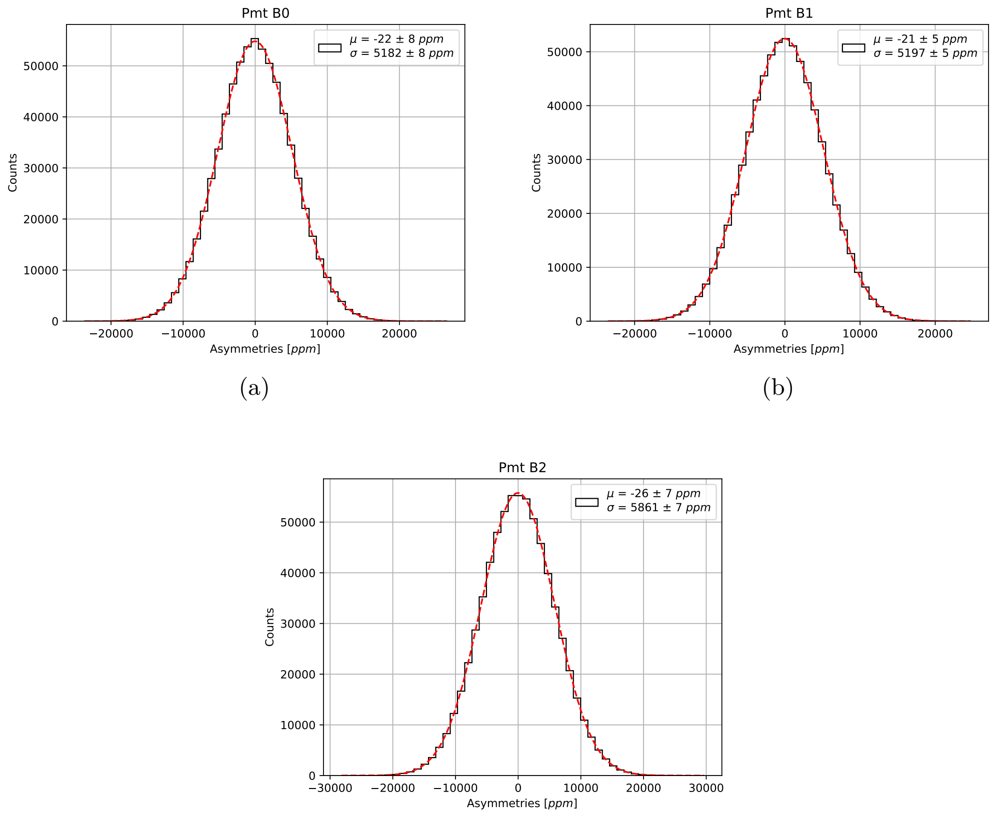

(a) (b) (c)

Figure 5.5: Histogram of the Asymmetry for Detector B. The Asymmetries are corrected removing the data without polarization. The raw asymmetries are multiplied by $\frac{1}{P}$

Recalling the equation 2.14, where we assumed that A a normal distributed variable, now we can confirm our initial assumption. To extract the asymmetry A_n from the data, we assume a linear model where the asymmetries depend on the beam parameters, in the way we discussed in section 5.1. The contributions due to variations of the beam within an events are described with 5 parameters, that are $A_x, A_y, A_{\theta_x}, A_{\theta_y}, A_E$. The data are analyzed both using python libraries, and with a fit program implemented in the framework of this thesis. To analyze the data with python, it is used the *curvefit* function implemented in the python library *scipy*. We also implemented a dedicated program to interface directly to the analysis program, the fit program, that is written in *C++* code. The fit program implements the ordinary least square algorithm (OLS), a well know algorithm used in linear regression. The OLS algorithm is basic algorithm, easy to implement and robust. In linear regression it is assumed that :

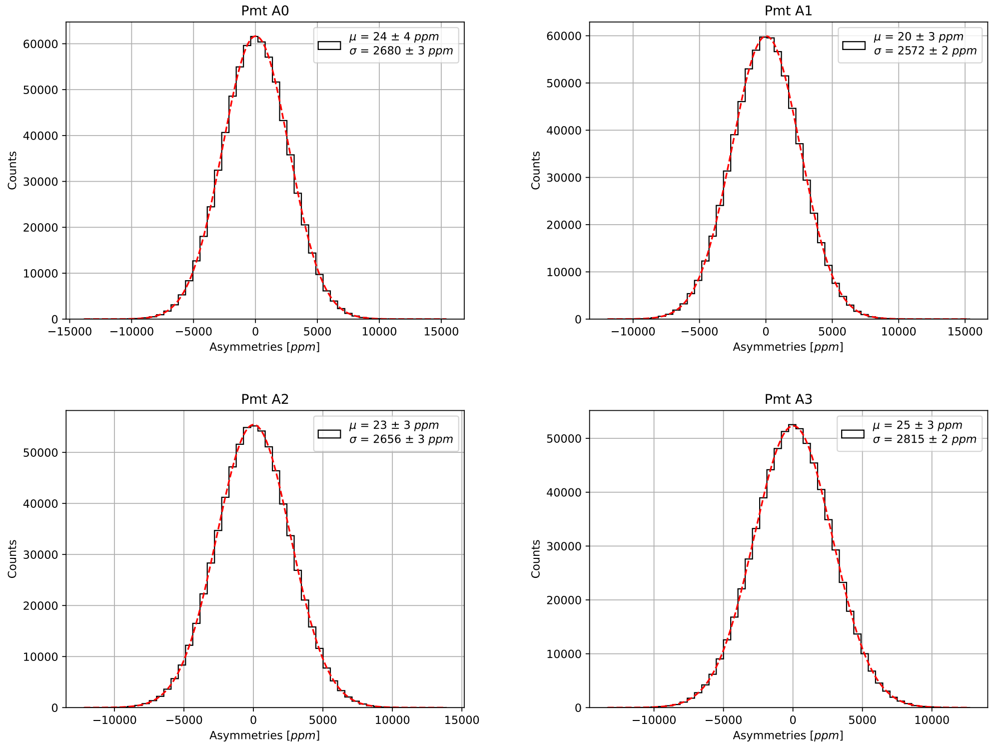

Figure 5.6: Histogram of the Asymmetry A0,A1,A2,A3.The Asymmetries are corrected removing the data without polarization. The raw asymmetries are multiplied by $\frac{1}{P}$

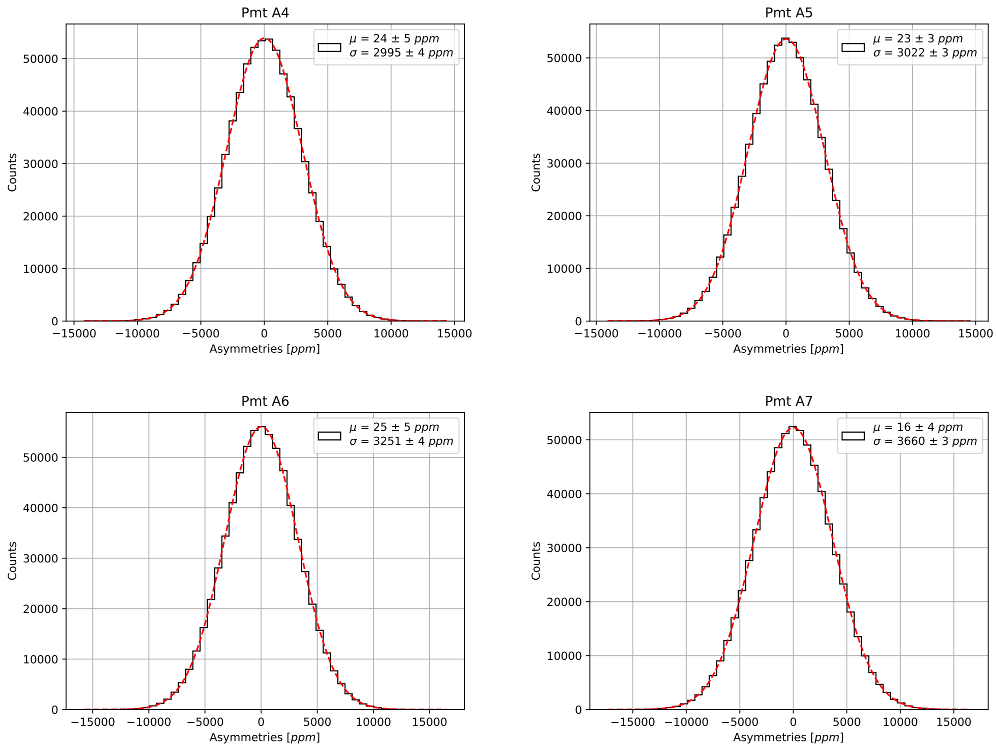

Figure 5.7: Histogram of the Asymmetry for Detector A.

$$y = \vec{x} \cdot \vec{\beta} + \epsilon \tag{5.9}$$

$\vec{x}$ are the independent variables, $\vec{\beta}$ are the parameters and ϵ is a noise parameter, that is supposed to be gaussian (however, the robustness of the OLS algorithm allows relaxing this request). Another

Pmt	reduced χ^2
B0	1.2 ± 0.2
B1	0.9 ± 0.2
B2	1.23 ± 0.2
A0	1.2 ± 0.2
A1	0.7 ± 0.2
A2	0.7 ± 0.2
A3	0.9 ± 0.2
A4	1.4 ± 0.2
A5	0.7 ± 0.2
A6	1.1 ± 0.2
A7	1.7 ± 0.2

Table 5.3: Reduced χ^2 for the gaussian fit of the asymmetry data.

important assumption is that the linear variables are not correlated. This last requirement is particularly important, as correlated data cannot be processed with either of the two algorithms used. Before proceeding with the fit, it is necessary to verify this assumption. The correlation matrix for the beam parameters is reported in a table 5.4.

	X	Y	θ_x	θ_y	E	I
X	1	-0.02	-0.99	0.06	0.04	-0.03
Y	-0.02	1	0.01	-0.65	0.01	-0.02
θ_x	-0.99	0.006	1	-0.005	-0.05	0.03
θ_y	0.06	-0.65	-0.05	1	-0.003	0.03
E	0.04	0.005	-0.05	-0.003	1	0.26
I	-0.03	-0.02	0.03	0.03	0.26	1

Table 5.4: Correlation coefficient between beam parameters.

The correlation between $(\theta_x, X); (\theta_y, Y)$ the values for the correlation are high compared to the other parameters.

The plots in figure 5.8 confirm the linear dependence between the parameters. For the θ_x versus the X position the data are distributed in line, and the data are completely anti-correlated. For the θ_y versus Y, the data are distributed following parallel lines, that have the same angular coefficient but different offsets. The lines are equally spaced, this means that the beam parameter δY is translated ,for a part of the events, by a multiple of some quantity δl_y. With the linear fit we estimate that $\delta l_y = 0.017 \pm 0.001\,\mu\mathrm{m}$. This effect could reproduce the data structure that we observe in plot *b* of figure 5.8.

It is clear that the have to modify the model to fit the data. We decided to include as linear independent variables only : I, X, Y, E. Before proceeding with the fit, it is interesting to study how A_n evolves increasing the data. What we intend is to plot the averaged values $\overline{A_n}$ as the number of events increases, where the average is made on all data collected from time $t = 0$ up to time $t = t_1$, s show in figure (5.9).

These plots are useful to check that the asymmetries converge to a certain value, and that there are no steep variations that could be related to the presence of remaining outliers. Besides this we observe that the sign of the asymmetries for the two detectors are opposite, in agreement with what we expect from the different kinematics, with the sign of the asymmetry given by the sign of the projection of the cross product $\vec{k} \times \vec{k}'$ along the axis orthogonal to the scattering plane. For detector A the cross product projection is positive, while for the detector B it is negative. For a better visualization of the data, especially to observe the dependence of the asymmetry on the beam parameters measured, it is useful to plot A versus each of the beam parameters. Unfortunately, the statistical error associated to the asymmetry is too high to appreciate whether there is a linear dependence in the data. For example, in figure 5.10 we plot the asymmetries A versus X.

The statistical error associated to A is too high to identify a trend in the values. A different

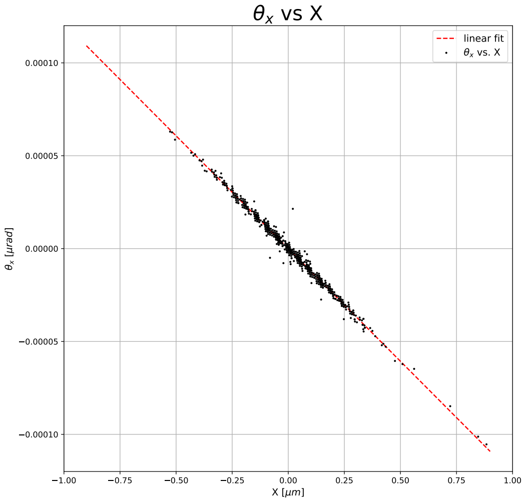

(a)

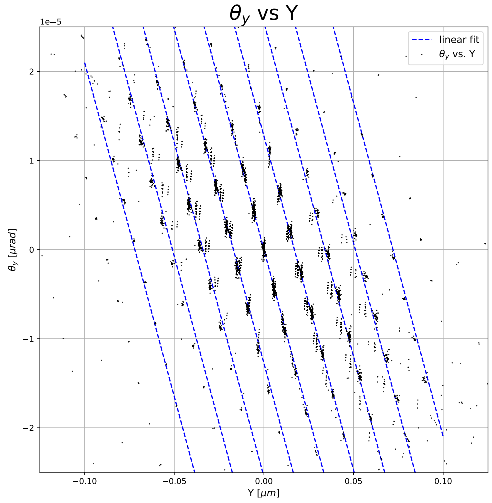

(b)

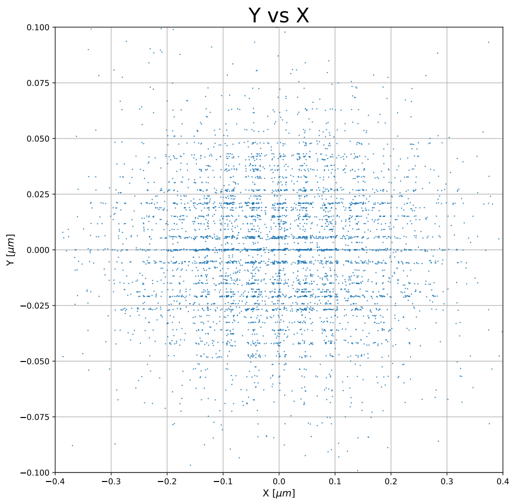

(c)

Figure 5.8: Correlation plots of positions and angles.

approach is to divide the x axis in small intervals, and average the asymmetries in each interval. In a plot of this type each point represents the overall asymmetry for a particular interval of X ,Y or E.

We report for brevity only the values for PMT A0 of detector A. In this case is simpler to identify the presence of a linear dependence in the data. The errors are computed with the formula defined in equation 2.14, considering each interval separately. Another approach that we can use to further reduce the fluctuations due to the high statistical error of A_n is to do an additional average for all the PMTs of each detector. This procedure decreases the error of a factor $\sqrt{8}$ for detector A and $\sqrt{3}$ for detector B. However, this does not take into account the different linear dependencies on the beam parameters for the various PMTs , and therefore is not immune from a possible bias.

We have explored different models to describe the asymmetry dependence on beam parameters. The first one is the linear model:

$$A = A_x\,\delta x + A_{phys} \tag{5.10}$$

For X and Y positions, we tried to use a 5th order polynomial:

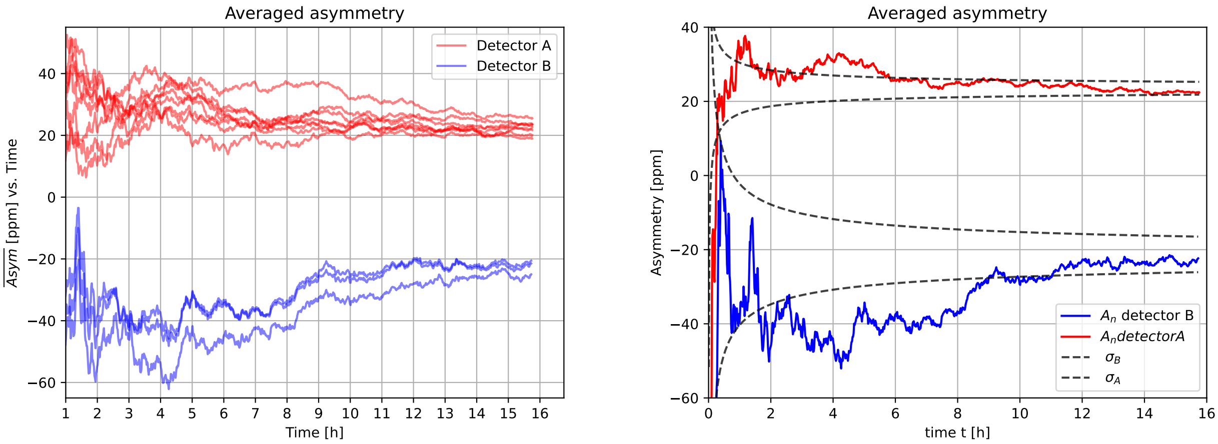

(a) *Averaged asymmetries for each PMT.*

(b) *Averaged asymmetry for detector A and B. The dotted line correspond to* 1σ *error.*

Figure 5.9: Plot of the Asymmetry versus time. The plot show the average over all the events collected from $t = 0$ to $t = t_1$. Each line represents A_n measured for PMT (in blue detector B and in red detector A). The values are corrected for the beam polarization, multiplying by $\frac{1}{p}$. No further correction is applied.

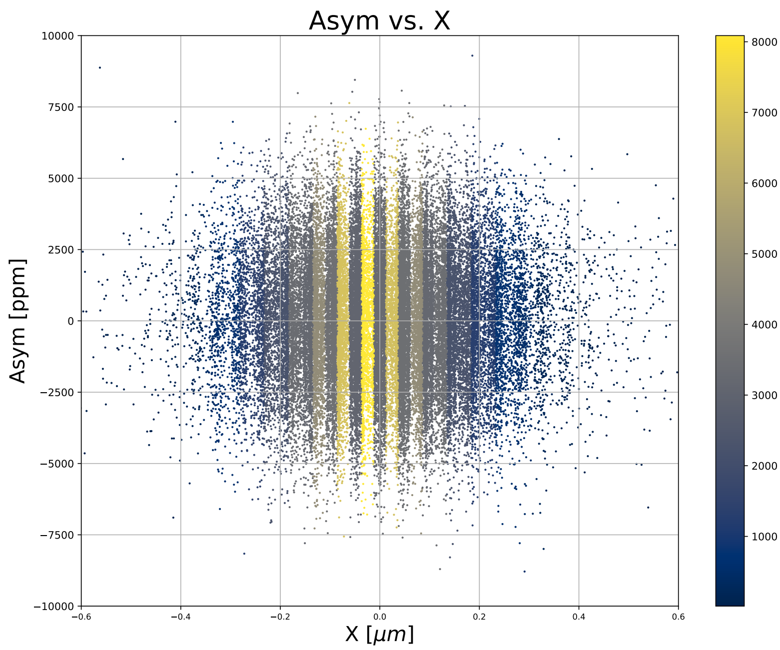

Figure 5.10: Detector A asymmetries versus X beam position. Because of the statistical uncertainties, it is not possible to visualize a linear dependence in the data. Each dot is colored depending on the density of points.

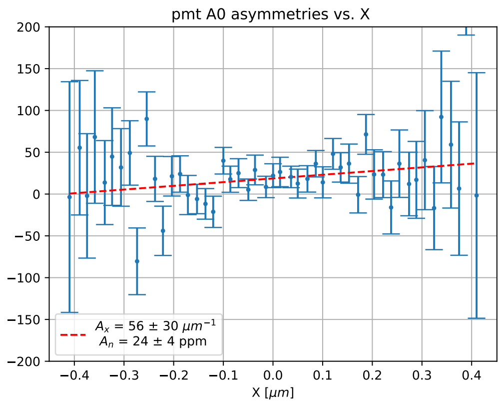

(a)

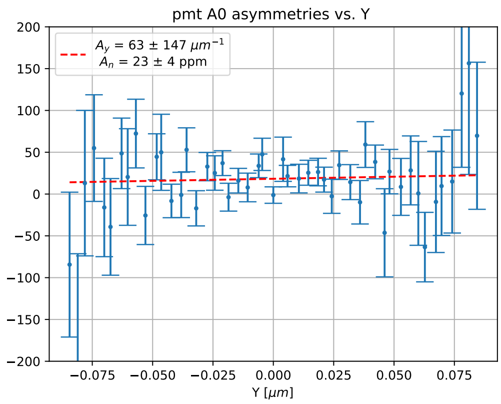

(b)

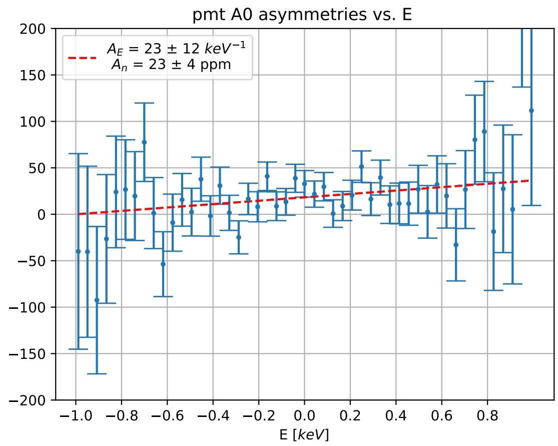

(c)

Figure 5.11: A versus δx, δy and δE. The plot are generated with 50 equally spaced bins. The red line is the best fit with a linear model.

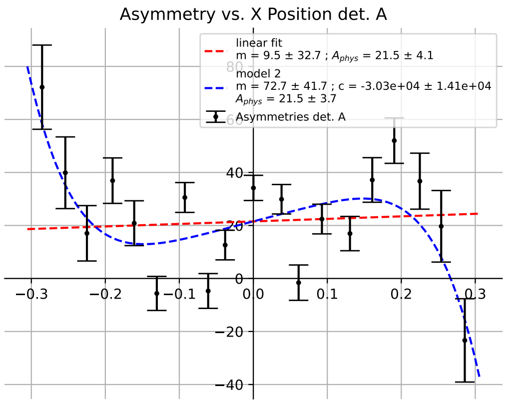

(a) *A versus δx, the linear model is the red line, the second used to fit the data is a polynomial, represented in blue.*

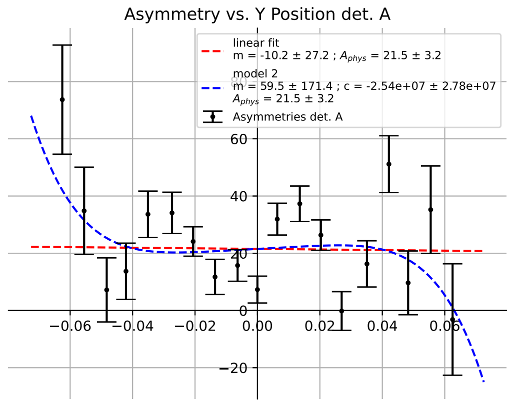

(b) *A versus δy, the linear model is the red line, the second used to fit the data is a polynomial, represented in blue.*

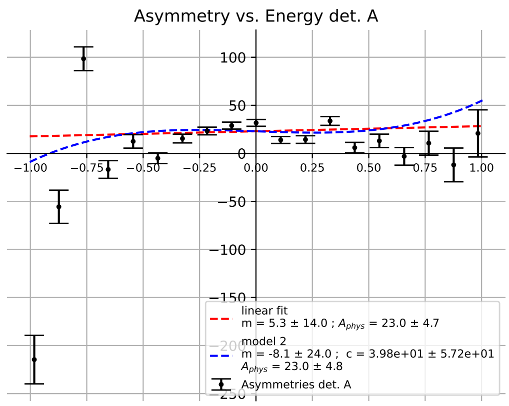

(c) *A versus δE, the linear model is the red line, the second used to fit the data is a polynomial, represented in blue.*

Figure 5.12: Averaged asymmetries versus the beam parameters δX, δY and δE. The x axis is divided in 19 intervals, and for each of them we average the asymmetries A.

$$A = c\,\delta x^5 + A_x\,\delta x + A_{phys} \tag{5.11}$$

While for the energy monitor, we tried a 3rd order polynomial:

$$A = c\,\delta E^3 + A_E\,\delta E + A_{phys} \tag{5.12}$$

The choice of an odd exponent is due to the observation that A increases near the edges of the plot with opposite sign.

The values of the fit parameters are reported in the plots of figures . The χ^2 of the fit are reported in table 5.5

detector A	X	Y	E
linear fit χ^2_{17}	99	59	94
alternative model χ^2_{16}	76	55	78

Table 5.5: χ^2_{ndf} for the different models used to fit the data show in figure 5.12

The χ^2 values are higher that the expected and we observe that the values for the model 2 are lower than the ones of linear fit. This high values can be explained with two considerations: the first one is that this procedure of averaging the data based on x interval leads to the loss of information that can influence the fit, the second consideration is that we are ignoring the possible error in the determination of δx. Despite this, we observe that using a model with more complicated dependencies does not change the values of A_{phys}. Because of this we do not see a strong evidence to change the linear model. The model that is used to extract the asymmetry is given in equation 5.13.

$$A_{tot} = A_{phy} \cdot P + \delta_I + A_x \delta x + A_y \delta y + A_E \delta E \tag{5.13}$$

the result of the fit are reported in 6.2, together with the final result of the asymmetry for detector A and B.

5.5 False Asymmetries

Until now the values for the false asymmetries were threated as the parameters of the fit. In this section we will investigate how we can obtain another different estimations, useful to check the validity of all the process of analysis of the data.

For $\frac{dA}{dX}$ and $\frac{dA}{dY}$, we conceptually exploit the possibility of varying the position of the beam on the target, as we did during one of the calibration phases. Using the same *wobbler 16* we asked MAMI to slowly change the beam position on the X and Y monitor. The change in position has the effect to modify the rates for the two detector, and from them it is possible to extract estimate the two false asymmetries related to the beam position. Now we will see how the two quantities are related. From the plot 5.13 we see that the counts are scaling linearly with the beam position, so we assume that the N are given by

$$N(x,...) = N_0 + m \cdot (x - x_0)$$

it is clear that the linear model can't be always good, at some point the electron will be deflected completely out of the detector, and so the counts will fall rapidly to zero. However, the magnets used to deflect the beam are producing small variation in the position, on the order of hundredths of a millimeters. Let's suppose that the beam position for two sub-events is x_1 and x_2, we can calculate the asymmetry between the two event, taking care of the possible effects due to the different position. We write explicitly:

$$Asym = \frac{N(x_1) - N(x_2)}{N(x_1) + N(x_2)} = \frac{N_0 + m \cdot (x_1 - x_0) - N_0 - m \cdot (x_2 - x_0)}{N(x_1) + N(x_2)} = \frac{m}{2N_0 + m \cdot (x_1 + x_2) - 2mx_0}(x_1 - x_2) \tag{5.14}$$

In this equation three different parameters appear: N_0 is the offset of the linear model, m is the angular coefficient, or the slope, and x_0 is the initial position respect to we compute the position variation. The first two terms are obtained by a linear fit, while x_0 is fixed conveniently.

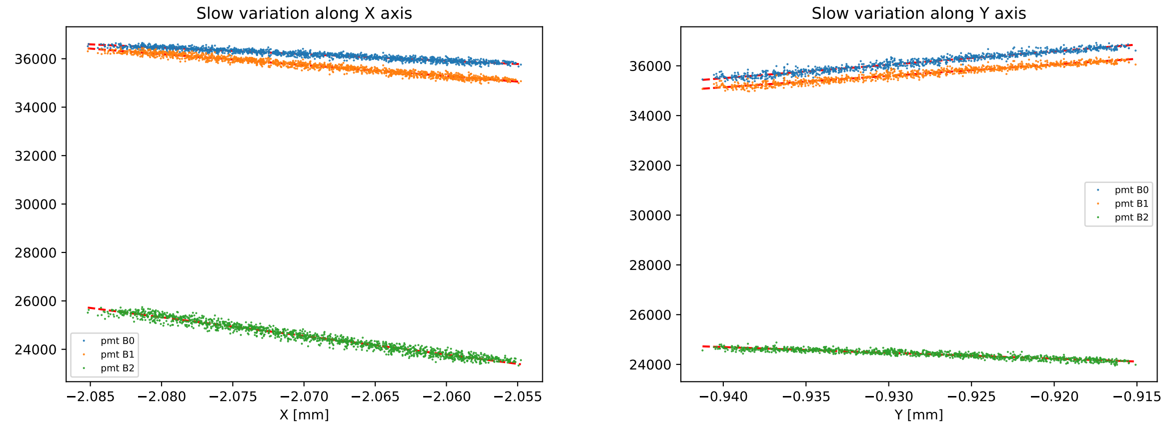

(a) *Plot for slow variation in x direction for detector B.* (b) *Plot for slow variation in x direction for detector B.*

Figure 5.13: Plot of the PMT counts versus the X position. The X position was slowly changed during the acquisition.

If the values x_1 and x_2 are are distributed symmetrically [1] We can simplify the denominator deleting the term $m \cdot (x_1 + x_2)$, fixing $x_0 = \frac{x(1)+x(2)}{2}$.

$$Asym = \frac{m}{2N_0}(x_1 - x_2) \tag{5.15}$$

The term in front of $(x_1 - x_2)$ can be compared to $\frac{dA}{dX}$. For N_0, the offset, we substitute the averaged value counts of each PMT for the polarized beam acquisitions. The data are reported in the table 5.6:

PMT	Detector A	Detector B
PMT 0	63733	17609
PMT 1	67262	17514
PMT 2	59782	14055
PMT 3	51736	
PMT 4	39057	
PMT 5	39667	
PMT 6	32768	
PMT 7	23593	

Table 5.6: Average counts per pmt, for time length of 20 ms.

The values for the false asymmetries obtained with this method are:

These values are not in agreement with A_x and A_y obtained from the fit (6.2). This may be due to the high correlation with the θ_x beam parameter. The negative correlation with θ_x means that when δX increases $\delta\theta_x$ decreases, and then the false asymmetries combined together, with the result that it is not possible to disentangle the two contributions.

5.5.1 Energy Asymmetry

For the energy asymmetry, a different method is necessary. We directly compute the Mott cross-section of the electron-carbon elastic scattering, and from that we can derive the false asymmetry due to energy variation. We start from the formula of the expected rates:

[1] In the same way of the beam parameter difference, shown in figure 5.2

'PMT'	A_x µm^{-1}	A_y µm^{-1}
B0	692	795
B1	395	682
B2	289	601
A0	233	533
A1	223	518
A2	202	493
A3	190	473
A4	211	503
A5	214	506
A6	217	510
A7	220	514

Table 5.7: Values for the false asymmetry, computed with the slow horizontal and vertical variation mode.

$$\frac{events}{time} = n_e N_t v_e \frac{\partial\sigma}{\partial\Omega}(\partial\Omega_a)\epsilon \tag{5.16}$$

Where:

- n_e electron density of the beam.
- N_t Number of scattering centers of the carbon target.
- v_e electron speed.
- $\partial\Omega_a$ solid angle acceptance of the spectrometers.
- ϵ detector efficiency.

We do not need to compute directly the expected rate for the two detectors, because some terms cancel out when substituted in the formula for the asymmetry, the only relevant term is the cross section:

$$A = A_n + \frac{\sigma(E_1) - \sigma(E_2)}{\sigma(E_1) + \sigma(E_2)}$$

Because $\partial\Omega_a$ is a common term in the numerator and in the denominator, we can simplify the expression and substitute σ with $\frac{\partial\sigma}{\partial\Omega}$. The Mott cross section is given by the formula below:

$$\frac{\partial\sigma}{\partial\Omega} = \frac{Z^2\alpha(\hbar c)^2}{E^2 sin^4(\frac{\theta}{2})} \cdot \frac{E'}{E} \cdot cos(\frac{\theta}{2}) \cdot F^2(\vec{q}) \tag{5.17}$$

Where the first term is the Rutherford cross-section, the second term represent the recoil of the nucleus, the third terms is the $cos(\frac{\theta}{2})$, and the last term is the nucleus form factor. The Recoil term can be written:

$$\frac{E'}{E} = \frac{1}{1 + \frac{E}{Mc^2}(1 - cos(\theta))}$$

With this final substitution we can rewrite the Mott cross section as:

$$\frac{\partial\sigma}{\partial\Omega} = \frac{D}{AE^2} \cdot \frac{1}{1 + EC} \cdot B \cdot F^2(\vec{q})$$

Where $D = Z^2\alpha((\hbar c)^2)$, $A = sin^4(\frac{\theta}{2})$ and $B = cos(\frac{\theta}{2})$. To compute the false asymmetry related to energy, we always assume that for small energy variation, a first order approximation is valid:

$$\sigma(E_1) \simeq \sigma(E_0) + \frac{\partial\sigma}{\partial E}(E_1 - E_0)$$

The approximations is done for small variations around the beam energy, which is 570 MeV. Now it is possible to compute the false asymmetry, the searched expression is:

$$A_E = \frac{\partial\sigma}{\partial E \partial\Omega} \cdot (2\frac{\partial\sigma}{\partial\Omega})^{-1} \tag{5.18}$$

We compute the above formula withe the constant A,B,C,D defined in 5.17.

$$A_E = -\frac{1}{2}\frac{2 + CE_0}{E_0 + E_0^2 C} \tag{5.19}$$

The result, applying the above formula is $A_e = -1.75\,\frac{ppm}{\mathrm{keV}}$. We can compare this result with the values obtained from the fit. The results are in agreement with the sign, if fact we expect a negative effect related to the beam variation. However, the false asymmetries from the fit are 1 order higher than the values computed here. A possible reason could be that we are underestimating other contributions that seems to be important with the energy variation. The estimation of the contribution of the false asymmetries to A is not accurate. This may be due to the correlation between the beam parameters, that combines together the different effects, or secondary effects that are not included in the calculation of the coefficients. Estimate the parameters through the linear fit seems to be easier. An alternative method may be to exploit Monte Carlo simulations of the entire experimental apparatus, which are however expensive, compared to linear regression.

5.6 Rates on Lead

After all the calibrations are done, we proceeded with the measurement of the rates on lead target, one of the objectives of the experiment. The lead target installed is a made of a thin layer with a thickness of 0.5 mm, and it is not isotopically pure. We took 14 acquisitions lasting $\simeq 2,5$ minutes, which corresponds to 6950 events. For each of these acquisitions we set the beam current at different values, ranging from 10 µA to 22 µA of intensity. The rates are then reported as a function of the current and linear model is used to fit the data.

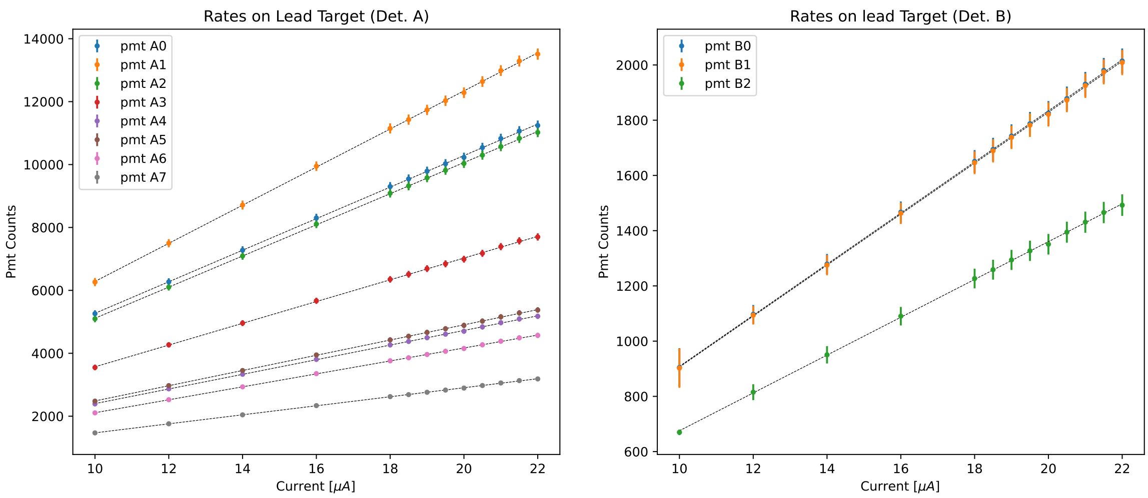

Figure 5.14: rates on lead Target as function of the beam current. The rates for each PMT of detector A (on the left), and detector B (on the right) are reported.

We fit using a linear model the data. The angular coefficient m and the offset q are reported in the table 5.8 for each PMTs of the two detectors.

PMT	m [µA^{-1}]	q	χ^2 (dof = 9)
A0	501.4 +/- 2.2	257 +/- 40	13.8
A1	605.8 +/- 2.3	226 +/- 42	13.4
A2	495.0 +/- 1.5	163 +/- 27	7.0
A3	345.7 +/- 1.6	113 +/- 30	12.0
A4	232.6 +/- 0.9	74 +/- 16	5.4
A5	242.0 +/- 0.7	66 +/- 14	3.5
A6	205.8 +/- 0.7	52 +/- 12	3.1
A7	143.4 +/- 0.5	36 +/- 9	2.3
B0	92.6 +/- 0.3	-17 +/- 6	2.1
B1	92.3 +/- 0.3	-17 +/- 6	1.9
B2	68.5 +/- 0.3	-9 +/- 6	2.8

Table 5.8: Lead rates, the values are measured for a target width of 0.5 mm.

The PMT Counts with this target, increase from 100 counts for detector B to 500 counts every 1 µA. It is interesting to recover the formula of the experimental standard deviation σ associated to the asymmetry distribution:

$$\sigma = \sqrt{\frac{1}{2N \cdot n}} \tag{5.20}$$

Where N is the counts per sub-event, while n is the number of event analyzed. Let's suppose that we want to obtain, for each PMTs, a statistical error not greater than $4,8\,ppm$. With this accuracy, the overall result A will have an error given by $\frac{4.8\,ppm}{\sqrt{8}} \simeq 1.7\,ppm$, equal to the statistical error that we have obtained for the measurement of A_n with ^{12}C (see table 6.4) while for detector B an overall result of $2.8\,ppm$. We have computed the time needed to achieve this accuracy for both the two detectors, given in total hours of experiment. This values are not casual: as we will see in the next part of this chapter, we managed to obtain this accuracy for the same measurement on carbon

current I	T [h] Det A	T [h] Det B
10	344	1487
12.5	277	1185
15	232	985
17.5	199	843
20	175	737

Table 5.9: Estimated time needed for the upcoming experiments to measure the transverse asymmetry for Lead with an aimed precision of $1.7\,ppm$ for detector A and $2.8\,ppm$ for detector B.

The amount of time needed to obtain this accuracy with carbon is roughly $15h$ with 10 µA. The same measurement with lead will need 23 times the time accumulated for Carbon. This is due to the fact that the target thickness for lead target must be smaller than the target thickness for carbon. Because the atomic number of lead is greater than carbon, the amount of radiation during the experiment is exponentially higher. During the experiment, the A1 experimental hall is constantly monitored, the radiation level can not exceed a certain threshold. This imposes an important constrain to the maximum target thickness. As a consequence, despite the Mott cross section increases as Z^2 and favor heavy nuclei, the radiation levels dictates to work with lower beam currents and smaller thicknesses for the target. Another experimental problem is the low melting point of Pb. To prevent the target from melting, the beam current intensity must be controlled in order to reduce the amount of heat produced by the beam. For the lead target a cooling system with a mixture of alcohol and water at $0°C$ degree is installed. In addiction, the beam position is continuously varied, following a Lissajous curve, in order to spread the beam hitting points. This is done using fast bending magnets, with a frequency much higher than the frequency of the polarization sequence, in order to avoid possible false asymmetry induced by the change in the positions. The combinations of all these factors makes the measurement with lead more challenging. However the A_n is valuable, in order to cancel possible systematics effect for the parity violating scattering, besides the fact that measurements made by PREX collaboration [13] do not agree with the theoretical prediction, suggesting the need to repeat the measurement independently.

Chapter 6

Final Result and Conclusion

In this chapter we show the result obtained for the transverse asymmetry measured on carbon during the experiment. The first result that we report is the values of asymmetry $\overline{A}_n$ computed as the average over all the events, after applying the various cut discussed before to remove wrong data and outliers. The values reported in tables 6.1a 6.1b are corrected by te beam polarization ($A_{raw} \times \frac{1}{P}$) and by the current asymmetry:

$$\overline{A}_n = \frac{\overline{A}_{raw}}{P} - \overline{A}_I \tag{6.1}$$

The sign of the asymmetry is given by the sign of the cross product between $\vec{k}$ incident electron and $\vec{k'}$ scattered electron. The results have positive sign for detector A and negative sign for detector B, in agreement with the kinematics. In section 4.3.6 we have discussed possible effects that arise from the presence of a PMT offset when we check the linearity of the PMTs respect to the beam current variation. This systematic effect tends to decrease the reconstructed values of the asymmetry by a factor c, computed in equation 4.12. The predicted value of c reported in table 4.12; we also compute the ratio between the final asymmetries with and without subtracting the offset, that is reported in table 6.1c. The values of c computed in these two ways are coherent.

The results reported in table 6.1b are show in plot 6.1. To Obtain a final asymmetry for detector A and B, the asymmetries for each plot are averaged using the formula:

$$A_n = \sum_{i=0}^{n_{PMT}} \frac{w_i A_i}{\sum_{i=0}^{n_{PMT}} w_i} \tag{6.2}$$

With $w_i = \frac{1}{\sigma_i^2}$. The above equation is the error-weighted mean, used to combine measurements with different statistical error.

The result obtained for both the two detector are reported here. The two values are in agreement with the expected sign and compatible with the previous measurement performed at MAMI [16].

- Asymmetry for detector A, $A_A = 23.6 \pm 1.7$ ppm.
- Asymmetry for detector B, $A_B = -21 \pm 5$ ppm.

PMT	$\overline{A}_n$ $[ppm]$	σ
B0	-19.92	7.7
B1	-19.0	7.8
B2	-23.42	8.7
A0	18.8	3.7
A1	16.05	3.4
A2	18.45	3.7
A3	19.0	4.2
A4	20.84	5.0
A5	22.83	4.9
A6	17.49	5.5
A7	19.24	6.6

(a) *Asimmetries, with offset not subtracted.*

PMT	$\overline{A}_n$ $[ppm]$	σ
B0	-20.61	8
B1	-19.69	8
B2	-24.13	9
A0	24.55	4.2
A1	22.54	4.1
A2	24.37	4.3
A3	23.49	4.7
A4	24.21	5.4
A5	26.39	5.3
A6	19.82	5.9
A7	20.97	6.9

(b) *Asymmetries with offsets subtracted*

PMT index	$\overline{A}_{notcorrected}/\overline{A}_{corrected}$
B0	0.97
B1	0.96
B2	0.97
A0	0.77
A1	0.71
A2	0.76
A3	0.81
A4	0.86
A5	0.87
A6	0.88
A7	0.92

(c) *c factor, as defined in 4.12*

Table 6.1: Averaged asymmetries over all the events. The values are corrected subtracting $\overline{A}_I$ and considering the effective polarization p of the beam

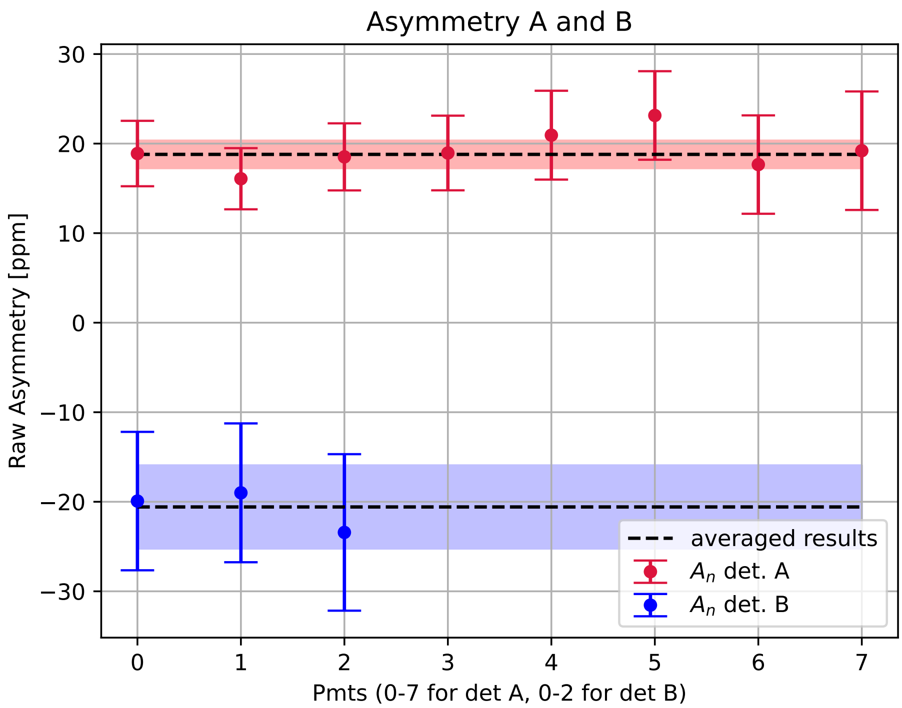

Figure 6.1: Plot of $\overline{A}_n$. The result are corrected by the beam asymmetry current and polarization. The black line represent the overall value A_n computed with the formula 6.2. $\overline{\delta I}$.

6.1 Linear Model Result

The result obtained from the linear fit of the asymmetries versus the beam parameters are reported here, together with the false asymmetry values. The final parameters for the model are X, Y, E, and the current asymmetry I is subtracted for each event:

$$A_{tot} - A_I = A_n \frac{1}{P} + A_x \delta X + A_y \delta Y + A_e \delta E \tag{6.3}$$

The result for detector A:

PMT	A_n	A_x	A_y	A_e	$\chi^2_{reduced}$
A0	24 ± 4	67 ± 27	-8 ± 135	-22 ± 12	1.000 ± 0.002
A1	23 ± 4	9 ± 26	-85 ± 130	-10 ± 11	1.001 ± 0.002
A2	23 ± 4	-12 ± 27	-24 ± 134	-21 ± 12	1.000 ± 0.002
A3	23 ± 5	14 ± 29	-180 ± 142	-31 ± 12	0.999 ± 0.002
A4	25 ± 5	50 ± 31	-85 ± 151	-26 ± 13	1.000 ± 0.002
A5	27 ± 5	31 ± 31	198 ± 152	-37 ± 13	1.001 ± 0.002
A6	20 ± 5	7 ± 33	142 ± 164	-31 ± 14	1.000 ± 0.002
A7	20 ± 6	6 ± 38	78 ± 184	-14 ± 16	1.001 ± 0.002

Table 6.2: Fit result with the linear model, for detector A.

the result for detector B:

The final results of the transverse asymmetry for the two detectors, for a $Q^2 = 0.04\,\text{GeV}^2$, computed with the weighted mean are then:

the values obtained from the linear fit, and the values obtained with a simple data averaging do not differ much from each other. This implies that the contribution due to the false asymmetries is generally small. This indicates that the beam stabilization decreased the correlated differences due to the different polarization of the beam, and confirm the goodness of the measurement of the transverse asymmetry at MAMI accelerator.

PMT	A_n	Bx	By	Be	$\chi^2_{reduced}$
B0	-20 ± 8	-59 ± 40	-25 ± 187	-14 ± 17	1.000 ± 0.002
B1	-20 ± 8	-64 ± 40	47 ± 188	-22 ± 18	1.000 ± 0.002
B2	-24 ± 9	-65 ± 46	-170 ± 211	-61 ± 20	1.000 ± 0.002

Table 6.3: Fit result with the linear model, for detector B.

DETECTOR	An
A	23.1 ± 1.7
B	-21 ± 5

Table 6.4: Overall result for detector A and B.

6.2 Data Without Polarization

In this section we report the result obtained for the block of runs that showed an unexpected behaviour, compatible with the absence of a transverse polarization of the beam. This data are analyzed in the same way as good data, and the result are reported in the table 6.5

PMT	An	Ax	Ay	Ae	$\chi_{reduced}$
A0	-12 +/- 5	88 +/- 30	38 +/- 154	-25 +/- 13	1.0 +/- 0.002
A1	-9 +/- 5	44 +/- 29	57 +/- 149	-23 +/- 13	1.0 +/- 0.002
A2	-5 +/- 5	17 +/- 30	111 +/- 154	-38 +/- 13	1.0 +/- 0.002
A3	-7 +/- 6	47 +/- 32	85 +/- 163	-51 +/- 14	1.0 +/- 0.002
A4	-5 +/- 6	38 +/- 33	192 +/- 171	-46 +/- 15	1.0 +/- 0.002
A5	-4 +/- 6	67 +/- 34	177 +/- 173	-52 +/- 15	1.0 +/- 0.002
A6	-1 +/- 7	70 +/- 36	-101 +/- 186	-54 +/- 16	1.0 +/- 0.002
A7	-1 +/- 7	25 +/- 41	-494 +/- 209	-41 +/- 18	1.0 +/- 0.002
B0	-13 +/- 11	48 +/- 58	-48 +/- 294	14 +/- 26	1.0 +/- 0.002
B1	-11 +/- 11	51 +/- 58	44 +/- 295	-3 +/- 26	1.0 +/- 0.002
B2	-7 +/- 12	90 +/- 65	-166 +/- 333	-9 +/- 30	1.0 +/- 0.002

Table 6.5: Analysis result for the data with polarization loss

The overall values are -5 ± 2 for detector A and -8 ± 5 for detector B. The two values are compatible with each other

6.3 Conclusion and Outlook

The transverse asymmetry for ^{12}C target, at a $Q^2 = 0.04\,\mathrm{GeV}^2$ has been measured with the new counting-based data acquisition systems. The measurement are reported in table 6.4, and are in agreement with the theoretical sign due to the different scattering kinematic for detector A and B. These measurement are in agreement with the measurement reported in [16], $23.9 \pm 1(stat) \pm 0.7(syst)\,ppm$ for detector A and $-21.9 \pm 1.5(stat) \pm 1.6(syst)\,ppm$. These results are encouraging: with the new electronic setup we have obtained similar values for the transverse asymmetry with respect to the old measurement, that were based on the integration of the PMT current, instead of the detection of the single electron pulses. With this new electronic, it will be possible to measure, for the first time, at MAMI, the transverse asymmetry for lead target, important in prevision of the future parity-violating experiment that will take place at MESA accelerator.

Appendices

.1 Abbreviations

Here we report a list of common abbreviation:

- **EOS**: equation of state.
- **PV**; parity violating experiment.
- **BNSSA**: beam normal single spin asymmetry.
- **ENMO**: energy monitor.
- **PIMO**: current monitor.
- **VFC**: voltage to frequency converter.
- **PMT**: photomultiplier tube.
- **RTM**: race track microtron.
- **XYMO**: position monitor.

.2 Beam Monitors Formula

.3 Data Tree

In this section we discuss briefly the functions implemented to fill the data tree, from the monitor raw values. In the majority of the transverse asymmetry experiments, the position of the beam respect to the transverse plane is measured in three different position (see next figure). The three monitors are named XY21, XY25, XY26. During this experiment, only two monitors are available, XY25 and XY21, and are used in the analysis.

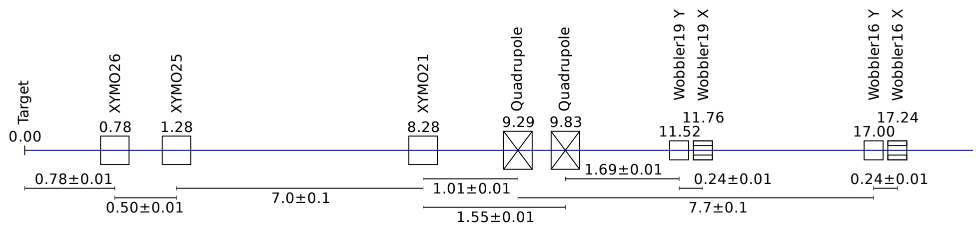

Figure 2: Scheme of the beam line, the target is on the left side of the picture.

Other monitors that are used are I21, I13 and E18, the current monitors and energy monitor, respectively. In the figure above, the current monitor I21 correspond to XY21. The E18 monitor, named also ENMO, and I13 are not shown in this picture, because they are placed in the racetrack RTM3 (see figure 3.3). The raw values from these monitors and the detectors are collected and stored in binary files produced by the A1 computer. The monitors data and are made by integers numbers, the digital output of the voltage to frequency converter. The beam parameters measured by the beam monitors are saved in the class *Beam*, in figure 4.19. The output of the VFCs is proportional to the signal of the beam monitors, as shown in figure 3.14. The analysis program converts from raw counts to values in V using the formula is given in equation 3.14. Once the voltage values are computed, the analysis program does another conversion, from voltage to the physical units. The formula for this conversion is given in 4:

$$\frac{V \cdot scale - offset}{I} \tag{4}$$

In th formula the coefficient *scale* and *offset* are loaded from the standard configuration files, where all the scaling factors measured during the calibrations are stored. In the above formula we divide by the beam current I, because the output signal of positions and energy the monitors are proportional to the intensity of the beam, and need to be normalized. For the current monitor, the signal is directly proportional to the current, so the denominator is omitted. The important quantities that are computed by the analysis program are: X, Y, position of the beam on the target, θ_x and θ_y scattering angles, current I and energy E. These quantities are saved in a different class, the *Target* class. We now briefly present the function implemented to process the raw data and retrieve these quantities. The position X and Y are computed as explained in section 4.3.2. In brevity, assuming that the beam is moving in a straight line, the beam trajectory is described by:

$$y = m_y \cdot z + q_y$$
$$x = m_x \cdot z + q_x$$

The values that we are looking for are q_x and q_y, x and y intercept. Imposing in the above equations the passage through the points (Z_{25};X_{25}) and (Z_{21};X_{21}), the intercepts of the equation are given by:

$$q_x = \frac{Z_{25} \cdot X_{21} - Z_{21} \cdot X_{25}}{Z_{25} - Z_{21}} \tag{5}$$

The scattering angles θ_x and θ_y are instead related to the slope m, knowing that $tan(\theta) = m$. The angles are given by the formula:

$$\theta_x = \frac{X_{25} - X_{21}}{Z_{25} - Z_{21}} \tag{6}$$

With these values, the analysis program compute the differences between different polarization states, that are the independent variables for the linear fit. The data tree contains other two classes: detector A and detector B. Each detector class is structured in a number of sub-classes equal to the number of the PMTs, where the counts are stored and processed. The raw data are saved in the variable *rawCounts*, that contains 4 integer number, one for each sub-events. Then the analysis program load the parameters saved in the standard configuration files, where the PMTs offset measured during the auto-calibration are stored. The *offsetCorrectedCounts* are given by equation 7

$$offsetCorrectedCounts = \frac{rawCounts}{N_0^i} \tag{7}$$

where N_0^i is the offset measured for PMT i. Other two variables, *positivePolarityCounts* and *negativePolarityCounts* are given by the sum of the offsetcorrectedCounts for sub-events with the same polarization. The *asymmetry* is given by the formula 8

$$asymmetry = \frac{(Pc[1] + Pc[2]) - (Nc[1] + Nc[2])}{(Pc[1] + Pc[2]) + (Nc[1] + Nc[2])} \tag{8}$$

where Pc and Nc stands for positive and negative polarity counts.

List of Tables

Bibliography

[1] M Thiel, C Sfienti, J Piekarewicz, C J Horowitz, and M Vanderhaeghen. Neutron skins of atomic nuclei: per aspera ad astra. *Journal of Physics G: Nuclear and Particle Physics*, 46(9):093003, aug 2019.

[2] H. A. Bethe and R. F. Bacher. Nuclear Physics A. Stationary States of Nuclei. *Rev. Mod. Phys.*, 8:82–229, 1936.

[3] J. Piekarewicz and M. Centelles. Incompressibility of neutron-rich matter. *Physical Review C*, 79(5), may 2009.

[4] S. Abrahamyan et al. Measurement of the Neutron Radius of 208Pb Through Parity-Violation in Electron Scattering. *Phys. Rev. Lett.*, 108:112502, 2012.

[5] F. J. Fattoyev and J. Piekarewicz. Accurate calibration of relativistic mean-field models: Correlating observables and providing meaningful theoretical uncertainties. *Physical Review C*, 84(6), dec 2011.

[6] D. Adhikari et al. Accurate Determination of the Neutron Skin Thickness of ^{208}Pb through Parity-Violation in Electron Scattering. *Phys. Rev. Lett.*, 126(17):172502, 2021.

[7] Lee Lindblom. Determining the nuclear equation of state from neutron-star masses and radii. *The Astrophysical Journal*, 398:569–573, 1992.

[8] J Lattimer and M Prakash. Neutron star observations: Prognosis for equation of state constraints. *Physics Reports*, 442(1-6):109–165, apr 2007.

[9] B. G. Todd-Rutel and J. Piekarewicz. Neutron-Rich Nuclei and Neutron Stars: A New Accurately Calibrated Interaction for the Study of Neutron-Rich Matter. *Phys. Rev. Lett.*, 95:122501, Sep 2005.

[10] B. P. Abbott et al. GW170817: Observation of Gravitational Waves from a Binary Neutron Star Inspiral. *Phys. Rev. Lett.*, 119(16):161101, 2017.

[11] Taylor Binnington and Eric Poisson. Relativistic theory of tidal Love numbers. *Phys. Rev. D*, 80:084018, 2009.

[12] M. Gorchtein and C. J. Horowitz. Analyzing power in elastic scattering of electrons off a spin-0 target. *Physical Review C*, 77(4), apr 2008.

[13] S. Abrahamyan et al. New Measurements of the Transverse Beam Asymmetry for Elastic Electron Scattering from Selected Nuclei. *Phys. Rev. Lett.*, 109:192501, 2012.

[14] Mikhail Gorchtein. Doubly virtual Compton scattering and the beam normal spin asymmetry. *Physical Review C*, 73(3), mar 2006.

[15] Oleksandr Koshchii, Mikhail Gorchtein, Xavier Roca-Maza, and Hubert Spiesberger. Beam-normal single-spin asymmetry in elastic scattering of electrons from a spin-0 nucleus. *Physical Review C*, 103(6), jun 2021.

[16] A. Esser et al. First Measurement of the Q^2 Dependence of the Beam-Normal Single Spin Asymmetry for Elastic Scattering off Carbon. *Phys. Rev. Lett.*, 121(2):022503, 2018.

[17] B. S. Schlimme et al. Vertical Beam Polarization at MAMI. *Nucl. Instrum. Meth. A*, 850:54–60, 2017.

[18] Robert Goldstein. Pockels Cell Primer. *Laser Focus*, 34:21, 1968.

[19] Timothy Gay and F. Dunning. Mott electron polarimetry. *Review of Scientific Instruments*, 63:1635 – 1651, 03 1992.

[20] M. Dehn. Strahldiagnostik und Analyse der optischen Eigenschaften des Strahlführungssystems von MAMI. *Diplomarbeit*, 2004.

[21] Single and Multichannel, Synchronous Voltage-to-Frequency Converters, AD7741. *Analog Devices.*

[22] F. Anghinolfi, P. Jarron, F. Krummenacher, E. Usenko, and M.C.S. Williams. NINO, an ultra-fast, low-power, front-end amplifier discriminator for the Time-Of-Flight detector in ALICE experiment. In *2003 IEEE Nuclear Science Symposium. Conference Record (IEEE Cat. No.03CH37515)*, volume 1, pages 375–379 Vol.1, 2003.